ISSN 1590-8844
Vol. 07 No 01
2006

International Journal of Mechanics and Control

Honorary Editor: Guido Belforte

Editor: Andrea Manuello Bertetto

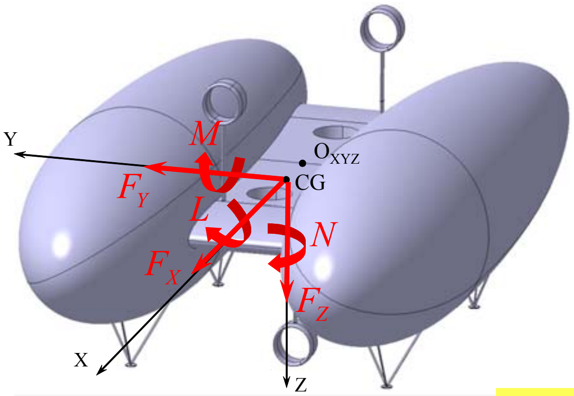

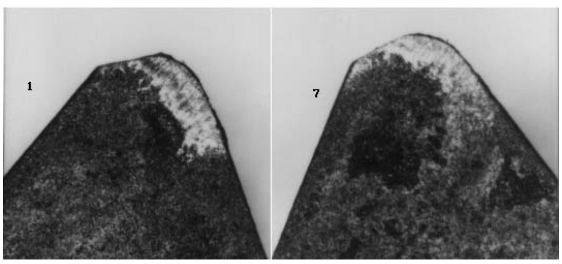

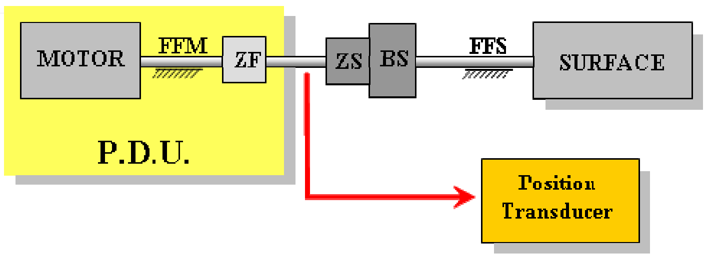

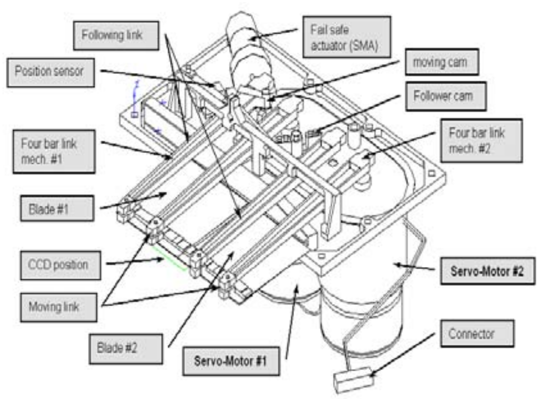

LIBRERIA EDITRICE UNIVERSITARIA
LEVROTTO & BELLA
TORINO

Official Torino Italy Court Registration
n.5390, 5th May 2000

Deposito presso il Tribunale di Torino
numero 5390 del 5 maggio 2000
Direttore responsabile:
Andrea Manuello Bertetto

International Journal of Mechanics and Control

The Journal is addressed to scientists and engineers who work in the fields of mechanics (mechanics, machines, systems, control, structures). It is edited in Turin (Northern Italy) by Levrotto&Bella Co., with an international board of editors. It will have not advertising.
Turin has a great and long tradition in mechanics and automation of mechanical systems. The journal would will to satisfy the needs of young research workers of having their work published on a qualified paper in a short time, and of the public need to read the results of researches as fast as possible.
Interested parties will be University Departments, Private or Public Research Centres, Innovative Industries.

Aims and scope

The *International Journal of Mechanics and Control* publishes as rapidly as possible manuscripts of high standards. It aims at providing a fast means of exchange of ideas among workers in Mechanics, at offering an effective method of bringing new results quickly to the public and at establishing an informal vehicle for the discussion of ideas that may still in the formative stages.

Language: English

International Journal of Mechanics and Control will publish both scientific and applied contributions. The scope of the journal includes theoretical and computational methods, their applications and experimental procedures used to validate the theoretical foundations. The research reported in the journal will address the issues of new formulations, solution, algorithms, computational efficiency, analytical and computational kinematics synthesis, system dynamics, structures, flexibility effects, control, optimisation, real-time simulation, reliability and durability. Fields such as vehicle dynamics, aerospace technology, robotics and mechatronics, machine dynamics, crashworthiness, biomechanics, computer graphics, or system identification are also covered by the journal.

Please address contributions to

Prof. Guido Belforte
Prof. Andrea Manuello Bertetto
PhD Eng. Elvio Bonisoli

Dept. of Mechanics
Technical University - Politecnico di Torino
C.so Duca degli Abruzzi, 24.
10129 - Torino - Italy - E.C.

e_mail: jomac@polito.it

Subscription information

Subscription order must be sent to
the publisher:

Libreria Editrice Universitaria
Levrotto&Bella
2/E via Pigafetta – 10129 Torino – Italy

www.levrotto-bella.net
e_mail: info@levrotto-bella.net
tel. +39.011.5097367
+39.011.5083690
fax +39.011.504025

ISSN 1590-8844
International Journal of Mechanics and Control, Vol. 07, No. 01, 2006

MATHEMATICAL MODEL FOR SIMULATION ANALISYS OF A REMOTELY-PILOTED LIGHTER-THAN-AIR PLATFORM

Battipede Manuela Gili Piero Lando Marco

Aeronautical and Space Department, Politecnico di Torino

ABSTRACT

This paper is focused on the dynamic modelling of an unconventional remotely-piloted Lighter-Than-Air vehicle, whose mathematical model is based on a 6 degree-of-freedom, 12 states nonlinear system, described by the basic equations of the Newtonian mechanics. Emphasis is placed on those innovative and peculiar aspects of the dynamic modelling, which allow the development of a complete low-cost-high-fidelity Flight Simulator used both for technical and commercial purposes. In particular, the availability of this tool, featuring real time simulations, is essential for the design, test and implementation of the most suitable flight control system, as well as for the pilot training of this innovative airship.

Keywords: airship, dynamic modelling, flight simulation, flight mechanics

1 INTRODUCTION

Over the last decade, the interest of various market sectors, involving military, civil and private organizations has more and more focused on unmanned aerial vehicles able to perform extremely different tasks, such as monitoring, telecommunications, advertising and surveillance. In addition, concern in environmental impact has grown, particularly in those areas where these air-vehicles should operate. Among the several topologies of unmanned aerial vehicles, remotely-piloted airships certainly represent the most interesting solution for low speed, low altitude exploration and monitoring missions and, at the same time, they can be easily arranged to have high performance and respect the environmental compatibility. In fact, their aerostatic lift makes them noiseless, non-obtrusive, ecological and useful for environmental applications [1], such as oceanographic [2], [3] and biological studies [4], traffic monitoring, ecological and climate research, inspection of endangered ecological sites as well as long-term variability studies. Moreover, airships have already been employed as camera and TV platforms for specialized scientific tasks and feature remarkable advantages over the other transport means in civil applications [5].

Contact author: Dr. Battipede Manuela

Aeronautical and Space Department, Politecnico di Torino
C.so Duca degli Abruzzi 24, 10129, Torino, Italy.
E-mail: manuela.battipede@polito.it

In particular, they can operate in places with inadequate airport facilities, which could be reached only by air-vehicles provided with hovering capabilities, such as the rotary-wing aircraft. Airships, however, benefit from the absence of rotor, which generally implies high structural design costs and strong payload (cameras and monitoring equipments) vibrations. Nevertheless, conventional airships show some drawbacks, such as the poor capability of operating in adverse environmental conditions. Their primary aerodynamic command system, in fact, together with the low weight and the big size of their whole body, makes them scarcely manoeuvrable in wind conditions or when a gust suddenly occurs. Aerodynamic surfaces are always poorly efficient, as they are usually covered by the separate stream of the hulls [6]. Moreover, in the range of low-to-moderate speeds, the necessary manoeuvre moments can be obtained only with very large deflections of the aerodynamic surfaces, which hence tend to work very close to the stall condition. Last, but not least, conventional airships cannot hover without wind, and even in presence of wind they can hover uniquely aligning the heading in the wind direction.

In order to overcome the problems discussed above, an innovative unmanned Lighter-Than-Air platform has been designed, featuring an ad-hoc command system which should facilitate manoeuvres in forward, backward and sideward flight and hovering with any heading, with or without wind. In particular, this new concept airship should fulfil some important requirements, such as controllability and manoeuvrability, low speed and hovering capabilities, operativity in severe weather conditions, noise emission, ground staff and required facilities, acquisition and operative costs. The final design target consists in achieving a good degree of satisfaction to all the previous requirements, on which fixed-wing aircraft, helicopters and conventional airships undoubtedly present total or partial lacks. For these reasons, the new concept airship has been conceived with a highly non conventional architecture, coupled with a thrust-vectoring command system, which features a completely new piloting philosophy. This airship has been designed to operate as a low-cost multipurpose multimission platform. Once equipped with the appropriate sensors, such as electro-optics, radars and hyperspectral camera, the airship can be used for inland, border and maritime surveillance missions. Provided with the appropriate communication systems, however, it can be easily employed as a communication coverage extension, whenever it is not feasible to rely upon a fixed installation, such as after catastrophic events, or in peace-keeping and military operations.

The purpose of the paper is to give a thorough description of the mathematical model of this unconventional air-vehicle from the flight mechanics point of view. Great emphasis is placed especially on those peculiar aspects of the dynamic modelling, such as the aerodynamics, the aerostatic lift contribution, the inertial characteristics and the propulsive system. The airship dynamic model has been essential for the development of a complete and refined Flight Simulator, with real-time simulation features, which will be thoroughly described in Section 10. The availability of a reliable simulation tool allows firstly to investigate the global dynamic behaviour of this innovative unmanned airship, and then, support its whole design process from the early stages up to the more advanced phases, in which the single components and subsystems have to be correctly analyzed, dimensioned and integrated in the final product.

2 AIRSHIP CHARACTERISTICS

In details, the new concept airship presented in Figure 1 features a double-hull architecture with a central plane housing structure, propellers, on-board energetic system and payload. This configuration allows to reduce the lateral wet surface and consequently the sensitiveness of the air-vehicle to the lateral gusts, providing the same aerostatic lift with respect to the single hull platform. This unconventional airship does not use aerodynamic control surfaces, therefore, the primary command system is based on six propellers, moved by electrical motors, suitably set in order to produce the desired forces and moments, necessary to control and manoeuvre the airship both in hovering and forward flight in the whole flight envelope. In particular, two vertical propellers provide the vertical thrust for climbing, descent and pitching manoeuvres, while four thrust-vectoring propellers mounted on rotating arms allow to control the lateral-directional attitude of the airship. The outstanding feature of this new command system is undoubtedly the capability of hovering and manoeuvring with and without wind. Conventional airships with aerodynamic control surfaces, in fact, can uniquely hover by orienting their nose against the wind to take advantage of the relative airspeed, which makes the aerodynamic surfaces effective to produce the manoeuvring moments. The lift is basically generated by a hybrid system consisting of aerostatic lift, the *buoyancy*, provided by the helium inside the hulls, and the vertical thrust given by the two vertical propellers. In forward flight, the buoyancy is boosted by the aerodynamic lift developed by the double fuse-shaped body of the airship. In addition, this airship is equipped with two *ballonets*, one for each hull, which can be blown up with air and deflated, respectively during the descent and climb operations, in order to handle altitude variations without losing helium from the hulls and avoid any significant change in the hull shape. The variable amount of air inside the ballonets, in fact, compensates the helium volume fluctuations during altitude variations [7].

Landing operations are facilitated by a landing gear system featuring rods connected to a helicoidal gear, which is supported by the lower part of the airship envelope. The main characteristic of this landing device is that the helium inside the hulls can be effectively used as a damper.

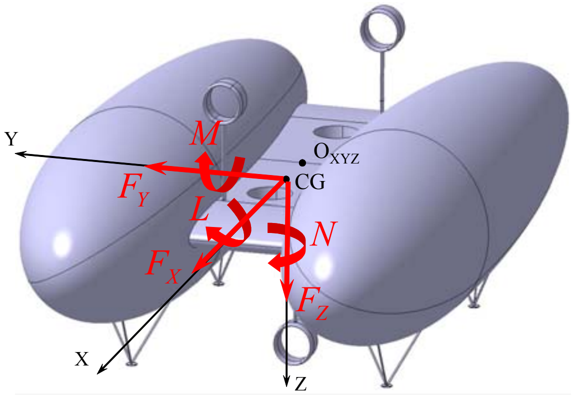

Figure 1 The new concept unmanned airship.

3 BASIC ASSUMPTIONS ON THE AIRSHIP MATHEMATICAL MODELLING

The airship mathematical model is based on a six-degree-of-freedom non linear dynamic model [6], in which the airship is treated as a rigid body without aeroelastic effects and symmetric with respect to the centre-line vertical plane XZ. In particular, the model is described by the Newtonian nonlinear equations of motion, which are expressed through 12 ordinary differential equations (ODEs). This 12-state formulation basically follows the standard dynamic modelling of the conventional aircraft [8] and assumes that the Earth is fixed in space, representing thus an inertial reference frame, and its curvature is neglected. However, the presence of aerostatic lift provided by a huge gas volume and the large volume of air displaced by the airship motion give rise to significant additions to the familiar aircraft equations of motion, such as the buoyancy force B and the apparent mass and inertia terms M_{app}. These equations of motion are referred to the XYZ body-axes reference frame fixed in the Centre of Gravity (CG) of the airship. Due to the airship symmetry, both the CG and the Centre of Buoyancy (CB), in which the buoyancy force B acts, lie in the XZ plane and their coordinates are evaluated in the body-fixed reference frame O_{XYZ}, as shown in Figure 2. Specifically, the CG position (a_X, a_Y, a_Z) is referred to the geometric point O fixed on the central plane in between the two vertical propellers, while the CB coordinates (b_X, b_Y, b_Z) are related to the CG position by means of the following expression:

$$\bar{b} = \begin{bmatrix} x_{CB} - a_X \\ y_{CB} - a_Y \\ z_{CB} - a_Z \end{bmatrix} = \begin{bmatrix} b_X \\ b_Y \\ b_Z \end{bmatrix} \qquad (1)$$

where x_{CB}, y_{CB} and z_{CB} are the CB coordinates with respect to O_{XYZ}, which depend on some flight parameters, such as the altitude, and are gathered into look-up tables for different flight conditions. In this way, they can be evaluated at each time step of the numerical integration of the equations of motion by simply interpolating data in the appropriate look-up tables.

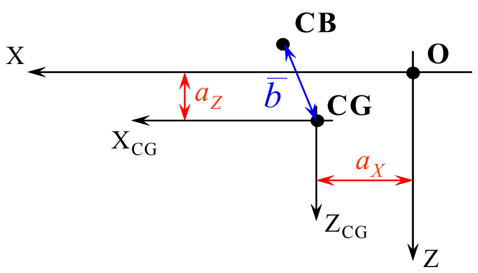

Figure 2 Scheme of the airship reference points.

The general scheme of the airship model is illustrated in Figure 3. The complete state vector $\bar{x}$ consists of twelve elements:

$$\bar{x} = \begin{bmatrix} u & v & w & p & q & r & \phi & \theta & \psi & N & E & H \end{bmatrix}^T \qquad (2)$$

where (u, v, w) are the linear velocities, (p, q, r) are the angular velocities, (ϕ, θ, ψ) are the Euler angles which define the attitude of the airship relatively to the Earth, while (N, E, H) are the coordinates defining the *North-East-Up* position of the airship relatively to the Earth. These twelve state variables can be obtained by integrating their time-derivatives with respect to time through the *Runge-Kutta* numerical integration method. Moreover, the state variables need to be coupled back to all the force and moment equations, as well as to the equations of motion themselves in order to compute their time-derivatives. The inputs of the dynamic model consist of the rotational speeds n_{pr} of all the six propellers and the orientation angles δ_{pr} of the four thrust-vectoring propellers. These inputs exclusively feed the propulsion system and generate the desired propulsive forces and moments needed to manoeuvre the airship. In particular, these signals are generated by the pilot acting on a new concept cockpit that will be described in Section 10.1. Successively, the pilot commands are pre-processed and re-allocated by the Control Allocation System modelled in the Flight Control Computer (FCC) and, finally, are filtered by first order transfer functions that account for the actuator dynamics. The design and tuning of the Control Allocation System [9], [10] has been a crucial issue because of the poor knowledge of the unconventional airship dynamic behaviour. Both the longitudinal and lateral-directional command systems are quite atypical and without historical records, therefore, they have been subjected to intensive studies, carried out through numerical analyses filtered by the pilot opinions during several flight simulations. Finally, the atmospheric data needed to evaluate the aerodynamic, propulsive, buoyancy and gravitational forces are based on the ICAO Standard Atmosphere model.

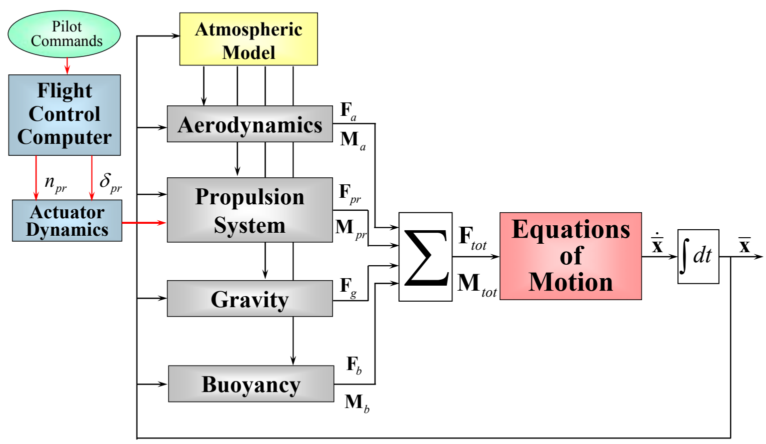

Figure 3 General scheme of the airship model.

4 EQUATIONS OF MOTION

The airship equations of motion are expressed in the non linear state-space format and consist of six force and moment equations, three kinematic equations and three navigation equations. The axial, side and normal force equations and the rolling, pitching and yawing moments equations with respect to the CG reference frame are computed by implementing the Newton's second law of motion for each degree of freedom. In a matricial form it can be written:

$$M\,\dot{\bar{x}}_v = \bar{F}_d + \bar{F} \quad \Rightarrow \quad \dot{\bar{x}}_v = M^{-1}\left(\bar{F}_d + \bar{F}\right) \tag{3}$$

where $\dot{\bar{x}}_v = \begin{bmatrix}\dot{u} & \dot{v} & \dot{w} & \dot{p} & \dot{q} & \dot{r}\end{bmatrix}^T$ is the partial state vector of linear and angular accelerations, M is the total mass matrix, $\bar{F}_d$ and $\bar{F}$ represent respectively the dynamic contributions and the external contributions depending on aerodynamics, static buoyancy, propulsion system and gravitational force:

$$\bar{F}_d = \begin{bmatrix} -m_Z wq + m_Y rv \\ -m_X ur + m_Z pw \\ -m_Y vp + m_X qu \\ -\left(J_Z - J_Y\right)rq + J_{YZ}\left(q^2 - r^2\right) + J_{ZX}pq - J_{XY}pr \\ -\left(J_X - J_Z\right)pr - J_{YZ}pq + J_{ZX}\left(r^2 - p^2\right) + J_{XY}qr \\ -\left(J_Y - J_X\right)qp + J_{YZ}pr - J_{ZX}qr + J_{XY}\left(p^2 - q^2\right) \end{bmatrix} \tag{4}$$

$$\bar{F} = \begin{bmatrix} F_{X_a} + F_{X_b} + F_{X_{pr}} + F_{X_g} \\ F_{Y_a} + F_{Y_b} + F_{Y_{pr}} + F_{Y_g} \\ F_{Z_a} + F_{Z_b} + F_{Z_{pr}} + F_{Z_g} \\ L_a + L_b + L_{pr} \\ M_a + M_b + M_{pr} \\ N_a + N_b + N_{pr} \end{bmatrix} \tag{5}$$

where F_X, F_Y, F_Z are the generic force components in the CG reference frame along the X-, Y- and Z-body axes, while L, M, N are the generic moments around the X-, Y- and Z-body axes respectively, as shown by the red arrows in Figure 1. The terms m_X, m_Y, m_Z and J_X, J_Y, J_Z, J_{XY}, J_{ZX}, J_{YZ} in Equation (4) represent the airship inertial elements contained in the total mass matrix M.

In order to solve the equations of motion of Equation (3), it is also necessary to know the attitude, defined by the Euler angles (ϕ, θ, ψ), and the altitude H of the airship, because some contributions to the external forces and moments $\bar{F}$ of Equation (5) depend upon these flight variables. Moreover, it is useful to evaluate the coordinates of the airship vehicle with respect to the Earth-fixed reference frame to be able to simulate navigational tasks. Firstly, the three kinematic equations defining the airship attitude rates are respectively:

$$\begin{cases} \dot{\phi} = p + \dot{\psi}\sin\theta \\ \dot{\theta} = q\cos\phi - r\sin\phi \\ \dot{\psi} = \dfrac{q\sin\phi + r\cos\phi}{\cos\theta} \end{cases} \tag{6}$$

Secondly, the three navigation equations, computing the Earth-relative airship velocity components along *North*, *East* and *Up* directions, are defined by the following expressions:

$$\begin{cases} \dot{N} = u\cos\theta\cos\psi + v\left(\sin\phi\sin\theta\cos\psi - \cos\phi\sin\psi\right) + \\ \quad + w\left(\sin\phi\sin\psi + \cos\phi\sin\theta\cos\psi\right) \\ \dot{E} = u\cos\theta\sin\psi + v\left(\sin\phi\sin\theta\sin\psi + \cos\phi\cos\psi\right) + \\ \quad + w\left(\cos\phi\sin\theta\sin\psi - \sin\phi\cos\psi\right) \\ \dot{H} = u\sin\theta - \left(v\sin\phi + w\cos\phi\right)\cos\theta \end{cases} \tag{7}$$

5 INERTIAL DATA

The airship total mass matrix M of Equation (3) is defined as follows:

$$M = M_i + M_g + M_{app} \tag{8}$$

The airship inertial data, in fact, have been computed on the assumption that M has to account for three contributions [11]: 1) the mass and inertia terms M_i of all the airship structure components, such as the central plane, the propulsive system, the energetic system and the envelopes; 2) the inertial properties M_g of the gas (helium and air) inside hulls and ballonets; 3) the apparent mass and inertia terms M_{app} arising from the large volumes of air displaced by the airship motion, especially in non stationary conditions. Firstly, the inertial characteristics of the airship structural components are expressed as follows:

$$M_i = \begin{bmatrix} m & 0 & 0 & 0 & 0 & 0 \\ 0 & m & 0 & 0 & 0 & 0 \\ 0 & 0 & m & 0 & 0 & 0 \\ 0 & 0 & 0 & I_{XX} & -I_{XY} & -I_{XZ} \\ 0 & 0 & 0 & -I_{XY} & I_{YY} & -I_{YZ} \\ 0 & 0 & 0 & -I_{XZ} & -I_{YZ} & I_{ZZ} \end{bmatrix} \tag{9}$$

Secondly, the gas inertial contribution can be written as:

$$M_g = \begin{bmatrix} m_g & 0 & 0 & 0 & 0 & 0 \\ 0 & m_g & 0 & 0 & 0 & 0 \\ 0 & 0 & m_g & 0 & 0 & 0 \\ 0 & 0 & 0 & I_{XX_g} & -I_{XY_g} & -I_{XZ_g} \\ 0 & 0 & 0 & -I_{XY_g} & I_{YY_g} & -I_{YZ_g} \\ 0 & 0 & 0 & -I_{XZ_g} & -I_{YZ_g} & I_{ZZ_g} \end{bmatrix} \quad (10)$$

where the elements of the M_g matrix are estimated by modelling the helium/air mass inside hulls and ballonets through the *Catia* CAD code [12]. In particular, the gas inertial characteristics, such as the mass m_g, the centre-of-gravity position (x_g, y_g, z_g) and the inertia moments ($J_{XX_g}, J_{YY_g}, J_{ZZ_g}$) with respect to O_{XYZ}, vary during the ascent or descent manoeuvres and, therefore, have to be evaluated and suitably gathered into look-up tables as functions of two parameters, namely the airship current altitude H and the *plenitude altitude* H_{max} that will be defined subsequently. In this way, it is then possible to compute the gas inertia moments with respect to the airship CG reference frame at each time step of simulation through the Huygens-Steiner formula:

$$\begin{cases} I_{XX_g} = J_{XX_g} - m_g\left[\left(z_g - a_Z\right)^2 + \left(y_g - a_Y\right)^2\right] \\ I_{YY_g} = J_{YY_g} - m_g\left[\left(x_g - a_X\right)^2 + \left(z_g - a_Z\right)^2\right] \\ I_{ZZ_g} = J_{ZZ_g} - m_g\left[\left(x_g - a_X\right)^2 + \left(y_g - a_Y\right)^2\right] \end{cases} \quad (11)$$

The products of inertia I_{XY_g}, I_{XZ_g}, I_{YZ_g} contained in the M_g matrix are assumed to be equal to zero because of the gas symmetrical distribution inside hulls and ballonets.
Finally, the apparent mass and inertia effects are defined by the following matrix:

$$M_{app} = \begin{bmatrix} -X_{\dot u} & -X_{\dot v} & -X_{\dot w} & -X_{\dot p} & -X_{\dot q} & -X_{\dot r} \\ -Y_{\dot u} & -Y_{\dot v} & -Y_{\dot w} & -Y_{\dot p} & -Y_{\dot q} & -Y_{\dot r} \\ -Z_{\dot u} & -Z_{\dot v} & -Z_{\dot w} & -Z_{\dot p} & -Z_{\dot q} & -Z_{\dot r} \\ -L_{\dot u} & -L_{\dot v} & -L_{\dot w} & -L_{\dot p} & -L_{\dot q} & -L_{\dot r} \\ -M_{\dot u} & -M_{\dot v} & -M_{\dot w} & -M_{\dot p} & -M_{\dot q} & -M_{\dot r} \\ -N_{\dot u} & -N_{\dot v} & -N_{\dot w} & -N_{\dot p} & -N_{\dot q} & -N_{\dot r} \end{bmatrix} \quad (12)$$

where all the matrix elements may be considered as added forces and moments, which are described by the dimensional derivatives of aerodynamic forces and moments with respect to linear and angular acceleration perturbations, i.e. $X_{\dot u} = \partial F_{X_a} / \partial \dot u$ or $L_{\dot p} = \partial L / \partial \dot p$. The non dimensional coefficients of these derivatives have been calculated with respect to the O_{XYZ} reference frame by using NSAERO [13], a multi-block computational fluid dynamics code, which solves the Navier-Stokes equations including also the viscous effects. In detail, this code makes use of the fully conservative up-wind formulation and the viscous effects are simulated by coupling the turbulent model to the *Spalart-Allmaras* equation: this is the best compromise between simulation efficiency and computational effort. Before being included into Equation (8), however, the matrix M_{app} must be rewritten with respect to the CG reference frame. This translation can be done on the assumption that the fluid kinetic energy does not depend on the reference frame:

$$\frac{1}{2}\bar{x}_{vCG}^T M_{appCG}\,\bar{x}_{vCG} = \frac{1}{2}\bar{x}_{vO}^T M_{appO}\,\bar{x}_{vO} \quad (13)$$

Furthermore, the velocity vector $\bar{x}_{vO}$ of the body axis origin O can be related to the velocity vector $\bar{x}_{vCG}$ of the airship CG by using the following expression:

$$\bar{x}_{vO} = \left[\begin{array}{c|c} I & A \\ \hline 0 & I \end{array}\right]^{-1} \bar{x}_{vCG} \equiv \left[\begin{array}{c|c} I & -A \\ \hline 0 & I \end{array}\right] \bar{x}_{vCG} \quad (14)$$

where A is the rotational matrix from the O_{XYZ} to the CG reference frame and it is made up by the airship CG coordinates (a_X, a_Y, a_Z):

$$A = \begin{bmatrix} 0 & a_Z & -a_Y \\ -a_Z & 0 & a_X \\ a_Y & -a_X & 0 \end{bmatrix} \quad (15)$$

Finally, from Equation (13) and Equation (14), the apparent mass matrix M_{app} in the CG reference frame results:

$$M_{appCG} = \left[\begin{array}{c|c} I & 0 \\ \hline A & I \end{array}\right] M_{appO} \left[\begin{array}{c|c} I & -A \\ \hline 0 & I \end{array}\right] \quad (16)$$

6 AIRSHIP AERODYNAMICS

The airship aerodynamic modelling is based on the six aerodynamic coefficients ($C_{X_a}, C_{Y_a}, C_{Z_a}, C_{l_a}, C_{m_a}, C_{n_a}$) and the eighteen damping non dimensional derivatives ($C_{X_{p,q,r}}, C_{Y_{p,q,r}}, C_{Z_{p,q,r}}, C_{l_{p,q,r}}, C_{m_{p,q,r}}, C_{n_{p,q,r}}$), which have been computed in the O_{XYZ} reference frame by using the NSAERO code. These coefficients depend on some flight parameters, such as the airspeed, the angle of attack α and the sideslip angle β. In particular, they are estimated at zero altitude on a rough grid for $0 \le \alpha \le 90°$, $0 \le \beta \le 180°$, and at different Reynolds numbers $Re = \rho U l / \mu$, where ρ is the air density, μ is the fluid viscosity, l is a characteristics length and U is the free-stream airspeed. The investigated Reynolds numbers refer to velocities U equal to 2 *m/s*, 4 *m/s*, 8 *m/s*, and 20 *m/s*. The NSAERO data are successively processed, interpolated and extrapolated into thicker grids and more extended ranges of the Reynolds number, the angle of attack (-90° ≤ α ≤ +90°), and the sideslip angle (-180° ≤ β ≤ +180°), in order to obtain suitable 3-D look-up tables, as shown in Figure 4. For airspeeds lower than 2 *m/s* up to $Re = 0$, aerodynamic coefficients are kept constant to the first *Re* condition, i.e. 2 *m/s*. This 360-degree aerodynamic modelling allows the airship dynamic model to handle either hovering or any other forward flight condition and avoid discontinuities in passing from hovering to forward flight. Table I summarizes the data processing carried out on the NSAERO aerodynamic coefficients in order to build the 3-D aerodynamic look-up tables used by the Flight Simulator. Particularly, NSAERO data are upset on the uncalculated ranges of α and β, and their signs are opportunely changed according to the axis conventions.

Table I - Aerodynamic Look-Up Table Processing

$C_{X,Y,Z,l,m,n}$ _matrix	$0 \le \beta \le 180°$ $\quad 0 \le \alpha \le 90°$					
	$C_{X_{NSAERO}}$	$C_{Y_{NSAERO}}$	$C_{Z_{NSAERO}}$	$C_{l_{NSAERO}}$	$C_{m_{NSAERO}}$	$C_{n_{NSAERO}}$
$-180° \le \beta < 0 \quad -90° \le \alpha < 0$	+	-	-	+	-	-
$-180° \le \beta < 0 \quad 0 \le \alpha \le 90°$	+	-	+	-	+	-
$0 \le \beta \le 180° \quad -90° \le \alpha < 0$	+	+	-	-	-	+
$0 \le \beta \le 180° \quad 0 \le \alpha \le 90°$	+	+	+	+	+	+

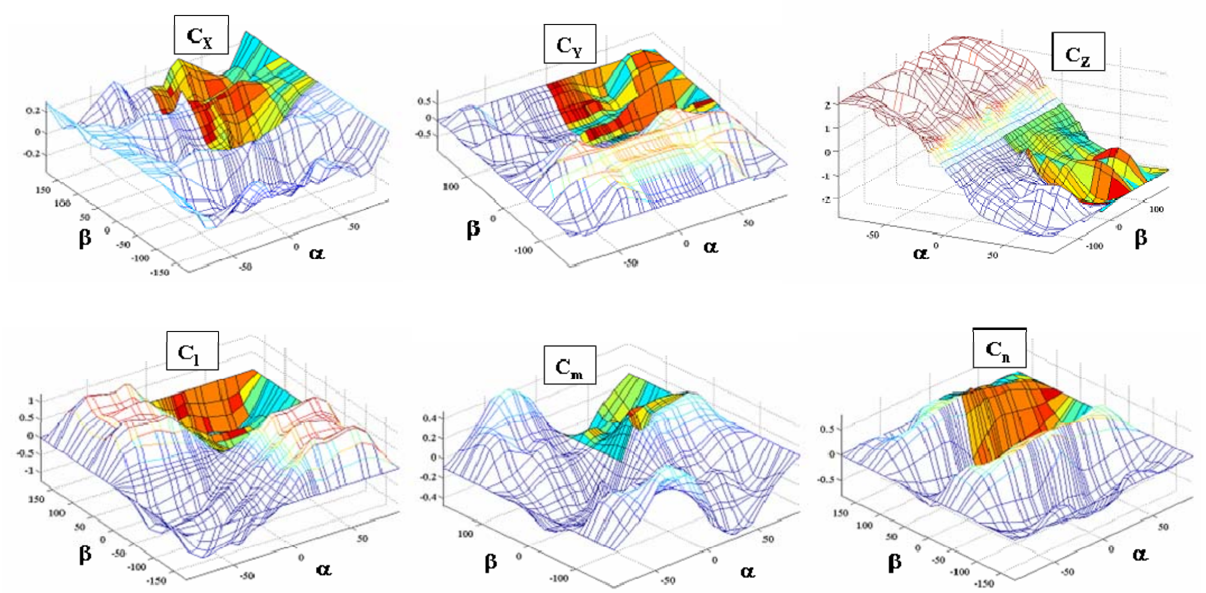

Figure 4 Aerodynamic modelling through 3-D Look-Up Tables.

Finally, the aerodynamic forces and moments can be expressed in the standard notation as follows:

$$\begin{cases} F_{Xa} = \left(C_{X_a} + C_{X_p}\hat{p} + C_{X_q}\hat{q} + C_{X_r}\hat{r}\right)\cdot 1/2\,\rho U^2 V^{2/3} \\ F_{Ya} = \left(C_{Y_a} + C_{Y_p}\hat{p} + C_{Y_q}\hat{q} + C_{Y_r}\hat{r}\right)\cdot 1/2\,\rho U^2 V^{2/3} \\ F_{Za} = \left(C_{Z_a} + C_{Z_p}\hat{p} + C_{Z_q}\hat{q} + C_{Z_r}\hat{r}\right)\cdot 1/2\,\rho U^2 V^{2/3} \\ L_a = \left(C_{l_a} + C_{l_p}\hat{p} + C_{l_q}\hat{q} + C_{l_r}\hat{r}\right)\cdot 1/2\,\rho U^2 V^{2/3} D \\ M_a = \left(C_{m_a} + C_{m_p}\hat{p} + C_{m_q}\hat{q} + C_{m_r}\hat{r}\right)\cdot 1/2\,\rho U^2 V^{2/3} l \\ N_a = \left(C_{n_a} + C_{n_p}\hat{p} + C_{n_q}\hat{q} + C_{n_r}\hat{r}\right)\cdot 1/2\,\rho U^2 V^{2/3} D \end{cases} \tag{17}$$

where $\hat{p} = pb/2U$, $\hat{q} = qc/2U$, $\hat{r} = rb/2U$ are the non dimensional angular velocities, ρ is the air density, U is the free-stream airspeed, V is the airship volume, D is the hull diameter and l, c, b are airship reference lengths. Obviously, these aerodynamic forces need to be properly translated in the CG reference frame through the rotational matrix A, before being integrated in Equation (5):

$$\begin{Bmatrix} \overline{F}_a \\ \overline{M}_a \end{Bmatrix}_{CG} = \left[\begin{array}{c|c} I & 0 \\ \hline A & I \end{array}\right] \begin{Bmatrix} \overline{F}_a \\ \overline{M}_a \end{Bmatrix}_{O} \tag{18}$$

7 BUOYANCY AND GRAVITY

The main contribution to the airship lift is supplied by the aerostatic buoyancy provided by the helium inside the hulls. The two inner *ballonets* can be blown up with air and deflated to handle altitude variations. In particular, air is initially released from ballonets during climb up to the *plenitude altitude* H_{max}, which is the altitude defined before each mission according to the amount of helium contained in the hulls and to which the gas is completely expanded filling the hulls themselves. Beyond the plenitude altitude, helium has to be released from hulls causing the reduction of buoyancy B. Differently, during descent ballonets are blown up by the on-board pneumatic system [7]. Assuming constant pressure and temperature inside the hulls, the buoyancy does not vary from the ground to the plenitude altitude and is expressed as follows:

$$B = V_b \Lambda_{air_0} \left(1 - \frac{1}{\varepsilon_{He}}\right) \tag{19}$$

where V_b is the helium volume, Λ_{air_0} is the specific weight of air at zero altitude and ε_{He} is the air/helium specific weight ratio. If the airship exceeds the plenitude altitude, a given amount of helium is released from the hulls and the buoyancy decreases proportionally to the air specific weight according to the expression:

$$B = V_b \Lambda_{air_0} \frac{p_a T_{K0}}{p_{a0} T_K} \left(1 - \frac{1}{\varepsilon_{He}}\right) \tag{20}$$

where p_a and T_K are respectively the pressure and the temperature of the atmosphere at the current altitude.

The buoyancy action is applied in the CB, whose location, defined by the x_{CB}, y_{CB} and z_{CB} coordinates, changes with the altitude depending on the amount of air contained in the ballonets. In particular, the presence of ballonets and their functioning are mathematically modelled through the variations Δx and Δz of the CB position with respect to the O_{XYZ} reference frame. The lateral shift Δy of the buoyancy is assumed to be negligible, as the pneumatic system is designed to act immediately to compensate the effects that might be caused by the sudden occurrence of a bank angle: an automatic valve, in fact, is expected to close the duct that connects the ballonets, preventing the air to flow from each other. Differently, Δx and Δz are estimated through the *Catia* CAD code by considering an initial air-helium subdivision of the hulls, depending on the plenitude altitude H_{max}, and successively, varying the ballonet volume to simulate the altitude variation [14]. In this way, the current CB position for different air-helium configurations can be evaluated at each time step of the simulation through the estimated variations Δx and Δz, which are shown in Figure 5 for different plenitude altitudes (up to 7000 m) as functions of the actual altitude H. In particular, the negative Δz values point out that the CB is higher than the CG improving the airship lateral stability. Moreover, beyond the plenitude altitude, ballonets are completely deflated, hence Δx and Δz keep constant values. Finally, these longitudinal and vertical variations Δx and Δz are gathered into look-up tables as a function of the current altitude H and the plenitude altitude H_{max}.

The buoyancy force B acts along the Z-Earth axis (*NED* inertial reference frame), thus, it needs to be transferred in the CG body reference frame through the Euler rotational matrix $\{E\}$:

$$\bar{F}_{b_{CG}} = \{E\}\begin{bmatrix} 0 & 0 & -B \end{bmatrix}^T_{NED} \tag{21}$$

$$\{E\} = \begin{bmatrix} \cos\theta\cos\psi & \cos\theta\sin\psi & -\sin\theta \\ -\cos\phi\sin\psi + \sin\phi\sin\theta\cos\psi & \cos\phi\cos\psi + \sin\phi\sin\theta\sin\psi & \sin\phi\cos\theta \\ \sin\phi\sin\psi + \cos\phi\sin\theta\cos\psi & -\sin\phi\cos\psi + \cos\phi\sin\theta\sin\psi & \cos\phi\cos\theta \end{bmatrix} \tag{22}$$

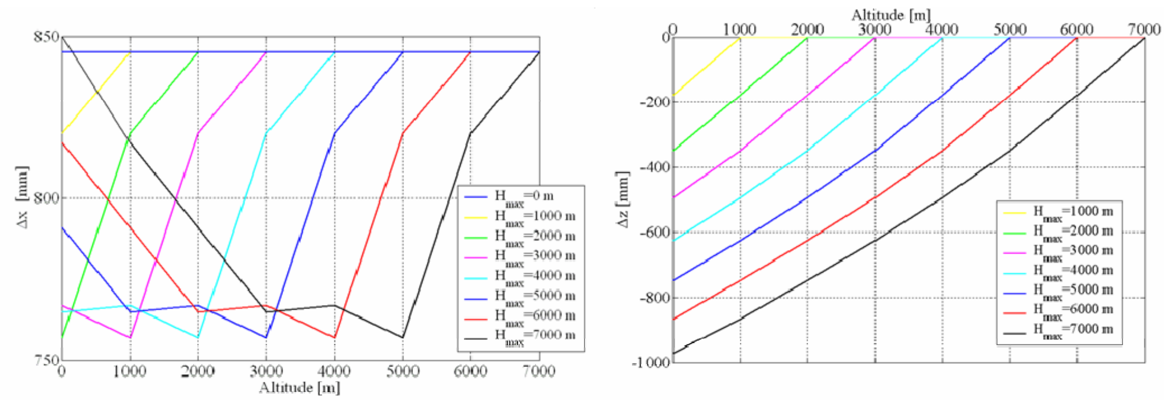

Figure 5 Longitudinal and vertical variations of the CB position with respect to O_{XYZ}.

The buoyancy moments $\bar{M}_{b_{CG}}$ are then computed by means of the CB coordinates (b_X, b_Y, b_Z) of Equation (1) through the following expression:

$$\bar{M}_{b_{CG}} = \bar{b} \wedge \bar{F}_{b_{CG}} = \begin{bmatrix} b_Z B \sin\phi \cos\theta \\ b_Z B \sin\theta + b_X B \cos\phi \cos\theta \\ -b_X B \sin\phi \cos\theta \end{bmatrix} \tag{23}$$

with the assumption that the CB lies in the XZ symmetry plane and, therefore, $b_Y = 0$.
Analogously to the buoyancy force B, the gravitational force $W = mg$ acts along the Z-Earth axis as well and gives rise to the following force components in the CG body reference frame:

$$\bar{F}_{g_{CG}} = \{E\}\begin{bmatrix} 0 & 0 & mg \end{bmatrix}^T_{NED} = \begin{bmatrix} -mg\sin\theta \\ mg\sin\phi\cos\theta \\ mg\cos\phi\cos\theta \end{bmatrix} \tag{24}$$

8 GROUND REACTION

In order to simulate complete missions from take-off to landing, providing the pilot with training realistic manoeuvres, ground reactions are also taken into account by roughly modelling the landing device of the airship. In fact, although the airship is equipped with four retractile landing devices connected to the hulls, the dynamic model features a single landing device placed on the CG location at *4 m* from the ground. In this way, the ground reactions are simply modelled by a single force acting in the airship CG, while the dynamics of the successive touches of the whole landing gear is neglected as well as the airship attitude. At this stage, the model has surely poor capabilities of simulating a realistic landing, but it is effective and sufficient during the take-off. The ground normal reaction can be expressed as follows:

$$F_{GR} = W - B - T_{Z_{NED}} - F_{Z_{a_{NED}}} \tag{25}$$

where W is the airship total weight, B is the buoyancy, $T_{Z_{NED}}$ is the component along the Z-Earth axis of the total propulsive force and $F_{Z_{a_{NED}}}$ is the normal aerodynamic force with respect to the Earth-fixed reference frame. When $H \le 4\,m$, the ground reaction F_{GR} is calculated and as long as it is positive, the airship is considered to be constrained to the ground. Whereas, if $F_{GR} \le 0$ the airship is landing or taking-off and the equations of motion are integrated under the action of aerodynamic, gravitational, propulsive and buoyancy forces and moments.

9 PROPULSIVE SYSTEM

The thrust T of all the six propellers is modelled through the first *Rènard* formula [15]:

$$T = \tau\,\rho\omega^2 R^4 \tag{26}$$

where ρ is the air density, R is the radius and ω is the angular rate of the propeller. τ represents the thrust coefficient, which is a function of the propeller working point $\gamma = U_{AX}/\omega R$, as illustrated in Figure 6 for both vertical (*VT*) and thrust-vectoring propellers (*FW*):

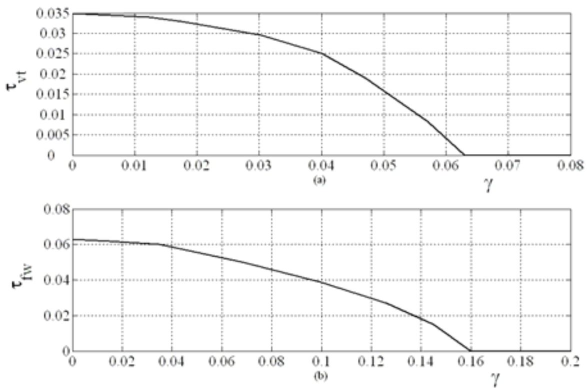

Figure 6 Thrust Coefficient – (a) vertical propellers (b) thrust-vectoring propellers.

The term U_{AX} in the working point expression represents the axial airspeed component at the propeller disc along its rotational axis. U_{AX} can be estimated by calculating the velocity vector $\bar{v}_{pr} = \{u_{pr}\ v_{pr}\ w_{pr}\}^T$ of the airship rigid body at the propeller-disc center:

$$\bar{v}_{pr} = \bar{v}_{CG} + \bar{\Omega} \wedge \bar{l}_{pr} \tag{27}$$

where $\bar{\Omega}$ is the angular rate vector (p, q, r) and $\bar{l}_{pr}$ defines the location of the propeller disc with respect to the CG reference frame. For the four thrust-vectoring propellers with generic orientation δ, the component U_{AX} will be expressed as follows:

$$U_{AX} = u_{pr}\cos\delta + v_{pr}\sin\delta \tag{28}$$

while for the two vertical propellers it will be $U_{AX} \equiv w_{pr}$.

The command input n_{pr} acts on the propeller angular rate ω commanding the magnitude of the propeller thrust T according to Equation (26). In addition, all the propellers can work in reverse mode with reduced efficiency $\eta < 1$. The orientation δ of each of the four thrust-vectoring propellers is generated by the second command input δ_{pr}, which represents the result of the pilot action on longitudinal, lateral and directional commands, then processed by the Control Allocation System. Figure 7 shows the disposition of the six propellers in the airship central plane. In particular, there are four thrust-vectoring propellers in asymmetrical positions: front up (*FU*), front down (*FD*), rear up (*RU*), rear down (*RD*); while the two vertical ducted propellers are in the fore (*VF*) and aft (*VA*) part of the central plane. Combining together the longitudinal, lateral and directional commands, the axial, side and normal components of the total propulsive force referred to the O_{XYZ} reference frame can be computed by adding up the contributions of all the propellers:

$$\begin{cases} F_{X_{pr}} = T_{FU}\cos\delta_{FU} + T_{RD}\cos\delta_{RD} + T_{RU}\cos\delta_{RU} + T_{FD}\cos\delta_{FD} \\ F_{Y_{pr}} = T_{FU}\sin\delta_{FU} + T_{RD}\sin\delta_{RD} + T_{RU}\sin\delta_{RU} + T_{FD}\sin\delta_{FD} \\ F_{Z_{pr}} = -T_{VT} - T_{VA} \end{cases} \tag{29}$$

Consequently, the total propulsive moments around O_{XYZ} are given by the expression:

$$\bar{M}_{pr} = \bar{F}_{pr} \wedge \bar{l}_{pr0} \equiv \begin{bmatrix} 0 & F_{Z_{pr}} & -F_{Y_{pr}} \\ -F_{Z_{pr}} & 0 & F_{X_{pr}} \\ F_{Y_{pr}} & -F_{X_{pr}} & 0 \end{bmatrix} \cdot \begin{Bmatrix} x_{pr0} \\ y_{pr0} \\ z_{pr0} \end{Bmatrix} \tag{30}$$

where $\bar{l}_{pr_0}$ represents the position vector of each propeller with respect to O_{XYZ}. Finally, $\bar{F}_{pr}$ and $\bar{M}_{pr}$ have to be transferred in the CG body reference frame in order to be included in Equation (5):

$$\begin{Bmatrix} \bar{F}_{pr} \\ \bar{M}_{pr} \end{Bmatrix}_{CG} = \left[\begin{array}{c|c} I & 0 \\ \hline A & I \end{array}\right] \begin{Bmatrix} \bar{F}_{pr} \\ \bar{M}_{pr} \end{Bmatrix}_{O} \tag{31}$$

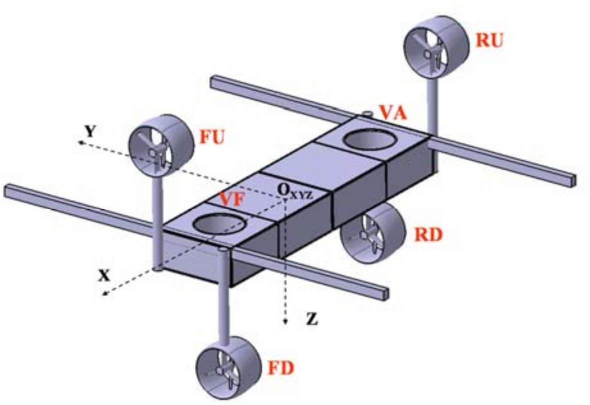

Figure 7 Scheme of the primary control system.

10 FLIGHT SIMULATOR

The airship dynamic model, which has been deeply described in the previous Sections, defines the most peculiar features of the airship from the flight mechanics point of view and represents the kernel of a complete and reliable Flight Simulator. The development of this Flight Simulator is essential to support the whole design process of the unconventional lighter-than-air vehicle and provide an effective expository platform for the subsequent marketing operations. In particular, this Simulator is initially employed to evaluate the unknown dynamic behaviour of the airship and then, it has to support the design and test phases of a completely new flight control system, as well as its implementation into the on-board computer by means of innovative techniques based on real-time rapid prototyping and hardware-in-the-loop simulations. In addition, the Flight Simulator should supply a powerful tool for the pilot during the training phase of this non conventional remotely-piloted airship featuring extremely peculiar characteristics. In fact, although the piloting has been reckoned to emulate as much as possible the helicopter concept, a worthwhile training phase is necessary to get used to the airship response and achieve the best performance from its great capabilities.

The simulation code of the Flight Simulator has been developed in the *Matlab*/*Simulink* environment and basically consists of two main blocks: the airship dynamics, mathematically modelled in the previous Sections, and the Flight Control Computer (FCC), in which the Control Allocation System has been implemented. Piloting devices, graphic interface and real-time simulation features of the Flight Simulator will be carefully investigated in the next Sections.

10.1 THE COCKPIT

The control procedure is carried on by the pilot action performed through a dedicated cockpit, consisting of a multi-function throttle and a three-degree-of-freedom joystick, both equipped with a series of buttons, switches, levers and knobs, as shown in Figure 8. In details, the *Joystick* commands either the orientation of the four thrust-vectoring propellers for the lateral and directional manoeuvres or a differential variation of the rotational speed of all the six propellers for the longitudinal manoeuvres. The main throttle, *Throttle 1*, commands the rotational speed of the two vertical axis propellers for quick climb and descent manoeuvres. *Throttle 2*, that is the slider control on the throttle device, acts on the collective rotational speed of the four thrust-vectoring propellers for the forward propulsion. In addition, a hat switch, placed on the throttle device, commands the reverse working of the four thrust-vectoring propellers in order to slow down the airship motion and rapidly allow either a hovering condition or an easy landing. Finally, a dedicated *Knob*, that is the rotary control with build-in button placed on the throttle device, allows the collective orientation of the four thrust-vectoring propellers along the wind direction within the 360 degrees and its successive reset. This new and primitive cockpit has been designed and customized according to practical rules, set by the regulations, which have been then integrated by the pilot suggestions. In particular, this cockpit is initially intended to be used in the

Flight Simulator and, subsequently, in the Ground Station [10] of the real remotely-controlled airship. In fact, the Ground Station should be realized as close as possible to the Flight Simulator in order to maintain the same operational environment used by the pilot during the training phase. In this context, both the Simulator and the real airship should be piloted with two hands, and for no reason the pilot should be prevented from acting simultaneously on all the commands, if this is required by the contingent situation.

Figure 8 New concept cockpit.

10.2 THE VISUAL INTERFACE

The Flight Simulator adopts *Microsoft® Flight Simulator 2004* (FS2004) for graphical display and real-time pilot interactions. This visual interface is based on some add-on software packages, such as *FSUIPC* and *WideFS*, which are developed by third parts and allows the remote connection between FS2004 and any other external application through the Ethernet protocol. Furthermore, the connection between FS2004 and the *Matlab/Simulink* environment, in which the airship mathematical model and its control allocation system have been implemented, is carried out through an opportune *S-Function*-based interface in *C++* code, which is inserted as a block in the *Simulink* scheme of the Flight Simulator. These few expedients allow the remote interaction between the numerical simulation of the *Matlab/Simulink* airship model and its visual interface in a very simple way achieving a refined and low-cost flight simulator for the Nautilus innovative unmanned airship.
In addition, the *Software Development Kit* of FS2004 provides the 3-D modelling and animation tool *g-max* for the accomplishment of the 3-D airship model, which can be used to customize the graphical display. FS2004 gives the user the ability to choose, configure and/or modify the mode of graphical operation through setup menus and different camera views, such as from the control tower, from the cockpit and from any other specific position relatively to the vehicle, as shown in Figure 9.

10.3 THE REAL TIME SIMULATION

Since the Flight Simulator has to support the design, development and test of the innovative flight control system that will be integrated in the airship on-board computer, real-time rapid prototyping and hardware-in-the-loop simulation techniques are used for the testing of the embedded control software during its development. In order to perform realistic hardware-in-the-loop simulations, the entire Flight Simulation has been organized into four separate entities, properly connected within the *Matlab/Simulink* simulation environment. In particular, the four entities concern the airship mathematical model, the FCC, the ground station and the data-link device (receiver and transmitter). As the dynamic system simulation is a non-real-time application which has to be interfaced with the embedded real-time control system, the *Simulink* model has to be converted into a real-time simulation. This operation can be accomplished by using the low-cost automatic code generator RT-LAB™, which generates C code through *Real-Time Workshop*, compile this code in *QNX* and executes it on one or more PC processors running in parallel, which represent the *Targets*. As shown in Figure 10, the Flight Simulator features two *Targets* in the remote station, respectively the airship dynamic model and the FCC, which are equipped with the appropriate I/O interface cards and communicate with the pilot station via Ethernet network. The pilot station includes the cockpit, two monitors, displaying different view of the flying airship, and a *Console* laptop. The *Console* commands the real-time simulation running on the two *Targets*, interacts with the graphical motor based on *Microsoft® Flight Simulator 2004* and displays a virtual cockpit for the pilot. In addition, the up-down link device is simulated by a commercial wireless network, which allows the communication between the ground station and the FCC.

REFERENCES

[1] Elfes A., Bueno S.S., Bergerman M., Ramos J.Jr.G., A Semi-Autonomous Robotic Airship for Environmental Monitoring Missions. *Proceedings of the International Conference on Robotics & Automation*, IEEE, pp. 3449-3455, 1998.

[2] Zaugg D.A., Arnold D.V., Jensen M.A., Ocean Surface and Landside Probing with a Scanning Radar Altimeter. *Proceedings of the Int. Geoscience and Remote Sensing Symposium*, IEEE, Vol. 1, pp. 120-122, 2000.

[3] Hain J.H.W., Lighter-than-air Platforms (Blims and Aerostats) for Oceanographic and Atmospheric Research and Monitoring. *Proceedings of the Oceans MTS Conference and Exhibition*, IEEE, Vol. 3, pp. 1933-1936, 2000.

[4] Dorrington G.E., Development of an airship for tropical rain forest canopy exploration. *The Aeronautical Journal*, Vol. 109, No. 1098, pp. 361-372, 2005.

[5] Valera J.L., Some Remarks on the Conceptual Design of a Heavy Lift Cargo Transporter. *Proceedings of the 14th AIAA Lighter-Than-Air Technical Committee Convention & Exhibition*, AIAA, Reston, VA, 2001.

[6] Khoury G.A., Gillett J.D., *Airship Technology*. Cambridge University Press, 1999.

[7] Battipede M., Lando M., Gili P.A., Vercesi P., Peculiar Performance of a New Lighter-Than-Air Platform for Monitoring. *Proceedings of the AIAA Aviation Technology , Integration and Operation Forum*, AIAA, Reston, VA, 2004.

[8] Stevens B.L., Lewis F.L., *Aircraft Control and Simulation*. John Wiley & Sons, Inc., New York, 1992.

[9] Battipede M., Gili P.A., Lando M., Control Allocation System for an Innovative Remotely-Piloted Airship. *Proceedings of the AIAA Atmospheric Flight Mechanics Conference*, AIAA, Reston, VA, 2004.

[10] Battipede M., Gili P.A., Lando M., Ground Station and Flight Simulator for a Remotely-Piloted Non Conventional Airship. *Proceedings of the AIAA Guidance, Navigation and Control Conference*, AIAA, Reston, VA, 2005.

[11] Thomasson P.G., Equations of Motion of a Vehicle in a Moving Fluid. *Journal of Aircraft*, Vol. 37, No. 4, pp. 630-639, 2000.

[12] CATIA V5R12, *3-D CAD Software Package*, Ver. 5, Dassault Systèmes S.A., 2003.

[13] NSAERO, *Advanced Fluid Dynamics Software*, Analytical Methods, Inc., Redmond, WA.

[14] Battipede M., Gili P.A., Lando M., Massotti L., Flight Simulator for the Control Law Design of an Innovative Remotely-Piloted Airship. *Proceedings of the AIAA Modelling and Simulation Technologies Conference*, AIAA, Reston, VA, 2004.

[15] Lausetti A., Filippi F., *Elementi di Meccanica del Volo - Vol. I*. Levrotto & Bella, Torino, 1955.

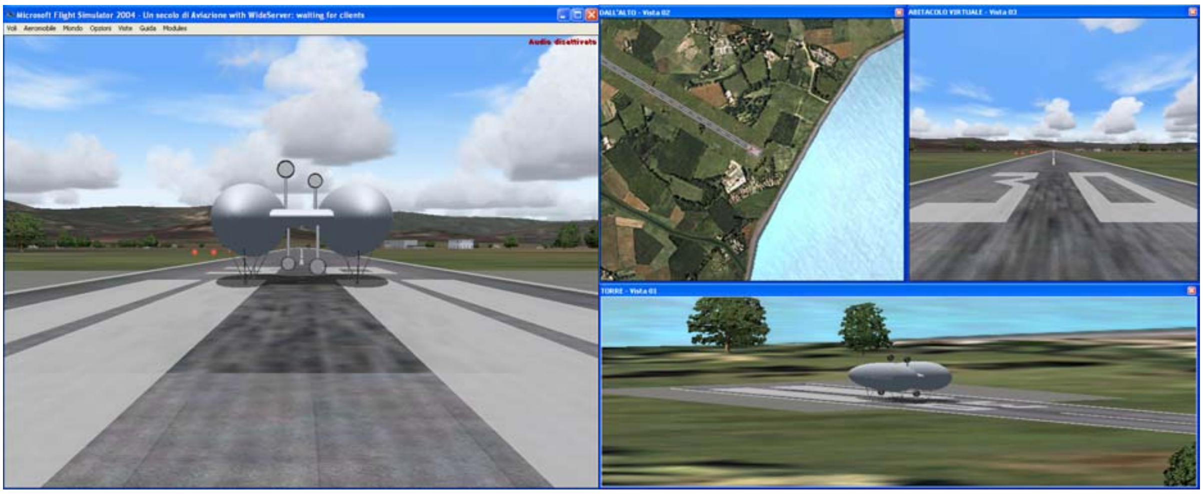

Figure 9 Different camera views within FS2004.

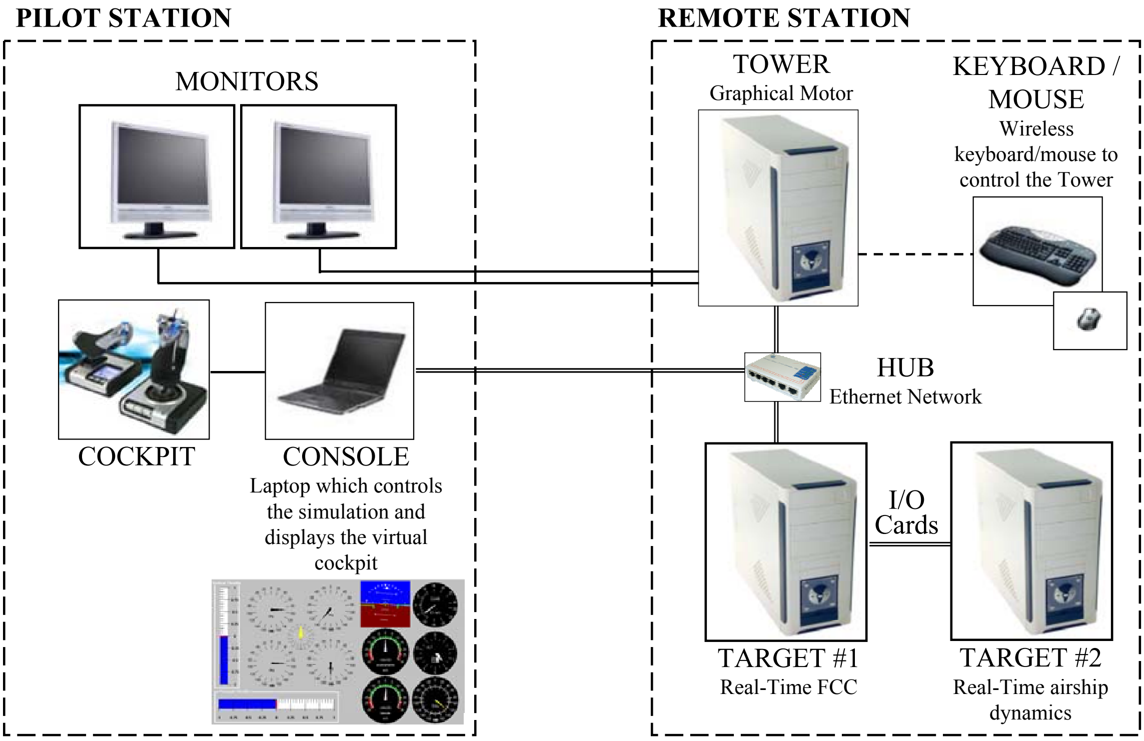

Figure 10 Flight Simulator hardware architecture.

ISSN 1590-8844
International Journal of Mechanics and Control, Vol. 07, No. 01, 2006

TRIBOLOGICAL BEHAVIOUR OF THE TOOL-WORKPIECE KINEMATIC PAIR IN MACHINING OF IMPREGNATED SINTERED MATERIALS

P. Buonadonna G. Dionoro

Department of Mechanical Engineering, University of Cagliari, Italy

ABSTRACT

The results of front-end turning tests performed on porous materials preimpregnated in the cutting zone with a rosin solution in ethanol are presented. Impregnation substantially improves some tribological properties of the tool-workpiece kinematic pair, such as wear and energy dissipation during machining. Tool wear during machining is known to reduce tool-workpiece interference. Thus it was necessary to introduce a geometric correction parameter, so that the quantity measured could be referred to the unit area of the chip removed. Analysis of the experimental results has shown that machining of porous materials undeniably benefits from localised impregnation in the cutting zone, opening up new opportunities for simple low-cost industrial applications.

Keywords: Machinability, PM materials, tool wear, surface finishing

1 INTRODUCTION

It is a well known fact that sintered materials are fairly refractory to machining, subjecting the tool-workpiece kinematic pair to severe tribological stress. This matter has received pour attention by researches, therefore many scientific papers can't be found in literature. This drawback is generally associated with the porosity of these materials, which is where they differ mostly from bulk materials [1, 2].

All other conditions being equal, the presence of pores reduces the volume of material to be machined (conventionally known as volume of undeformed chip) implying that porous materials have lower cutting forces than bulk materials. However, experimental data have repeatedly shown sintered materials to actually have higher forces and moments compared to their solid counterparts, poor surface finish and to induce rapid tool wear.

Contact author: P. Buonadonna[1], G. Dionoro[2]

[1]Dept. of Mechanical Engineering, Univ. of Cagliari, P.zza d'Armi, 09123 – Cagliari, Italy,
E-mail: buonadon@unica.it

[2]Dept. of Mechanical Engineering, Univ. of Cagliari, P.zza d'Armi, 09123 – Cagliari, Italy,
E-mail: dionoro@unica.it

Briefly, this can be attributed to the following experimentally observable phenomena:

- tool chatter produced during machining by the alternation of voids and solid particles in the matrix;
- additional plastic deformation work due to the compressibility of the pores in the material;
- a complex phenomenon known as powdery chip formation.

As far as tool chatter is concerned, the pores of a sintered material (PM) cause the tool edge to impact repeatedly against the surface, resulting in premature tool wear. Wear is also accelerated by the fact that porosity reduces thermal conductivity [3]. The prevailing phenomenon however is material discontinuity which induces much greater chatter than non-porous materials.

Regarding plastic deformation work, the partial or total pore compressibility of the sintered compacts subjected to machining modifies the apparent density of the chips formed. Consequently, considering apparent volumes, the phenomenon involved in PM machining can no longer be construed as constant-volume plastic deformation and for this reason the chip formation model for PM machining needs to be partially reformulated.

Lastly, powderiness, which will depend on the kinematic conditions established during machining, is created by minute fragments of powdery chips that are extruded between the tool major flank and machined surface, causing

additional deformation work. Powderiness impairs the surface finish, zones where the metal has been torn away alternating with others where the chips form burrs.
Briefly, sintered powder compacts have far greater shear strength than bulk materials and result in shorter tool life. Other investigations [4, 5] have shown that for sintered compacts additional energy has to be expended in plastic deformation of the chip fragments that work their way between the tool back and machined surface.
Moreover, by filling the pores with a liquid substance, thus making them incompressible, the tool chatter produced during machining by the alternation of voids and solid material can be reduced and actually eliminated, such that they behave in a similar fashion to bulk materials.
However, it should be recalled that the impregnating substance acts essentially as a lubricant for the tool-chip kinematic pair, as evidenced by the macrographs taken of the tool after machining.

2 EXPERIMENTAL

Face turning tests were performed on cylinders made of sintered iron and of a copper-iron alloy (2% Cu). Copper is an essential element in the manufacture of sintered steel parts and the percentage of alloy had been established earlier as the most appropriate for detecting any overheating in the cutting zone [2, 6]. The ASC 100 29 powder, produced by atomisation, was supplied by Höganas. By varying pressure we obtained three densities: low (6.0 Mg/m^3), medium (6.5 Mg/m^3) and high (7.0 Mg/m^3), that practically cover the entire range of applications.
After pressing, the specimens were sintered in a continuous furnace at 1120° C for 20 minutes under endogas methane atmosphere (dew point = -10° C). The 40 mm high cylindrical workpieces had a diameter of 100 mm.
The tool used in the tests was an uncoated carbide triangular (T) insert with a cutting edge length of 11.0 mm, nose radius of 0.4 mm, rake angle of 5°, back rake angle of 0° and side cutting edge angle of 9.5°.A saturated solution of rosin dissolved in ethanol was used as impregnating substance. This was found to be the most suitable lubricant for local application, confined to the cutting zone [7, 8] and also has the advantage that neither of its two constituents are harmful to human health and are readily and cheaply available.
Three different impregnation methods were used:

- coating the work surface in a horizontal position and waiting for 2 minutes before machining;
- coating the hot, previously machined work surface already mounted on the mandrel and turning immediately;
- coating the work surface with the workpiece already mounted on the mandrel and cooling with compressed air prior to machining.

Each specimen previously characterized for density, chemical composition and impregnation method was machined using a new tool. Cutting parameters were as follows:
depth of cut, p = 0.5 mm;
feed rate, a = 0.015 mm/rev;
spindle angular velocity, n = 2200 rev/min;
maximum cutting speed, $V_t max \approx 691$ m/min (≈ 11.5 ms^{-1});
for a total of 72 tests.
Turning was done with a conventional parallel lathe driven by a single three-phase asynchronous motor.
Cutting force was measured using a pair of strain gauges in a bridge circuit mounted on two perpendicular faces of the tool-holder.
Machine power was indirectly measured by means of the electric motor's supply voltage and current (Figure 1). The essential assumption is that the portion of electric power absorbed by the motor, for non-machining related phenomena, is practically constant and can therefore be easily eliminated. In fact, the stability of the angular velocity of an asynchronous motor, the power losses due to machine operation, the machine power required to rotate the workpiece and the power dissipated by friction in the kinematic chain, to a good approximation remain constant during each test. The instantaneous power in a three-phase motor, supplied by a three-phase, three wire system, can be calculated using the ARON equation. So it is sufficient to know the instantaneous values of the three phase voltages and of two line currents. Denoting with E_1, E_2, E_3 measured phase voltage and with I_1 e I_2 measured line current, we can write:

$$P(t) = [E_1(t) - E_3(t)]\cdot I_1(t) + [E_2(t) - E_3(t)]\cdot I_2(t) \,. \quad (1)$$

A resistive voltage divider for measuring each phase was used. The dividers were connected obtaining an abstract star point which was then taken as ground node for the data acquisition system. Current was measured using two Hall effect TELCON HTP 25 transducers. The analogical values were then sampled directly using a National Instrument LABPC+ acquisition card. Sampling frequency was set at 5 kHz. A virtual instrument was developed for data processing and presentation in real time using LabVIEW software.

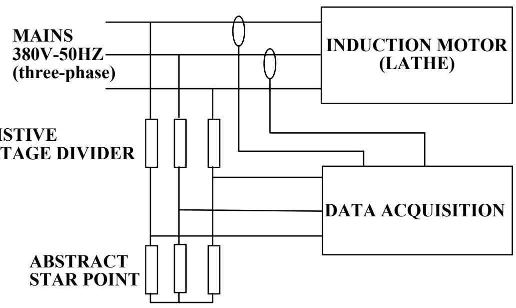

Figure 1 Schematic diagram of power acquisition.

After each test tool wear was measured, determining L_1, L_2, L_3, L_4, L_5, L_6, shown in Figure 2, with the optical part of a microdurometer and then macrophotographing the worn part of the tool.

ISSN 1590-8844
International Journal of Mechanics and Control, Vol. 07, No. 01, 2006

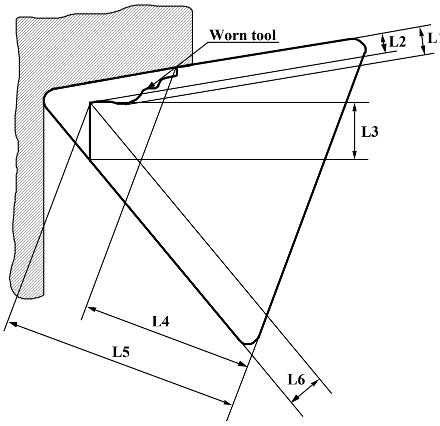

Figure 2 Wear measurements.

3 RESULT AND DISCUSSION

As was to be expected, machining of impregnated and non-impregnated surfaces produced different results and the lower the density of the sintered compacts, and consequently the greater the amount of impregnating substance used, the more substantial these differences are.
Tables I and II give the mean and standard deviations of cutting forces for all the experiments.
Figure 3 shows one of the most meaningful tests. For all tests measured data have been corrected for the error due to heating of the strain gauge mounted on the tool holder. The macrographs of Figure 4 show tool wear after machining the sintered compacts whose cutting forces are reported in Figure 3. As can be observed, tool wear differs significantly for the impregnated and non-impregnated surface and in the latter case the tool nose is completely worn out. This would appear to support the hypothesis advanced in the introduction that the reduction of cutting force is more attributable to the lubricating effect of the impregnating substance than to pore deformation.

Table I - Cutting forces mean values and standard deviation. Material = Fe

Specimen	Density [Mg/m^3]	Mean [N]	St. dev. [N]
Dry 13	6.0	-1890	108
Impr. 13B	6.0	-612	84
Impr. 14B	6.0	-307	6
Dry 23	6.5	-826	1146
Impr. 23B	6.5	-606	464
Impr. 24B	6.5	-412	509
Dry 33	7.0	-856	283
Impr. 33B	7.0	-1772	162
Impr. 34B	7.0	-1079	542
Dry = Not impregnated			
Impr. …*B = impregnated			
* = 3: Machined about 2 min after impregnation on test bench			
* = 4: Machined about 2 min after second impregnation with hot workpiece mounted on mandrel			

Table II - Cutting forces mean values and standard deviation. Material = Fe + Cu 2%

Specimen	Density [Mg/m^3]	Mean [N]	St. dev. [N]
Dry 43	6.0	-1151	22
Impr. 43B	6.0	-751	30
Impr. 44B	6.0	-182	352
Impr. 45B	6.0	-441	106
Dry 53	6.5	-679	1129
Impr. 53B	6.5	-1221	755
Impr. 54B	6.5	-842	293
Impr. 55B	6.5	-441	248
Impr. 56B	6.5	-970	261
Dry 63	7.0	-1558	32
Impr. 63B	7.0	-1349	119
Impr. 64B	7.0	-1282	190
Impr. 65B	7.0	-1326	78
Dry = Not impregnated			
Impr. …*B = impregnated			
* = 3: Machined about 2 min after impregnation on test bench			
* = 4: Machined about 2 min after second impregnation with hot workpiece mounted on mandrel			
* = 5: Machined about 2 min after third impregnation with workpiece mounted on mandrel after cooling with compressed air			

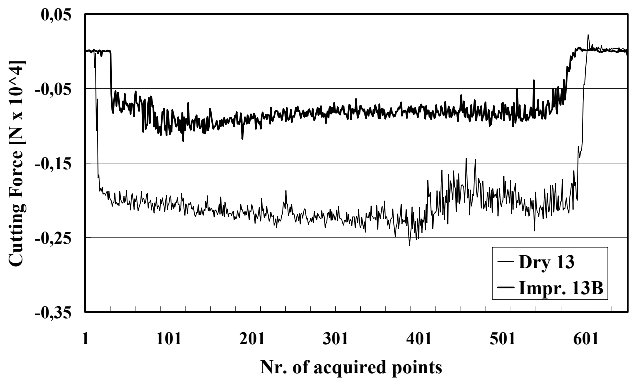

Figure 3 Cutting force vs. time (for explanation of symbols, see Tables I and II).

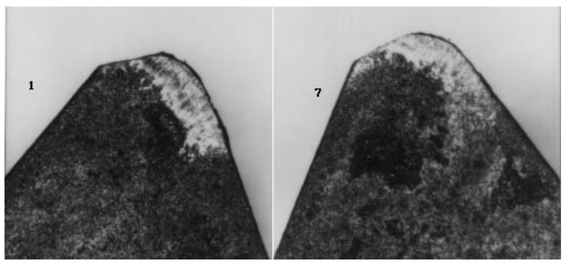

Figure 4 Macrographs of worn tool. Material: Fe; density: 6 Mg/m^3; 1 = Dry; 7 = Impregnated.

Figure 5 shows absorbed power of the motor during machining. A similar trend was observed in all the tests, more or less irregular, depending on specimen density and chemical composition.

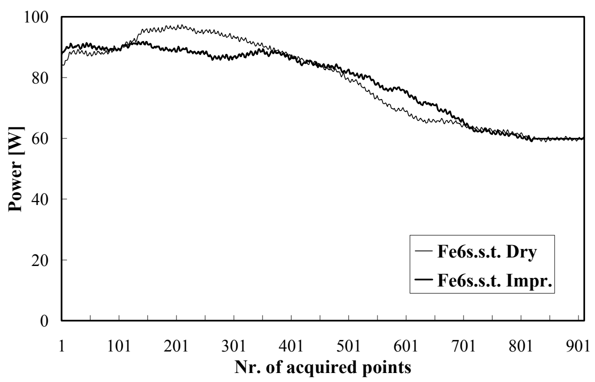

Figure 5 Power vs. time. Material: Fe; density: 6 Mg/m^3.

The apparent incongruity of the higher power required, from a certain point onwards, for machining the impregnated surface, can be explained by the fact that the figure does not allow for the decrease in cutting depth, and consequently undeformed chip area, as tool wear increases. For this reason we found it useful to refer power to the unit area of the chip using the method illustrated below [9, 10].

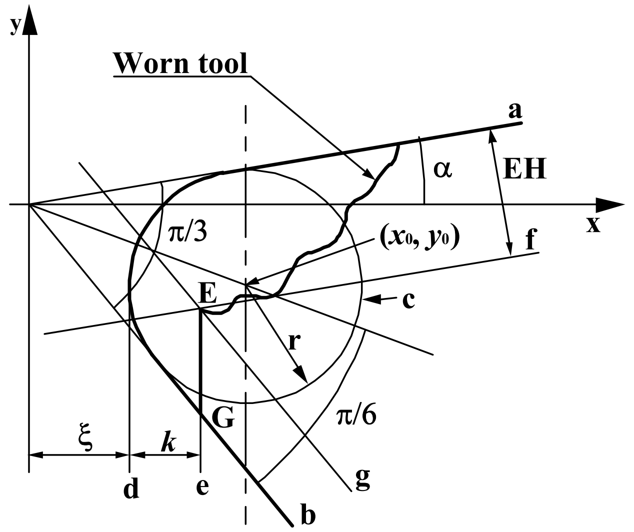

Figure 6 Method for determining actual cutting depth for worn tool.

Using the reference system depicted in Figure 6, the equations for the straight lines representing the cutting edges, the relative circumference of tool nose and of the straight lines passing through some characteristic points of the wear profile can be written:

a: $y = \tan\alpha \cdot x$, (2)

b: $y = -\tan(\pi/3 - \alpha)\cdot x$, (3)

c: $(x - x_0)^2 + (y - y_0)^2 = r^2$, (4)

d: $x = \xi = x_0 - r$, (5)

e: $x = \xi + k$, (6)

f: $y = \tan\alpha \cdot x - \left(\overline{EH}/\cos\alpha\right)$, (7)

g: $y = -\tan(\pi/3 - \alpha)\cdot x + \overline{EG}$. (8)

Segments $\overline{EH}$ and $\overline{EG}$ coincide respectively with L_2 and L_3 of Figure 2.
Combining Equation (8) with Equation (7), the abscissa x_E is obtained:

$$x_E = \left(\overline{EG} + \overline{EH}/\cos\alpha\right)/\left[\tan\alpha + \tan(\pi/3 - \alpha)\right]. \quad (9)$$

Combining Equation (2) with (4) and Equation (3) with (4) and imposing the tangency condition, the coordinates of the centre of circumference representing the tool nose are obtain:

$$x_0 = r\left[\cos(\pi/6 - \alpha)/\sin(\pi/6)\right], \quad (10)$$

$$y_0 = r\left[\sin(\pi/6 - \alpha)/\sin(\pi/6)\right]. \quad (11)$$

Knowing r (= 0.4 mm) and α (= 9.5°), the value of k using the equation can be calculated:

$$k = x_E - \xi = x_E - x_0 + r . \quad (12)$$

Table III shows the values of k for all the tests.

Table III - Geometric tool wear parameters.

Material	Impr.	Density [Mg/m^3]	EG [mm]	EH [mm]	*K* [mm]
Fe	Y	6.0	0.405	0.332	0.188
Fe	Y	6.5	0.364	0.400	0.208
Fe	Y	7.0	0.338	0.370	0.203
Fe+Cu 2%	Y	6.0	0.152	0.400	0.055
Fe+Cu 2%	Y	6.5	0.360	0.400	0.205
Fe+Cu 2%	Y	7.0	0.360	0.446	0.239
Fe	N	6.0	0.368	0.320	0.152
Fe	N	6.5	0.344	0.384	0.182
Fe	N	7.0	0.336	0.396	0.185
Fe+Cu 2%	N	6.0	0.145	0.400	0.049
Fe+Cu 2%	N	6.5	0.304	0.338	0.156
Fe+Cu 2%	N	7.0	0.400	0.384	0.222

Assuming for the sake of simplicity that the value of k increases linearly towards the centre, where it attains the maximum value calculated above, the latter value can be divided by the number of acquired points, to determine the extent of tool wear for each value of power measured during machining. Knowing the measured power W which is referred to the actual area of the chip, the power W' can be calculated referred to the unit area of the undeformed chip, which is equal to 0.0075 mm^2, as:

$$W' = W / [p - k(n)] \cdot a , \quad (13)$$

where p, a and k(n) are depth of cut, feed rate and tool wear in the point considered.

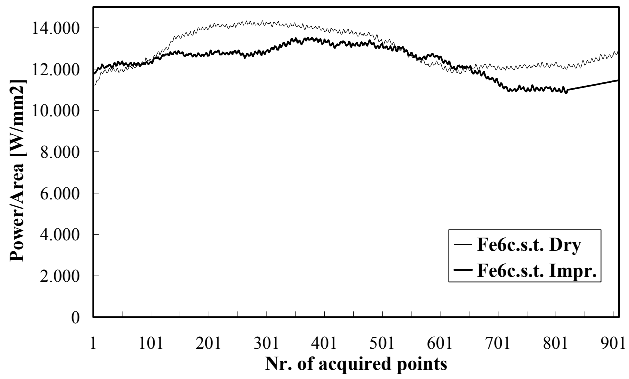

Figure 7 Corrected Power vs. time. Material: Fe; density: 6 Mg/m^3.

The power diagrams, thus corrected, versus time, overcome the incongruity mentioned earlier (Figure 7) and this emerges even more clearly when the data are linearly interpolated (Figure 8), which would seem a more correct approach, insomuch as all the accidental phenomena are eliminated, especially those due to tool chatter.

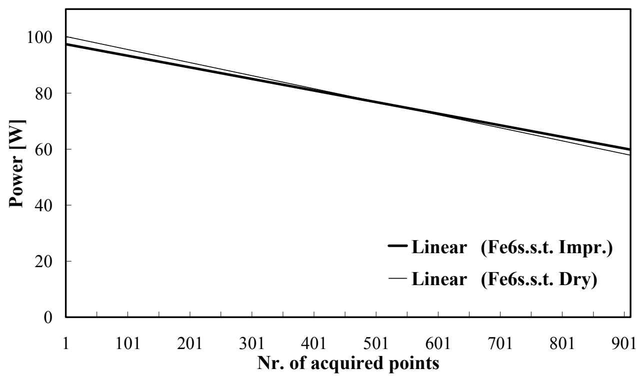

(a)

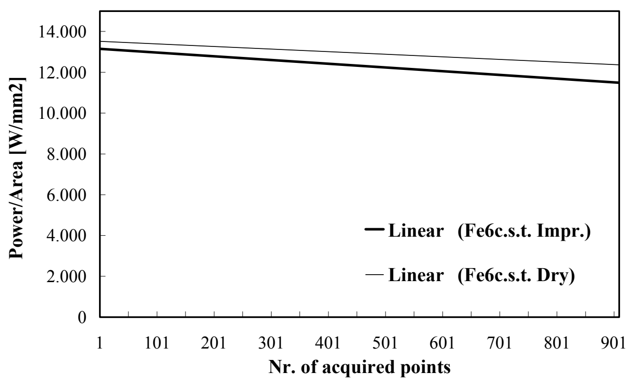

(b)

Figure 8 Linear fit of diagrams 5 (a) and 7 (b).

The conclusions that follow emerge from examination of all the experimental data recorded (cutting forces, power and tool wear) that for the sake of brevity are omitted here.
Cutting forces and power were always found to be lower for the impregnated compacts than for the non-impregnated ones and exhibited a less irregular trend. For nominal, practically negligible tool wear, in some parts and notwithstanding the correction made, machine power was found to be higher for the impregnated than for the non-impregnated material. One possible explanation for this is that the impregnating substance does not exert any lubricating effect whatsoever, on the contrary additional work is expended for deforming this incompressible liquid.
Note that the extent of tool wear was found to decrease in particular for the sintered iron-copper alloy powder compacts, suggesting that modest pore deformation may be attributed to the copper-induced matrix hardening, thus depriving the impregnating agent of one of its functions, the copper acting as a lubricant in its place.

4 CONCLUSION

Pre-impregnation of sintered powder compacts significantly improves their tribological behaviour during machining, resulting in particular in a reduction of tool wear and work energy.
Impregnating porous materials prior to machining generally results in a decrease of cutting force and power and an increase in tool life. The substance should be applied preferably using a simple and rapid procedure with the workpiece already mounted on the mandrel. No significant differences have been observed for the different methods of impregnation tested and impregnating the cutting zone with the workpiece already in place offers an obvious advantage in that it wastes little time prior to machining and the procedure can easily be automated.
The need to use high solution concentrations is associated with the fact once the solvent evaporates the solute will occupy part of the pore so the higher the concentration the larger the portion occupied.
The greater the porosity and hence the lower the density of the material to be machined, the more effective the alcoholic rosin solution used as cutting lubricant will be.
Non-impregnated materials of higher density exhibited superior machinability compared to the lower density products, whereas for impregnated compacts, the low density material proved easier to machine.

REFERENCES

[1] Robert J. Causton, Machinability of P/M Steels. *Int. Conf. on Powder Metallurgy and Particulate Materials*, Seattle, Washington, USA, 1995.
[2] Gallo A. et al., The cutting of PM materials. *Proc. ICIM '91*, Torino, pp. 114 -119, 1991.
[3] Gallo A. et al., The role of impregnation in the drilling of PM materials. *'95 AMT*, Zagopane (Poland), 1995.

[4] Autorino A. et al., Energy dissipation in machining holes in impregnated sintered iron. *III Conv. A.I.Te.M.*, Salerno; 1997.

[5] Mazillu D., Tirpe Gh., Dobre D., Considerations regarding energetic aspect at machinability of powder metallurgy materials. *2nd Int. Conf. On Materials And Manufacturing Technologies – MATEHN '98*, Cluj-Napoca, Romania, Sept. 10 - 13, 1998.

[6] Gallo A. et al., Comportamento di diverse miscele di polveri Fe-Cu durante il trattamento termico di sinterizzazione. *Atti 12° Conv. Naz. Tratt. Term., Salsomaggiore*, pp. 289-302, 1989.

[7] Gallo A., Dionoro G., Il ruolo di un impregnante nel taglio dei sinterizzati. *Atti I Conv. AITEM*, Ancona, pp. 29-36, 1993.

[8] Bocchini G. F., De Fiore J. E., Dionoro G., Gallo A., A wax solution as an affective impregnant for improving the machinability of PM materials. *XXVI Conv. Naz. AIM*, Milano, nov. 1996.

[9] Trent E. M., *Metal cutting*. Butterworths, London, 1984.

[10] Shaw M. C., *Metal Cutting Principles*. Clarendon Press, Oxford, 1986.

ISSN 1590-8844
International Journal of Mechanics and Control, Vol. 07, No. 01, 2006

LOAD DEPENDENT COULOMB FRICTION: A MATHEMATICAL AND COMPUTATIONAL MODEL FOR DYNAMIC SIMULATION IN MECHANICAL AND AERONAUTICAL FIELDS

Lorenzo Borello Matteo D. L. Dalla Vedova

Department of Aerospace Engineering, Politecnico di Torino
Corso Duca degli Abruzzi 24 – 10129 TORINO

ABSTRACT

The proper evaluation of the friction forces and torques acting in a typical mechanical transmission is usually necessary when an accurate simulation of its dynamic behaviour is requested. For example, the authors consider the flap actuation systems of most commercial and military aircraft consisting of a centrally located Power Drive Unit (PDU), a shaft system and a certain number of reversible or irreversible actuators assembled in several different configurations. Dynamic behaviour of the flap actuation system is strongly dependent from the actuator dynamics; so an appropriate actuator simulation model is necessary in order to evaluate the system behaviour with a high degree of accuracy, both in failure and in normal operating conditions. An elevated compactness of the simulation model is recommended, nevertheless the high computational accuracy requested.
Aims of the work are:

- the proposal of a general purpose dynamic model concerning any transmission gear, equipped or not with ends of travel (such as the flap control system actuators), characterised by an innovative dry friction physical model having a component proportional to the load acting on the driven element (efficiency < 1) and a component independent on the load;
- the development of the corresponding mathematical model and computational algorithm;
- the implementation of a Matlab-Simulink numerical model able to simulate the dynamic behaviour of a typical flap control system equipped with the above mentioned actuators;
- the simulation of some typical actuations, in order to validate the proper accuracy of the actuator dynamic model (by means of comparison with the results coming from a suitable and reliable FORTRAN numerical model, and the analysis of the results.

The algorithm developed by the authors in Matlab-Simulink supplies an effective answer to such problems and, by means of a self-contained Simulink subsystem, can describe the effects produced by friction forces on the dynamic behavior of a generic mechanical actuator and simulate many of typical coulomb friction's effects interacting with its mechanical ends of travel. The first author has previously developed the physical-mathematical model illustrated here, performing and optimizing the Fortran algorithm used for validation of simulation produced from the present computing method; the second author, on the base of this results, has instead developed the Matlab-Simulink algorithm devising a self-contained Simulink subsystem of absolutely general validity and easy employable in many various applications

Keywords: coulomb, friction, actuator

Contact author: Matteo D. L. Dalla Vedova

E-mail: matteo.dallavedova@polito.it

1 INTRODUCTION

The primary and secondary flight control actuation systems of most commercial and military aircraft consist of a certain number of actuators fed by two or more hydraulic lines; the actuation devices are normally linear and based upon jacks (usually adopted for spoilers, airbrakes, flaps, etc. and realized by means of irreversible ACME screws or reversible ballscrews) or rotary actuator (often based upon epicyclical gear). The behaviour of this kind of system and the role that coulomb viscous forces plays in their dynamics, equipped with reversible or irreversible actuators, is analyzed and evaluated by means of numerical models. The flap actuation systems of most aircraft consist of a centrally located Power Drive Unit (PDU), a shaft system and a certain number of actuators (normally two for each flap surface). Depending on the performance requirements and on the specified interface with the other aircraft systems and structure, several different configurations have been used in the design of such actuation systems. PDU's can be either hydromechanical or electromechanical and be either of a single or dual motor type. In the last case, the outputs of the two motors can be either torque summed or speed summed. The shaft system generally consists of torque tubes connecting the PDU output with the right and the left wing actuators; however, the flap actuation systems of small commercial aircrafts often use flexible drive shafts rotating at high speed in place of the low speed rigid shafts.

The actuators are normally linear and are based on ballscrews (usually of reversible type), though some flap actuators use an ACME screw (irreversible); some flap actuators are of a rotary type (usually reversible).

The system must be able to prevent asymmetries between the left and right wing flaps in case of a shaft failure (detected by a proper asymmetry monitoring system) and to hold the surfaces in the commanded position following the shutoff command given when no actuation is required.

If the actuators use an irreversible ACME screw, the abovementioned requirements are intrinsically accomplished; if the actuators are reversible (in order to obtain higher efficiency), a brake system is necessary:

- controlled wingtip brakes (one for each wing) located at the end of the transmission line, close to the position transducers, that become engaged and brake the system after a failure has been positively recognised;
- self-acting irreversibility brakes within each actuator, which self engage when the actuator output overruns the input shaft.

The relative merits of the three solutions (non-reversible actuators, reversible actuators with wingtip brakes or reversible actuators with irreversibility brakes) and which of the three is better is a long debated matter: the maximum asymmetry in failure conditions is greater with the wingtip brake solution, the solution with non-reversible actuators requires higher hydraulic power owing to its lower efficiency and the irreversibility brake solution, that overcomes the shortcomings of the two previous solutions, is more expensive. Therefore the most commonly used architecture employees the reversible actuators with wingtip brakes and centrally located PDU (of a dual motor type for operational reliability) because it is cheaper and more efficient, nevertheless the associated high asymmetries in case of failure. Whichever the actual configuration of the flap actuation system is, its dynamic behaviour is strongly dependent from the actuator dynamics; so an appropriate actuator simulation model is necessary in order to evaluate the system behaviour with a high degree of accuracy both in failure and in normal operating conditions. A high compactness of the simulation model is recommended, nevertheless the high computational accuracy requested.

2 AIMS OF THE WORK

Aims of the work are:

- the proposal of a general purpose dynamic model concerning any transmission gear equipped or not with ends of travel characterised by an innovative dry friction model having a component proportional to the load acting on the driven element (efficiency < 1) and a component independent on the load;
- the development of the corresponding mathematical model and computational algorithm;
- the implementation of a Matlab – Simulink numerical model able to simulate the dynamic behaviour of a typical flap control system equipped with the above mentioned actuators;
- the simulation of some typical actuations in order to validate the proper accuracy of the actuator dynamic model (by means of comparison with the results obtained by means of a suitable and reliable FORTRAN numerical model) and the analysis of the results.

3 PHYSICAL - MATHEMATICAL MODEL

The dry friction acting on a movable mechanical element consists of a force opposing the motion having a value variable as a function of the speed.

In the most of the applications, however the following model (Coulomb friction) can represent the relationship between the friction force and the speed:

- in standstill conditions the friction force can have any value lower or equal in module to the so said static friction value;
- otherwise, the force module has a constant value equal to the so said dynamic friction value.

The corresponding mathematical model must be able to describe the behaviour of a mechanical element subjected to the friction, dividing between the four possible conditions as follows:

- mechanical element initially stopped which must stay in a standstill condition;
- mechanical element initially stopped which must break away;
- mechanical element initially moving which must stay in movement;

- mechanical element initially moving which must stop.

This ability can be important in order to point out some undesired behaviours characterising the position servo-mechanisms as the powered flight controls. Like previously said, the nature of the phenomenon of the coulomb friction cannot completely be described from linear models (even though more favourable for the possible analytical solutions of the relative dynamic equations); therefore whichever attempt of modellization not too simplified needs the use of nonlinearities of such complexity to advise the employment of techniques of numerical solution based on the dynamic simulation in the dominion of the time. The techniques of numerical solution mainly employed (and generally proposed in literature) are based however on mathematical models that are affected by severe shortcomings. The proposed model overcomes the above-mentioned shortcomings and correctly simulates the behaviour of the mechanical device, as follows:

- selects the correct friction torque sign as a function of the actuation rate orientation;
- computes the friction torques according to the actual load value on the mechanical element;
- distinguishes between aiding and opposing load conditions;
- selects either the adhesion condition or the dynamic one;
- evaluates the eventual stop of the previously running mechanical element;
- keeps correctly in a standstill or moving condition the previously standstill or moving mechanical element respectively;
- evaluates the eventual break away of the previously standstill mechanical element;
- is able to simulate the dynamic of both reversible and irreversible actuators;
- simulate correctly the mechanical position limitation on the actuator of the landing flap.

The proposed model concerns the complete dynamics of the actuator-surface assembly, considered as a rigid mechanical element characterised by a single degree of freedom; the eventual actuator compliance and backlash are considered within the mathematical model of the transmission line.

3.1 DYNAMIC EQUILIBRIUM EQUATION

The equation of dynamic equilibrium is

$$Act - T_{FR} = J_S \ddot{\vartheta} \tag{1}$$

where

$$Act = T_{TR} - T_{LD} - C_S \dot{\vartheta}_S \tag{2}$$

represents the sum of the active torques, whose previous acquaintance is necessary to evaluate the friction torque.

3.2 FRICTION TORQUE EVALUATION

The Coulomb Friction models available in literature are usually characterized by extremely simplified structures and limited performances; their shortcomings, easily verifiable by means of opportune numerical simulations, are particularly emphasize if we adopt "integrated" dynamical models, that not only describe the performances of the actuator in Matlab – Simulink taking into account the frictions but estimating also the possible presence of mechanical ends of travel and their eventual interactions. The algorithm developed by the authors in Matlab – Simulink environment supplies an effective answer to such problems and, by means of a self-contained subsystem, can describe the effects produced by friction forces on the dynamic behavior of a generic mechanical actuator; authors' computational routine may correctly describe many of typical coulomb friction's effects as well as their interactions whit mechanical position limitation on actuator. The true potentialities of our algorithm for the calculation of the coulomb friction come from the implementation of a relatively simple but reliable and effective mathematical model in the greatly versatile of Matlab – Simulink environment; the result is a self-contained, general-purpose Matlab – Simulink subsystem that may be used directly in a lot of different applications (aeronautical, mechanical, etc). In our model, the friction torque is considered as the sum of a component not depending on the load and a further one related to the load through a defined value of efficiency. The former may assume two alternate values, static ($T_{FR0,stat}$) and dynamic ($T_{FR0,din}$). About the latter, in order to simulate both reversible and irreversible actuators, the proposed model introduces four suitable definitions of efficiency. Usually the efficiency is the ratio between the output and the input power (dynamic conditions) of a mechanical device; if it is characterised by a constant gear ratio (as the considered actuators are), the efficiency may be intended as the ratio between the output and the input torque (reported to the same shaft), even in static conditions. The efficiency of the actuator depends on the motion (static or dynamic) and load (aiding or opposing) conditions. Therefore, if the Coulomb friction model is employed, whatever actuator is characterised by the following four different types of efficiency:

$\eta_{din,opp}$= dynamic out/in torque ratio, opposing load

$\eta_{din,aid}$= dynamic out/in torque ratio, aiding load

$\eta_{stat,opp}$= static out/in torque ratio, load opposing the eventual motion

$\eta_{stat,aid}$ = static out/in torque ratio, load aiding the eventual motion

In the opposing conditions the output torque is essentially represented by the aerodynamic load and the input one by the transmission torque; vice versa in the aiding conditions (in aiding conditions the mobile surface is seen like motor element or input and the PDU like user element or output). By an adequate selection of the values of the above reported efficiencies, it is possible to simulate the behaviour of both reversible and irreversible actuators. Generally, the efficiencies of the irreversible actuators are lower than the reversible ones; particularly the aiding efficiencies of the irreversible arrangement must be intended as negative. The model computes the friction torque as the above-mentioned sum of a component not depending on the load and a further one related to the load through the efficiency as:

$$T_{FR} = T_{FR0} + \left(\frac{1}{\eta_{opp}} - 1 \right) \cdot T_{LD} \quad (3)$$

in opposing conditions (both static and dynamic)

$$T_{FR} = T_{FR0} + \left(1 - \eta_{aid}\right) \cdot T_{LD} \quad (4)$$

in aiding conditions (both static and dynamic).

When the actuation speed is not null and the load opposing, T_{FR} is obtained by the relationship (3) in which $\eta_{opp} = \eta_{din,opp}$ and $T_{FR0} = T_{FR0,din}$; when the load is aiding, T_{FR} is obtained by the relationship (4) in which $\eta_{aid} = \eta_{din,aid}$ and $T_{FR0} = T_{FR0,din}$; in both cases the sign of T_{FR} is assumed the same of the actuation speed, owing to its sign in equation (1). Else, when the actuation speed is null, T_{FR} is equal to *Act* if it lays within two limit values; when the load is positive, the lower value, negative, is obtained by the relationship (4) in which $\eta_{aid} = \eta_{stat,aid}$ and $T_{FR0} = T_{FR0,stat}$ and the upper one, positive, is obtained by the equation (3) in which $\eta_{opp} = \eta_{stat,opp}$ and $T_{FR0} = T_{FR0,stat}$. If the load is negative, the lower value, negative, is obtained by the relationship (3) in which $\eta_{opp} = \eta_{stat,opp}$ and $T_{FR0} = T_{FR0,stat}$ and the upper one, positive, is obtained by the relationship (4) in which $\eta_{aid} = \eta_{stat,aid}$ and $T_{FR0} = T_{FR0,stat}$.

3.3 DYNAMIC EQUATION INTEGRATION

By means of the equation (1) is possible to compute the acceleration of the actuator-surface assembly

$$\ddot{\vartheta} = (Act - T_{FR}) / J_S \quad (5)$$

Through two following numerical integrations is possible to obtain the angular rate and, subsequently, then the displacement of the actuator-surface assembly; if, within a generic integration step, a sign inversion of the angular rate occurs, the model determines the assembly stop as a possible consequence of the friction. The following integration step is able to evaluate either the eventual uninterrupted standstill condition or the break away, according to the actual value of the active torques related to the friction. Fig. 1 represents the above-mentioned model.

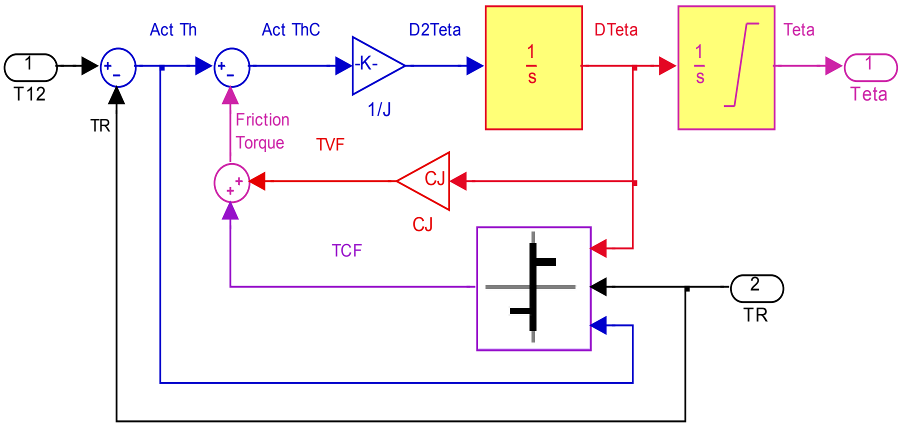

Figure 1 Theoretical actuator dynamics block diagram schematic.

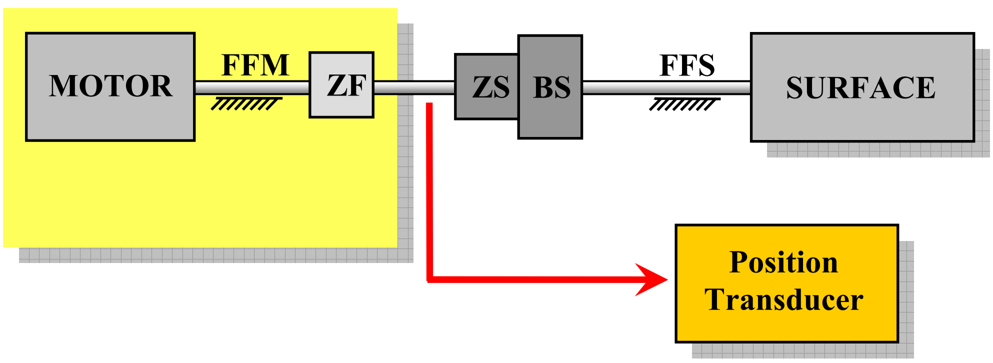

Figure 2 Passive subsystem schematic of control system dynamic model.

4 ACTUATION SYSTEM MODELLING

In order to validate the actuator dynamic model characterised by the load depending Coulomb friction, its behaviour is studied as a part of a hydraulic position servomechanism, typical of those currently used for flap control systems. Therefore, a control system dynamic model was prepared, whose passive subsystem is schematically represented in Fig. 2. The system model, which obviously represents only the essential elements of the real control flap system, consists of a Power Control and Drive Unit (PDU) that, through a drive shaft system and ballscrew actuators (BS), drives the flaps. Each actuator is an assembly containing a gear reducer (ZS) and a ballscrew. At the outer end of the shaft system is located the position transducers (PT) and the tachometers, if present. In order to put in evidence the eventual actuator reversibility, the considered system is never equipped with wingtip or irreversibility brakes. An Electronic Control Unit (ECU), not shown in Fig. 2, which closes the position control loop, performs the system control. The PDU contains the hydraulic motor, the gear reducer (ZM) and control valve; the system considered for this work was assumed to also contain tachometers for a continuous actuation speed control. Fig. 2 shows the mechanical model of the actuation system.
The model takes into account the hydraulic and mechanical characteristics of all system components, including their friction.
In particular, the model takes into account the following:
- Coulomb friction (FF) altogether generated in the PDU (FFM) and in the actuators (FFS),
- third order electromechanical dynamic model of the servovalve with limitations on the maximum excursion of flapper (XFM) and spool (XSM) and simplified fluid-dynamic model sensitive to the internal leakage (Clk) and the differential supply – return pressure (PSR),
- dynamic and fluid-dynamic hydraulic motor and high speed gear reducer model taking into account, beside the above mentioned Coulomb friction, viscous friction, internal leakage and mechanical ends of travel of the actuator and flap assembly.

5 SIMULATION RESULTS

The above-described model of the actuation system has been used to build a mathematical model of the whole system and a dedicated computer code written in Matlab – Simulink has been prepared.
In order to validate the computer code, some simulations have been run for the cases of irreversible and reversible actuator, with eventually reduced hydraulic system supply pressure and opposing or aiding loads; such simulations have been then compared with those obtained from an equivalent FORTRAN 90 model previously validated. In the following figures *Com* is the input command, *XF* the servovalve's first stage flapper position, *XS* the second stage spool position, *TR* the aerodynamic load acting on the surface, *DTeta* the surface angular rate and *Teta* the surface position. Figures 6, 7 and 8 show the simulations results for the cases of irreversible actuators. Fig. 3 represents the case of flaps deployment (0 deg to 17 deg) and retraction (17 deg to 0 deg) in loaded condition (35000 N*m, constant value).
As it is typical for the flap controls, the deployment travel is characterised by an opposing load, so having a reduced actuation speed (the commanded position is reached in approximately 6 seconds); in the retraction travel the aiding load produces a higher actuation speed (the commanded position is reached in approximately 2 seconds).
It must be noted that, owing to the actuator irreversibility, the aiding aerodynamic load produces a higher friction load, which results in a net small opposing load.
Fig. 4 represents the case of flaps deployment (0 deg to 17 deg) with opposing load (35000 N*m, constant value) and temporarily reduced supply pressure PSR.
At time = 1 s the supply pressure starts to drop at a rate of 12 MPa/s, reaching, two seconds later, the value of 2 MPa, kept constant up to time = 4 s; as a consequence, the actuation rate drops till to a complete stop, without any back movement owing to the irreversibility of the actuators. At time = 4 s the supply pressure starts to grow at a rate of 24 MPa/s, restoring, one second later, the design value of 26 MPa; thus, the actuation system starts again, reaching the commanded position approximately at time = 10 s.
Fig. 5 represents the case of flaps retraction (35 deg to 0 deg) with aiding load (35000 Nm, constant value) and temporarily reduced supply pressure with the same time history of the previous case; the pressure drop causes the actuation rate drops till to a complete stop, without any forward movement owing to the irreversibility of the actuators; the following pressure growth causes the actuation system starts again, reaching the commanded position approximately at time = 6.5 s. Figures 6, 7 and 8 show the simulations results for the cases of reversible actuators.
Fig. 6 represents the case of flaps deployment (0 deg to 17 deg) and retraction (17 deg to 0 deg) in loaded condition (35000 Nm, constant value) as in the previous case of Fig 3. The same considerations can be done, except for the reduced actuation times (deployment travel in approximately 3.5 s and retraction travel in approximately 1.6 s) in consequence of the higher efficiencies of the reversible actuators. It must be noted that, owing to the actuator reversibility, the aiding aerodynamic load produces a lower friction load, which results in a net aiding load.
Fig. 7 represents the case of flaps deployment (0 deg to 17 deg) with opposing load (35000 Nm, constant value) and temporarily reduced supply pressure with the same time history of Fig. 4. The pressure drop causes the actuation rate drops till to a complete stop, followed by a back movement owing to the reversibility of the actuators; the following pressure growth causes the actuation system

starts forward again (after a temporary stop caused by the friction), reaching the commanded position approximately at time = 7.2 s. Fig. 8 represents the case of flaps retraction (17 deg to 0 deg) with aiding load (35000 Nm, constant value) and temporarily reduced supply pressure with the same time history of the previous case; the pressure drop causes the actuation rate drops till to a reduced value without any stop condition owing to the reversibility of the actuators; the following pressure growth causes the actuation system attempts to restore the previous rate, only limited by the achievement of the commanded position approximately at time = 4.4 s.

6 CONCLUSIONS

The simulations performed show the proper accuracy of the proposed algorithm taking into account the effects of the dry friction and of the ends of travel on the behaviour of the actuators. It must be noted the ability of the proposed model to describe correctly the dynamic/static behaviour of both reversible and irreversible types, employing the proper values of the respective efficiencies.
So, the algorithm developed by the authors supplies an effective answer to the necessity of accurate tools in evaluating the effects produced by friction forces or torques and ends of travel acting on a generic mechanical actuator by means of a self-contained Simulink computational routine.

LIST OF SYMBOLS

Act	sum of the active torques
Com	input command
C_S	viscous damping coefficient of the surface
PSR	differential supply-return pressure
T_{LD}	aerodynamic load acting on the surface
T_{FR}	friction torque
$T_{FR0,stat}$	static friction torque component no load depending
$T_{FR0,din}$	dynamic friction torque component no load depending
T_{TR}	torque acting on the transmission line
J_S	moment of inertia of the aerodynamic surface
X_F	servovalve first stage flapper position
X_S	servovalve second stage spool position
$\eta_{din,aid}$	out/in torque ratio, aiding load, dynamic conditions
$\eta_{din,opp}$	out/in torque ratio, opposing load, dynamic conditions
η_{opp}	out/in torque ratio, opposing load
η_{aid}	out/in torque ratio, aiding load
$\eta_{stat,aid}$	out/in torque ratio, aiding load, static conditions
$\eta_{stat,opp}$	out/in torque ratio, opposing load static conditions
Teta	surface position
DTeta	surface angular rate
D2Teta	surface angular acceleration

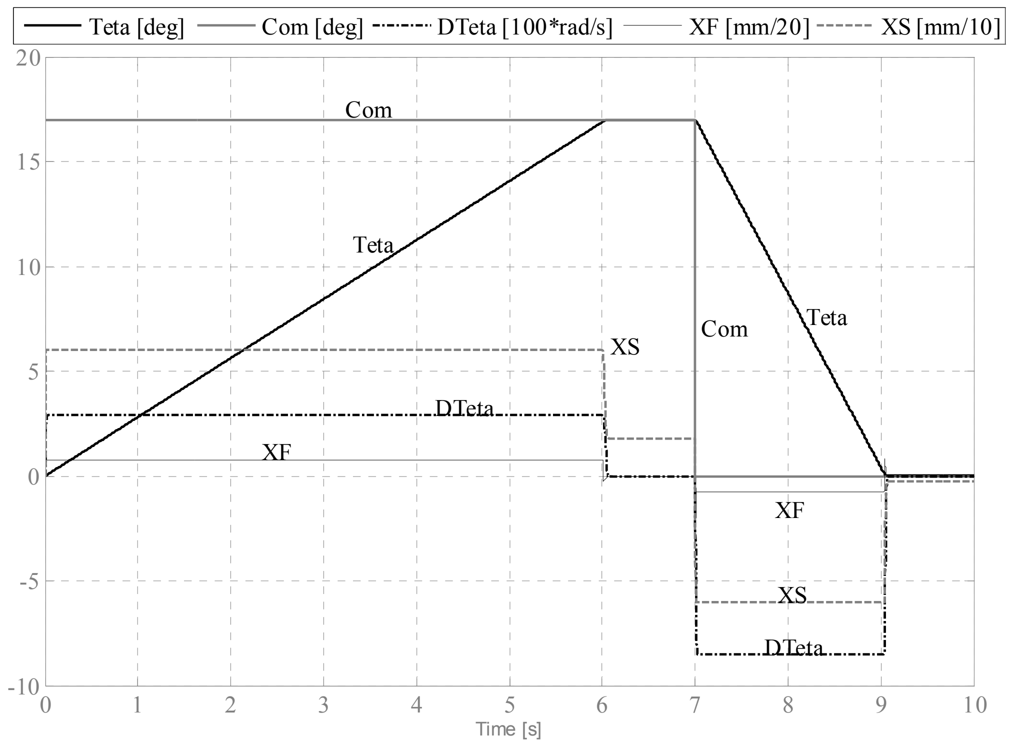

Figure 3

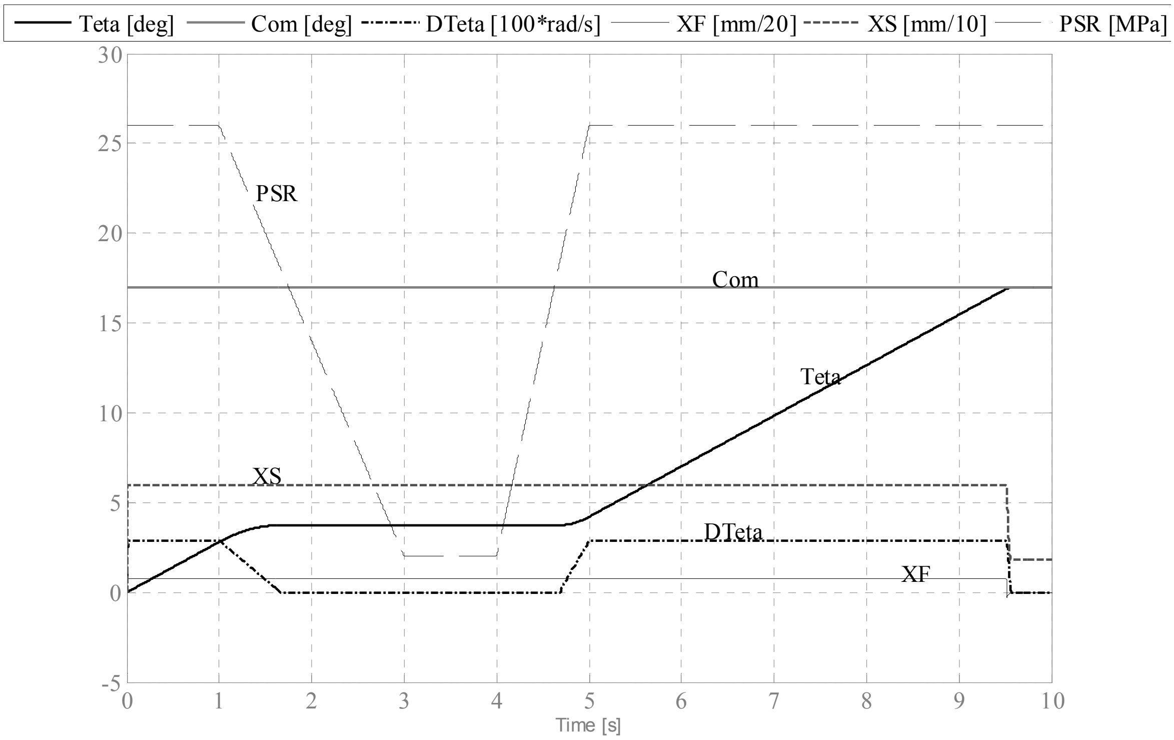

Figure 4

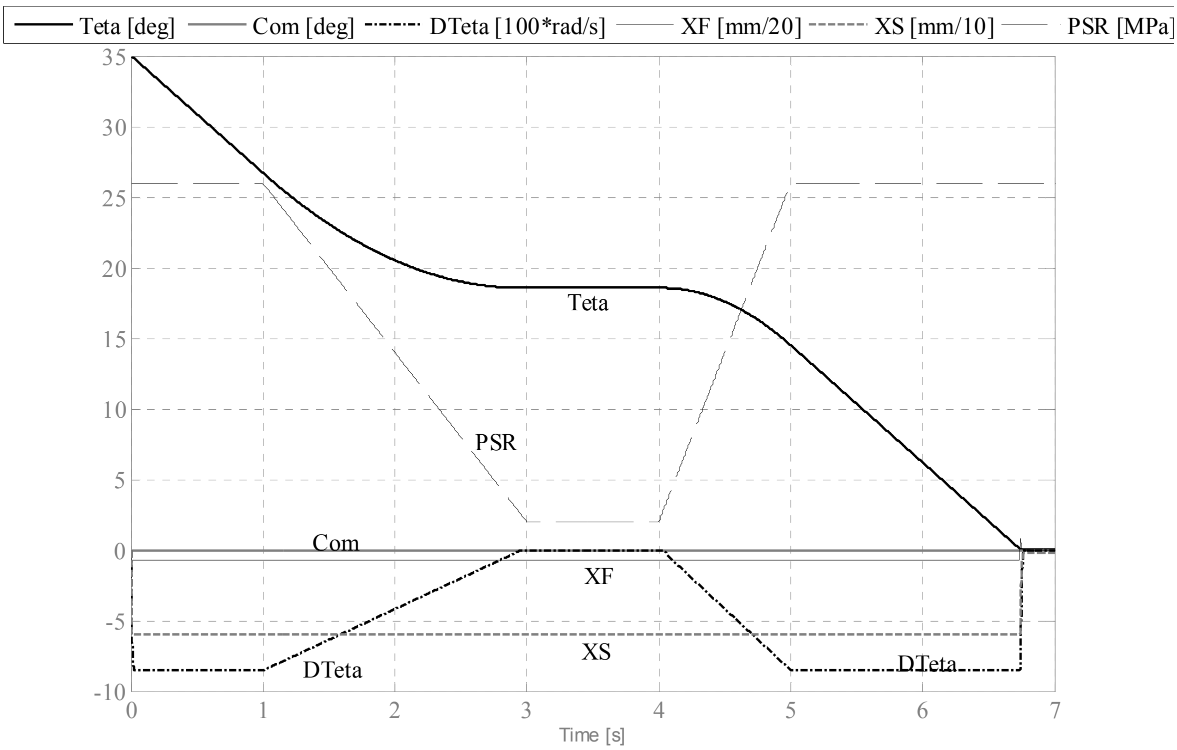

Figure 5

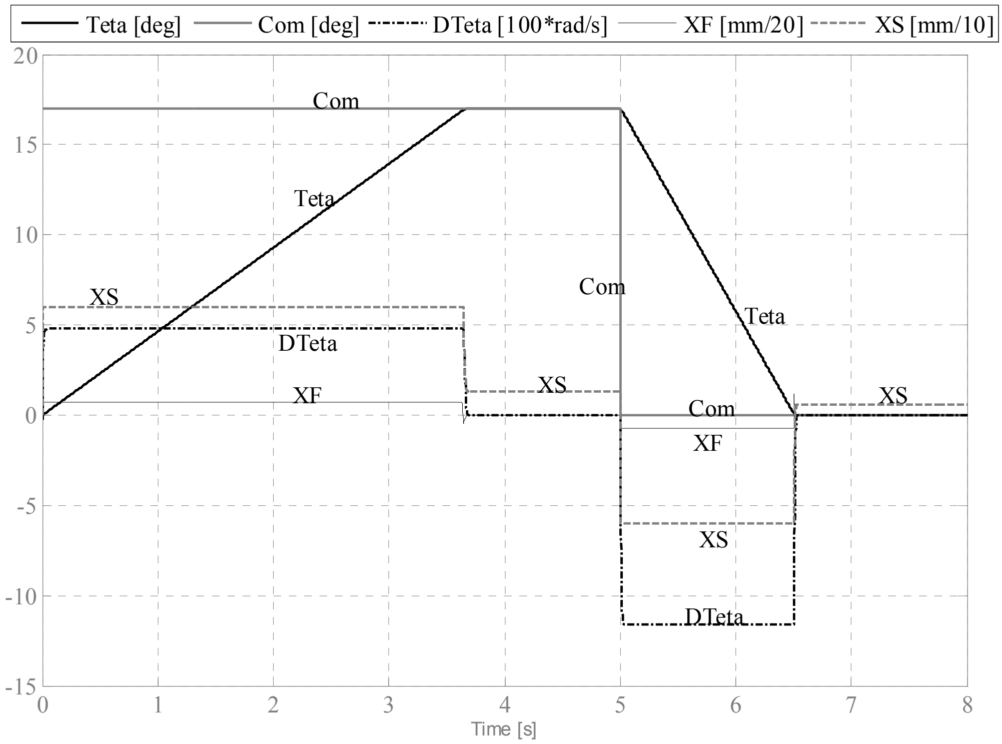

Figure 6

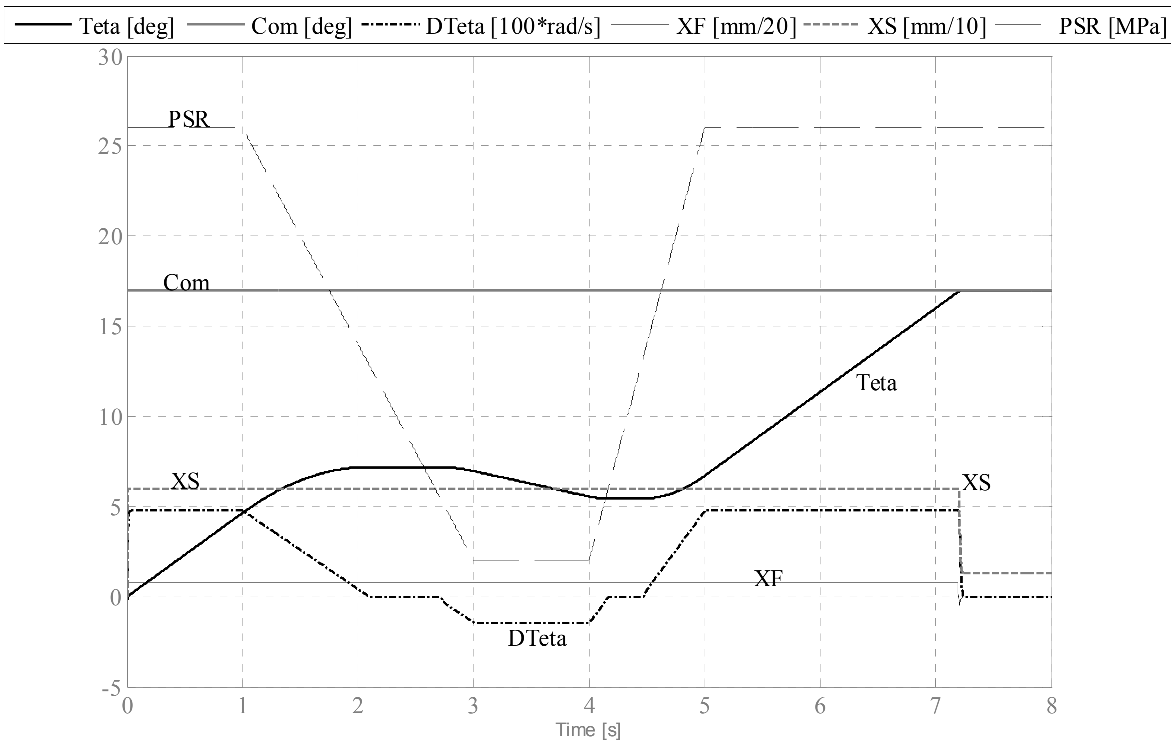

Figure 7

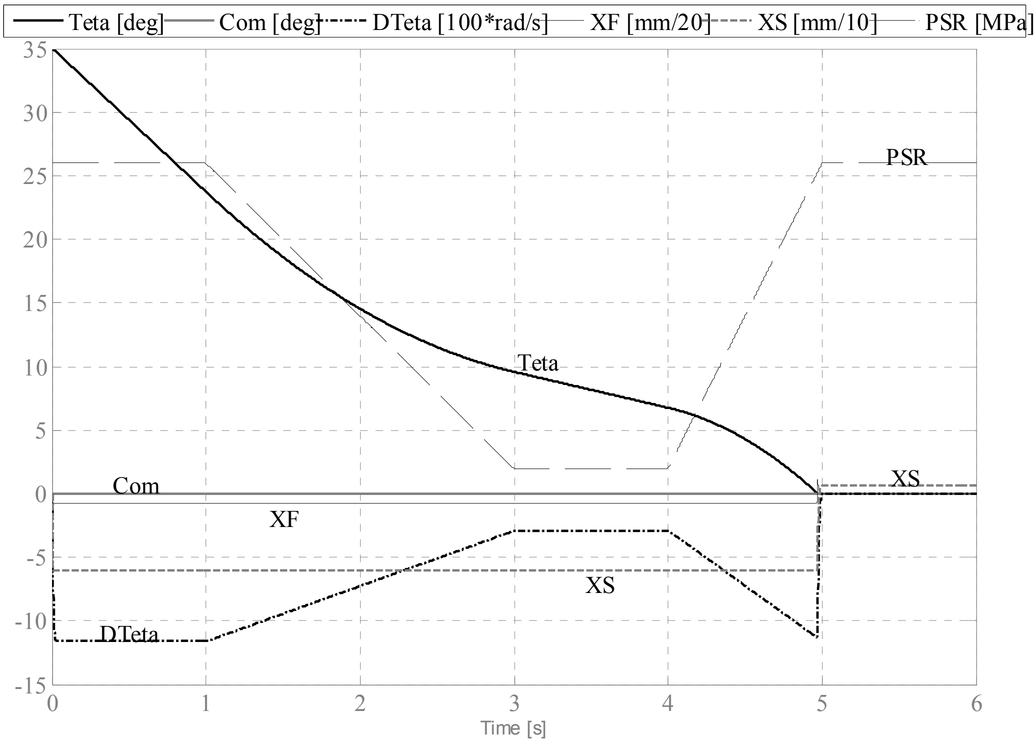

Figure 8

REFERENCES

[1] Jacazio G., Borello L., A non-linear model of an electrohydraulic servo system with axial piston hydraulic motor, *7th International Fluid Power Symposium*, Bath, England, 16-18 September 1986.

[2] Jacazio G., Borello L., Mathematical models of electrohydraulic servovalves for fly-by-wire flight control systems, *6th International Congress on Mathematical Modelling*, St. Louis, Missouri, U.S.A., August 1987.

[3] Borello L., Villero G., Modelli di attrito coulombiano nella simulazione di servomeccanismi, *NT Tecnica & Tecnologia N.3/89 (A.M.M.A.)*, Turin, Italy, pp. 11-17, May-June 1989.

[4] Jacazio G., Borello L., Villero G., Secondary flight controls: mechanical failures of transmission lines and related asymmetry problems, *19th ICAS Congress*, Anaheim, California, U.S.A., 18-23 September 1994.

[5] Borello L., Villero G., Flap control system actuators: mathematical and computational model for dynamic simulation, *European Congress on Computational Methods in Applied Sciences and Engineering ECCOMAS 2000*, Barcellona, Spain, 11-14 September 2000.

[6] Viersma T.J., *Analysis Synthesis and Design of Hydraulic Servo-systems and Pipelines*, Elsevier, Delft, 1980.

[7] Dransfield P., *Hydraulic Control Systems. Design and Analysis of their Dynamics*, Springer Verlag, Berlin, 1981.

[8] Karnopp D., Computer simulation of stick-slip friction in mechanical dynamic systems, *Journal of Dynamic Systems, Measurement, and Control*, Vol. 107, pp. 100-103, March 1985.

[9] Shearer J. L., Digital simulation of coulomb damped hydraulic servosystem, *Journal of Dynamic Systems, Measurement, and Control*, Vol. 105, pp. 215-221, December 1983.

[10] Kikuuwe R., Takesue N., Sano A., Mochiyama H., Fujimoto H., Fixed-step friction simulation: from classical coulomb model to modern continuous models, *International Conference on Intelligent Robots and Systems IEEE/RSJ 2005*, pp. 3910-3917, June 2005.

[11] Cull S. J., Tucker R. W., On the modelling of Coulomb friction, *Journal of Physics A: Math. Gen.,* Vol. 32, pp. 2103-2113, 1999.

ISSN 1590-8844
International Journal of Mechanics and Control, Vol. 07, No. 01, 2006

FEASIBILITY ANALYSIS ON A CAR CONTROL SYSTEM BY PSYCHIC-PHISICAL PARAMETERS

Alberto Rovetta Chiara Zocchi Alessandro Giusti
Alessandro Adami Francesco Scaramellini

Robotics Laboratory, Mechanical Department - Politecnico di Milano
Piazza Leonardo da Vinci, 32- 20133 Milano – Italy

ABSTRACT

This paper deals with the methodology of creating a new intelligent system to improve the driver's safety and comfort in automotive. The project aims at an architecture of intelligent sensors, able to monitorize the psychophysical state of the driver, in order to avoid accidents due to sleep attacks and assumption of alcool or drugs. Basically the parameters will be monitored by appropriate sensors which will turn the physical action into electronic signals. The signal power will be translated into a numerical value that measures some aspects of the performance of the driver in that particular condition. All the indications will be monitored in order to establish a protocol that will be on the basis for a safe drive and the psycho-physical condition of the driver may reveal if driver is reliable to a safe drive. Main goal of this research is to define the right parameters for driver's psycho-physical status monitoring inside the "Car System", by using the mechanical parameters of the car, the environmental conditions and the driver health and attention information, and to use them in a new architecture, where neural networks and fuzzy logic represent the tool to apply multivariate statistics.

Keywords: Safety in automotive, Sensors, Biorobotics

1 INTRODUCTION

Many projects in European Union programs are devoted to the increase of safety in automotive, in order to reduce deaths and accidents down to 50% in the next few years. PSYCAR project (Feasibility analysis on a car control system by psychic-physical parameters), funded by EU in a Regional plan, starting from Lombardy Italian Region and Austrian Region, is one of these projects and the methodology used as well as some preliminary results are reported.

From the Italian Statistic Institute (ISTAT) research, we know that most of the car accidents are due to an improper human behavior while driving, which cause more than 64% of car accidents and injuries and more than 60% of deaths. Car accidents are due, in most cases, to the following reason [1]:

- Alcohol: 72%;
- Sleep attack: 19%;
- Drugs: 9% .

Main purpose of the project is to define the correct psycho-physical parameters to be monitored in the driver + car system. Basically these parameters will be monitored by appropriate sensors which will turn the physical action into electronic signals. The signal power will be translated into a numerical value that measures some aspects of the performance of the driver in that particular condition. All the indications will be monitored in order to establish a protocol that will be on the basis for a safe driving. Main goal of this research is to define the right parameters for driver's psycho-physical status monitoring inside the "Car System", by using the mechanical parameters of the car, the environmental conditions and the driver health and attention information.

2 SECURITY IN AUTOMOTIVE

In this Section, the state of the art of security in automotive is presented and is about:

Contact author: Alberto Rovetta[1], Chiara Zocchi[2]

[1]E-mail: alberto.rovetta@polimi.it.
[2]E-mail: chiara.zocchi@polimi.it.

- existing devices for the evaluation of the driver's psychophysical state;
- security devices;
- articles related;
- avaible technology.

From this preliminary study, it can be observed that all the biggest automotive industry have product and commercialized systems more and more in the van (i. e. roadability and accidents prevention), but there isn't a multiple system, that analyzes and correlates different psychophysical parameters of the driver with those of the car, in order to monitorize the state of vigilance, attention and security.
Now some security devices are presented:

- Saab [2]. ComSense supports the driver concentration, because it's able to delay cell phones and messages, based on the drive situation. The function Night Panel (fig. 1) graduates the lights in the driver's cabin.

Figure 1 Saab: Night Panel.

- Citroen [3]. AFIL system: when the car is out lane, a vibration is applied in the driver's seat (fig. 2).

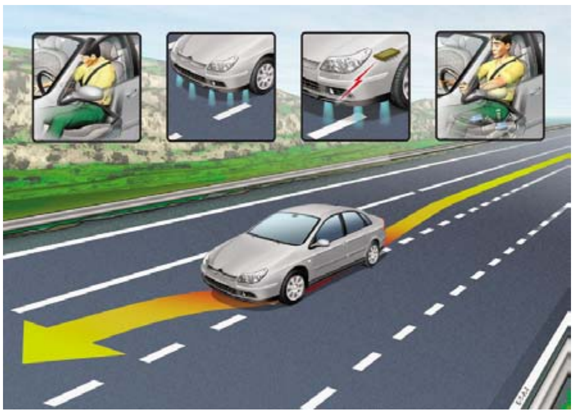

Figure 2 Citroen: AFIL system.

- Volvo [4]. DSTC: anti skid system (fig. 3) autonomously activated in winding and slippery roads, that reduces the motor power or brakes the wheels. IDIS (Intelligent Driver Information System) like the Saab ComSense.
- BMW [5]. Vigilance sensor (fig. 4): when the driver is seated and looks behind, an integrated with the car camera is focused upon the eyes. It follows automatically the head movements and records the eyes motions. This system detects the attention or stress level trough the blink frequency, velocity and amplitude, because a stressed person blinks are more frequently and slowly, till the eyes closure.

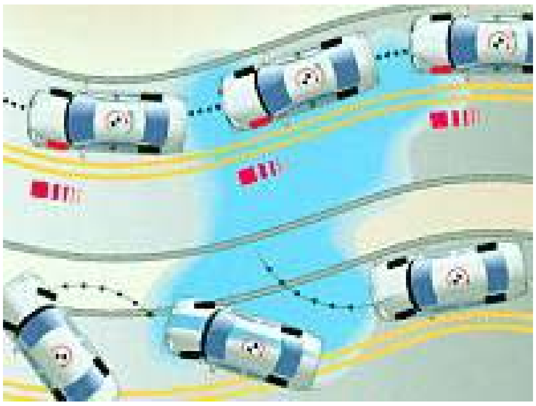

Figure 3 Volvo: DSTC system.

Figure 4 BMW: vigilance sensor.

- Audi [6]. Automatic seat adjustment, quality of the air analysis and roadability in different situations.
- Mercedes [7]. Night visual system (fig. 5A) with infrared and BAS Plus (fig. 5B) for anticipated braking in order to avoid accidents.
- Fiat [8], Alfa Romeo [9] and Peugeot [10]. Systems for roadability, internal comfort and parking.

3 DETECTION OF DRIVER PSYCHOPHISYCAL PARAMETERS

Rumar [11] compared the studies by Sabey & Staughton [12] and by Treat [13] as an illustrative accident investigation approach utilising multidisciplinary teams. As shown in fig. 6, road user/human factor has been pointed out as the dominating cause (over 90%) of road traffic accidents. As the main causes within human errors, recognition errors (perception, comprehension, delays and decision errors) are treated as predominated factors.
Significant efforts have already been made to detect the inattention of driver in terms of physiological and behavioural indicators [14]. The first ones include HRV

(heart rate variability), EEG (electroencephalogram, brain electrical activity), eye-based measure, and so forth. The others include driver steering wheel use, accelerator and brake applications, vehicle position (longitudinal, lateral and heading). As a summary, HRV is easy to monitor with sensors on the steering wheel, but it requires detailed spectral analysis and individual variations are large. In case of EEG, relationships between fatigue and drowsiness are established, but difficult to interpret and acquire with non wearable sensors. While most of physiological indicators have 'obtrusive' characteristic and require physical attachment to the driver (wearable sensors), behavioural indicators have 'remote' characteristic.

A

B

Figure 5 Mercedes: A) night visual system and B) BAS Plus.

A 'Steering wheel' indicator has advantage in easiness to monitor, but it is easily affected by vehicle/driving environment and has large individual variations. An 'Acceleration' or 'Brake pedal' indicator has also advantage in easiness to monitor, but it has not established relationship to attention. A 'Vehicle position' indicator has advantage of correlation with alcohol and drug use, but it is difficult to monitor. An 'Eye brink' indicator has advantage of remote measuring, but it has weak correlation with attention.

Combination of indicators (multiple indicators) has also been attempted to overcome the ambiguity and unreliability of single indicator as mentioned by Sussman et al. [14]. Also Faidy, Mevel, Siarry, Cointot & Coblentz argued that "multi-sensors approach, including 'dynamical sensors' for displaying driver's activity and 'static sensors' for characterising driver's attitude is more desirable" based on their literature review. The driver equipment developed [15] comprised of sensors including pressure, wheel angle, accelerator pedal angle and equipment for physiological data including EEG, electrooculogram (EOG), and electocardiogram (ECG). In their experiment for correlations between behavioural signals and the onset of driver's drowsiness at the wheel, "no linear relationship characterising each vigilance state was found between the car's sensor" and they suggested additional study to establish close relationships between alertness and motor behaviour.

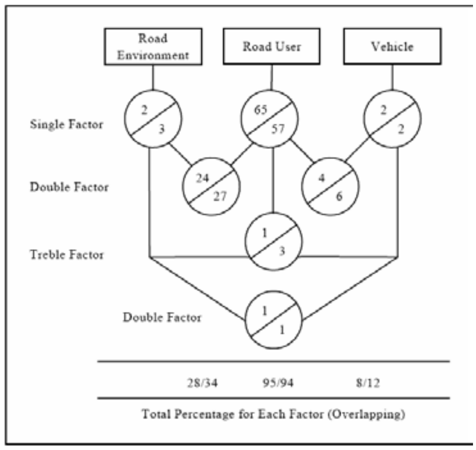

Figure 6 Percentage Contributions to Road Accidents.

O'Hanlon [16] studied the relationship between HRV and driver performance: drivers drove on round-the clock basis for 5 days over 586 km of the circuit. The results showed that "HRV increases markedly with driving time, and recovered after rest".

Verwey & Zaidel [17] carried out driving-simulator based experiment in which relation between driver's drowsiness and mental activity encouraged by game box was investigated. As measures for drowsiness, blinking and eye closure behaviour, self-ratings of driver on drowsiness were used. HRV (0.1 Hz component) was used to indicate mental effort as a physiological measure. As the result, the game box reduces the normal driving performance deterioration, typical for monotonous driving and the number of accident, incident, and crossing events. Besides it delays the onset of errors and improves the quality of vehicle control.

As stated by Alm [18] studied on whether visual sensitivity, defined as the ability to quickly detect and react to a visual stimulus, could be used to predict driver's ability to drive safety through experiment with simulator. A Yellow dot with the size 4x4 cm was presented and visual sensitivity was measured as the reaction time to the presentation of the yellow dot and as the number of "false alarms" and "misses". Results showed that about 50% of the variation in lateral position could be predicted using information of visual sensitivity. In the test protocol developed in the Robotics Laboratory, the driver executes some preliminary tests, similar to that proposed by Alm: a psychological questionnaire and a vigilance test (see Section 7).

As a recent study on ocular measure of driver alertness, Trucking Research Institute [19] did simulator-based experiments. Results showed that 'partial eye closure' was proved to detect cyclic phases of a driver experiencing brief

lapses of alertness and recovery, a continuous decline ultimately leading to an off-road simulator crash, an early warning potential of 10 minutes or more, and dramatic decline in the measure beginning 2-3 minutes before an offroad simulator crash.
Miller [20] suggested the model for "driver-adaptive warning system". In this system, onboard adaptive manoeuvre assessment module that analyses a driver's actions and develops a set of models for driver's characteristic behaviour in different driving manoeuvres, such as lane changing, lane following and traffic avoidance. These models provide the basis of two types of alarm system, state-based and event-based. Event-based system responds immediately to hazardous events while the other detects abnormalities in a given driver's current behaviour and responds by comparing predicted with actual behaviour to yield an error measure over time.
The model in fig.7 describes what action is to be expected from drivers in what situation: the system needs to know their expected actions in order to assist the drivers if they fail to act appropriately, so needs to recognise the situation driver, in order to evaluate whether a certain action is required of them.
Automobile accidents are one of the major causes of death in modern society and fatigue is also identified as one major risk factor [21–33]. This issue has not yet been studied, and this part of the project PSYCAR wants to investigate the occurrence of sleepiness in relation to the duration of sleep and driving as well as other psychophysical variables.

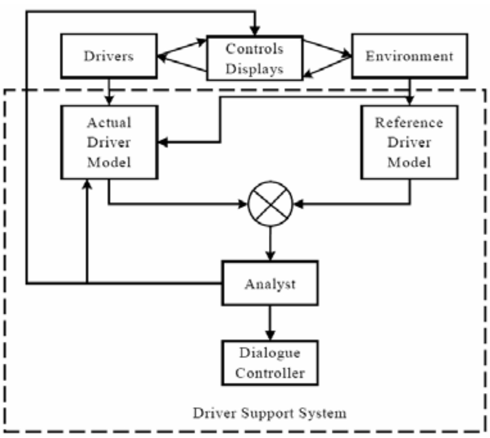

Figure 7 Driver support system.

4 ANALYSIS OF THE ALTERED PSYCHOPHISICAL STATE

4.1 ALCOHOL AND DRUGS

In general, all the euphoric agents increase the drive danger and support hazardous manoeuvres such as overtaking and increase of velocity. Besides the distortion of the perception faculty causes wrong evaluations about safety and braking distances.
The effects on the eyes, such as red aspect, inflammations and pupils dilatation, makes the driver to be more subject to dazzlement.
A lot of these substances cause somnolence and so increase the probability of sleep attack.
In table I the drugs and alcohol effects are reported.

Table I - Drugs and alcohol effects.

Agent	Effects
Cannabises	Tachycardia Blood pressure alteration Red eyes, mydriasis Increase of blink frequency
Ecstasy	Increase of body temperature
Amphetamine	Pressure Heart rate Increase of body temperature
Cocaine	Tachycardia Hypertension Tremor, contraction
Opiates	Respiratory frequency and volume
Methadone	Myosi Decrease of reaction time
LSD	Hallucinations
Alcohol	Decrease faculty of distance and velocity perception and reflexes No coordinated movements Increase of body heat Euphoria Tunnel vision

4.2 SLEEP ATTACKS

Sleep begins with yawns, eyes burn, closing eyelids and similar. It's due to normal fatigue, monotony, bad air, alcohol or drugs.
Sleep attack is a particular type of sleep: the driver has the eyes open, but he/she doesn't really sleep and isn't completely awake. So in this situation, the car is without driver, because he/she is in a non conscious state and is not able to elaborate information from the eyes. If the car is moving at 100km/h velocity, in a 1s sleep attack, 28m are traveled along the road without driver's reactions.
The most important sleep attack advises are:

- The car has greater oscillations around the middle of the lane;
- Involuntary reduction of car velocity;
- More frequent and slowly blinks;
- Yawns increase.

Apart from fatigue and monotony, other factors that induce sleep attacks are listed below:

- Oxygen lack in the driver cabin;
- High temperature of the driver cabin: the driver feels at ease and reduces concentration.

In the automotive market there are more or less sophisticated systems avoiding sleep attacks: the simplest measures the inclination of driver's head and signals unexpected falls ahead (fig. 8A). One of the more sophisticated is the BMW camera (presented in the Introduction fig. 8B).

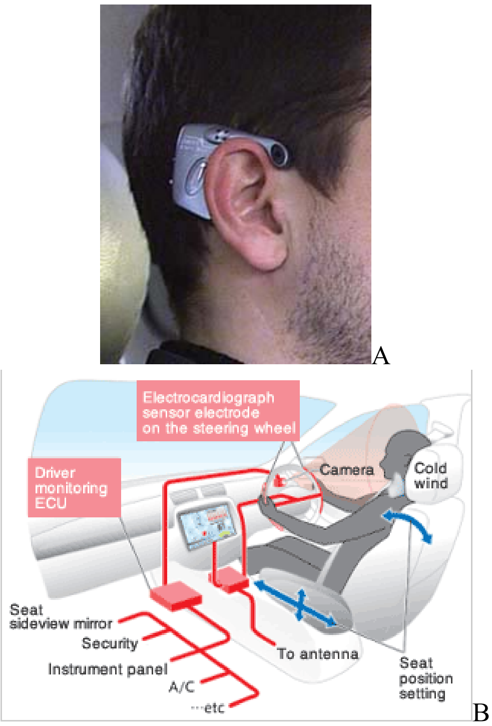

Figure 8 Security system evaluating A) head inclination and B) blinks frequency (BMW).

4.2.1 FROM CONSCIOUSNESS TO SLEEP

The electroencephalograph EEG measures 4 types of encephalic waves [35]:

- alpha: 8 - 12 Hz of frequency and 25 - 100 μV of amplitude;
- beta: with frequency more than 13 Hz and amplitude less than 40 μV;
- delta: 0.5 – 3.5 Hz of frequency and 75 - 200 μV of amplitude;
- theta: 4 - 7 Hz of frequency and 20 - 120 μV of amplitude. It appears spontaneously during the transition from vigilance to sleep.

Transition from consciousness to sleep [34] is gradual and these phases can be listed:

1. decrease of α waves amplitude;
2. α waves gradual disappearance in the occipital part, with a spatial distribution in the anterior part;
3. rapid eyes movements (REMs) reduction;
4. slow eyes movements (SEMs) appearance with 0.2 – 0.6 Hz of frequency;
5. θ waves appearance;
6. vertex EEG waves appearance.

5 PARAMETERS ANALYSIS AND CHOICE

After the studies presented in the previous Sections, 24 parameters have been chosen and they're collected in 3 groups:

1. physiologic parameters: blood pressure, heart rate variability (HRV), perspiration, tremor, pupils dilation, blink, pulmonary frequency and volume, head inclination, alcohol content, body temperature (THE), brain waves, reaction and action times and galvanic skin resistance (GSR);
2. driver's cabin parameters, related to the internal environment: temperature, humidity, smell, noises and oxygen/carbon dioxide concentration;
3. dynamics parameters, related to the car: velocity, acceleration, distances, time,.... Braking performance is critical in the avoidance of accident and almost every single accident involves the application of the vehicle brakes [36]. Except of the hazards due to unpredicted change in properties within one vehicle, differences between vehicles in braking performance are responsible of many rear end crashes [37]. Besides a vehicle with inferior brakes and tires must be driven a much longer distance behind superior vehicles on slippery winter roads. Technological approaches including ABS (Antilock Braking Systems) have been continuously designed to prevent the coefficient of road adhesion from dropping to slide values and raising the braking efficiency.

Considering these groups, a deeper study in the sleep attack field has been carried on in the Robotics Lab.. Up to now, for this purpose the parameters able to signal the sleep attack appearance are: body and peripheral temperatures (THE), GSR, HRV, blinks and brain waves (tab. 2).

Table II - Meaning of the psychophysical parameters: X = useful, - = less important [38].

	EEG	EOG	HR	HRV	EMG	THE	GSR
Stress	-	-	x	x	x	x	x
Negative emotions (e.g. anxiety, tension)	-	-	x	-	x	-	-
Mental fatigue/effort	x	x	-	x	x	x	x
Inattention	x	x	-	-	-	-	-
Sleepiness	x	x	-	x	-	x	x

At this point is right to remember that the project Regins-PSYCAR specifics require cheap and compatible solutions with technology ready to use (MEMS or not). So the final choice of the psychophysical parameters has taken in consideration also these factors:

- no wearable sensors;
- no invasiveness;
- no influence of the driver psycho physic state;
- technological availability;
- costs.

The brain waves are very useful in monitoring the transition from consciousness to vigilance, but the instrumentation is composed by a wearable cap (EEG) or needs a lot of space for the magnets (MEG). So the driver brain waves can't be monitored during the drive, due to a technological lack. But they're helpful during the tests executed with the simulation apparatus (presented in Section 7), as reference information.

In the biomedical field blinks are measured with the intrusive EMG and EOG, but in automotive, cameras are used.

6 PRELIMINARY TESTS ON THE ACQUISITION APPARATUS

At the Politecnico of Milan, Campus Bovisa, car tests have been executed in order to check the first acquisition apparatus: Visual Energy Tester (Elemaya [39]) for the measure of EEG, GSR, EMG, HRV, THE and Armband (Sensormedics s.r.l [40]).
The route followed (fig. 9) was repeated 6 times:

1. start with I gear;
2. II gear after 100m;
3. III gear after 100m;
4. II gear after 100m;
5. roundabout, II gear;
6. III gear after 100m;
7. braking after 100m;
8. replace in start position.

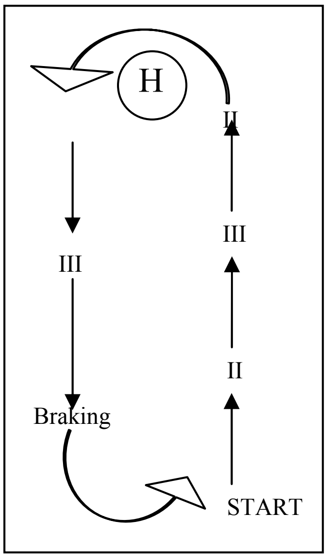

Figure 9 Route followed with the car and gear number inserted.

The test protocol is divided into these phases:

1. subject placement and test explanation:
   - erect trunk;
   - both hands on the steering wheel;
   - look ahead;
2. test start and acquisition
   - test A: EMG, cardiac frequency (fotopletismograph), GSR, body temperature;
   - test B (fig.10): frontal EEG with 2 electrodes, GSR, body temperature;
3. test conclusion and data storage
   - Excel tables with personal and acquired data.

From these preliminary tests, it was possible to observe that EEG waves were full of artefacts, due to car and driver movements, and tests duration (about 5 minutes) was too short, because sensors didn't reach their steady state correctly. The device ArmBand measures correctly GSR, body temperature and thermal exchange, but not in real time and so it can be only used as comparison with data acquired with sensors.

Figure 10 Subject executing test B.

7 SIMULATOR SYSTEM

A preliminary simulator system has been developed at the Robotics Lab.: it consists of a computer games' steering wheel (Logitech Momo) with pedals and a computer game that is projected in front of the driver, giving him the impression of actually driving (fig.11). The next step will be the application of a simulated path, realized by the group of the University of Linz (partner of Robotics Lab. in the PSYCAR project).
On the steering wheel, GSR (Galvanic Skin Response), HRV (Heart Rate Variability) and THE (peripheral body temperature) sensors are placed in order to measure the driver's parameters. In this way, the driver does not have to do anything special, that would not normally do when driving.
In addition to these sensors, six Electroencephalogram (EEG) signals are monitored: the EEG cap is necessary here but it will not be put on the actual system when it will go out from the laboratory.
The EEG signals are used in order to have an index of the driver's vigilance.

Figure 11 Simulator system

Also, using a two channel optical incremental encoder, the system can retrieve the steering wheel position and velocity.
Temperature and humidity sensors for the cabin are also placed in the simulation room as well as a temperature sensor for the environment outside the car system.
Apart from the driving simulation and sensorization system, two video cameras (Mustek DV 9000) have been placed in the simulation room, in order to monitor the driver's face, reactions and body position, as well as the errors he/she is making, when obstacles appear.
In order to collect all the sensory data, a preliminary board with the sensors has been created and a LABVIEW and MATLAB program (VI) have been made for this purpose.

7.1 TESTS PROTOCOL

The simulations are made on two different driver conditions: the normal and the altered states.
In the first case, the driver has slept during the night as usual, while in the second he has been awake for twenty-four hours.
The duration of the experiment is half an hour per person.
The simulations are always made in dark and noiseless conditions in order to have much more possibilities to fall asleep or to lose attention.
Before starting the data acquisition, the date, time and environmental conditions are noted and the car is always positioned at the same point. Each subject, before driving on the simulation for the first time is also trained to use the simulator and to always follow the same pre-defined route.
The subject has to be trained about what to do during the drive:

- initial body posture: left hand on the wheel, right sensorized hand on the leg (in order to reduce noises), left foot on the brake, right foot on the accelerator, look on the street.
- route and speed: the driver has to follow the right lane of the highway, to do U-turn at the end of the highway, always keeping 60km/h. The subject has to avoid accidents during the route.
- sudden events: he has also to be trained to brake answering to an obstacle appeared on the display.

7.2 PRELIMINARY AND REACTION TESTS

In order to create a comparison between normal and altered state the preliminary executions of a psychological test (questionnaire) [45,46] (fig. 12) is required.
During the vigilance test in pre-defined times that the subject doesn't know, the driver must brake. The response time is then stored with all the other sensory data.
This response time, data from the EEG signals and the number of errors the subject has made, will determine his safety index in no drive conditions.

7.3 DATA ANALYSIS

Each parameter will be defined by measurable digital values and will support to evaluate any possible alteration.

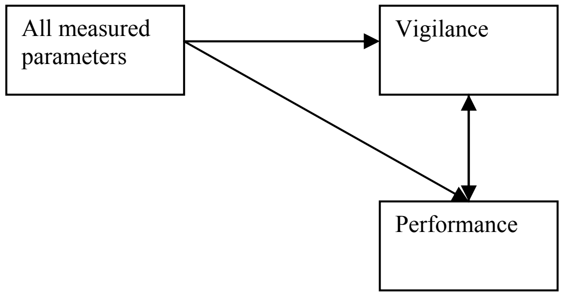

Figure 12 Relationship between the parameters measured, the vigilance and the driver performance.

All the links between the parameters will allow evaluating the exact level of driver alteration from the regular activity – and also the stress, the tiredness, the unsafe driving.
The purpose of the statistical multivariate analysis applied, is to find a relation between all the measured parameters and the driver's performance and vigilance decrease. The index of the driver's performance and security is measured by counting the errors making during the driving session. Furthermore, the driver's vigilance decrease is measured by studying the EEG signals as well as observing his facial characteristics and driving position on the video stream acquired. The stored data is statistically analyzed using the MATLAB program.
At the end of the analysis the correlations are available between the groups of parameters and their corresponding output safety index. Using these values as inputs and output respectively, a neural network can be trained for the application.
First results show that BTS and HRV decrease in altered subjects, while GSR increase.

8 WARNINGS

The end of this feasibility analysis on a car control system by psychophysical parameters requires a feedback on the driver, trough the security index definition and warnings. The first correlates the state of the driver, car and cabin, while the other is the answer of the total system control.
The aim of the PSYCAR project is not to wait that the driver fell asleep, but to advise him/her before, when the state of vigilance gradually decreases, in order to avoid accidents.
General human factor issues - timing of warning (when), warning modality (how) and warning contents (what) - are considered in this Section.

8.1 TIMING OF WARNING

Properly designed timing of warning is a critical element both in system effectiveness and user acceptance and the selection of a detection criterion must balance the need for early detection with the avoidance of false alarms [41]. In facts too-early warning makes drivers have a mistrust for the system due to the useless of warning while too-late warning has no effect on collision avoidance.

The timing of warning criterion can be selected between two strategies: in the first, the system determines whether a collision is likely to happen at current speeds and distances, within a certain time interval (i.e. in a car-following situation, the time-to-collision is the time taken for the two vehicles to collide if they maintain their present speed and headway). Under the other strategy, the system assumes that the vehicle preceding could brake at full braking power at any time.

8.2 WARNING MODALITY

As a manner of delivering warning message, several modalities can be considered, including visual, auditory, haptic, and so forth.
Main shortcoming of visual mode can be the increase of visual attention workload, and main advantage is that it provides precise information or absolute value. Auditory mode can be limited by the driver's hearing ability and surrounding noise, but this mode can orient the driver more likely to the forward vehicle or situation. The most important feature of haptic mode can be the reduction of warning time delay. In particular Llyod [42] suggested some criteria for the selection of DVI (Driver Vehicle Interface) warning modalities:

- Benefit all drivers;
- Not require specific directional orientation;
- Be compatible with driver response;
- Have viable integration with DAS (Driver Assistant System).

Labiale [43] showed that subject's workload is lowered when utilising an audible presentation of navigation information as opposed to a visual presentation. As for collision warning applications, where very short words or commands relative to navigation displays, audible mode may be useful compared to visual one.
Schumann et al. [44] examined the potential to modify the vehicle control dynamics by modifying the driver's control input. They found that drivers were more responsive to proprioceptive cues (such as steering wheel vibration or force feedback, e.g., resisting the driver's control input to change lanes) as compared to auditory warnings.

8.3 WARNING CONTENTS

Warning contents regarding potentially hazardous situation can be provided to driver at specific driving situation. In general the message is clearly stated that something is going wrong and the driver can be in a dangerous situation.

9 CONCLUSION

Applications of results to high class cars and to mass automotive may be quickly applied, because new technologies and new methodologies of research and application today easily offer the capability to cover with the maximum safety the drivers all over the world.
Besides the application and the data correlation from a set of multiple sensors is innovative in the automotive field.

ACKNOWLEDGEMENTS

Thanks to Dr. Giroldini, head of the ELEMAYA company, for providing the physiological sensors as well as the physiological signal amplification equipment and for helping with his years of experience in the field, Dr. Perissin for providing us equipment to monitor human physiological parameters. Thanks also to Prof. Pessa of the University of Pavia and to Prof. Baldissera of the Statale University of Milano for their help on choosing the psychological and vigilance test.
Finally, thanks to all the partners who are giving suggestions to the new design, as Centro Stile Alfa, Elasis, Brembo, Alcatel, Cefriel, Magneti Marelli, STM, and particularly Fondazione Politecnico which is starting to promote the planning of further researches, together with Regione Lombardia.

REFERENCES

[1] http://www.istat.it/salastampa/comunicati/non_calendario/20051013_00/novita_editoriale_incidenti_stradali_2004.pdf
[2] http://www.saab.com
[3] http://www.citroen.com/CWW/fr-FR
[4] http://www.volvo.com
[5] http://www.bmw.com
[6] http://www.audi.com
[7] http://www.mercedes-benz.it
[8] http://www.fiat.it
[9] http://www.alfaromeo.it
[10] http://www.peugeot.it
[11] Rumar, K. (1982), *The Human Factor in Road Safety*, Invited Paper at the 11th ARRBConference, University of Melbourne, pp. 23-27.
[12] Sabey, B. E. & Staughton, G. C. (1975), *Interacting Roles of Road Environment, Vehicle, and Road User in Accidents*
[13] Treat, J. R. (1980), *A Study of Precrash Factors Involved in Traffic Accidents*, In: Rumar, K. (1982), "The Human Factor in Road Safety", Invited Paper at THE 11th ARRB Conference, University of Melbourne, pp. 23-27.
[14] Sussman, E. D., Bishop, H., Madnick, B., and Walter, R. (1985), *Driver Inattention and Highway Safety*, Transportation Research Record 1047, Transportation Research Board, pp. 40-48.
[15] Faidy, J., Mevel, Y., Siarry, P., Cointot, B. & Coblentz (1992), *The Detection of Alertness Level Drop at the Wheel: Study of New Behavioural Parameters and Associated Sensors*, Paper No. C389/254, ImechE, pp. 33-37.
[16] O'Hanlon, J. F. (1972), *Heart Rate Variability: A New Index of Driver Alertness/Fatigue,* SAE 720141, pp. 1-7.
[17] Verwey, W. B. & Zaidel, D. M. (1997), *Preventing Drowsiness Accidents by An Alertness Maintenance*

Device, TNO-Report TM-97-C012, TNO Human Factors Research Institute, Netherlands.
[18] Alm, H. (2000), *Driver Fatigue and Accident – Can Visual Sensitivity Predict Drivers Ability to Drive Safely?* , Paper presented at the 14th Triennial Congress of the International Ergonomics Association and 44th Annual Meeting of the Human Factors and Ergonomic Society, San Diego, California, USA.
[19] Trucking Research Institute (1999), *Ocular Dynamics As Predicators of Alertness and Prophylactic Napping As a Fatigue Countermeasure*, FHWA-MC-99-028, Federal Highway Administration, U.S. Dot.
[20] Miller, C. (1999), *Guidelines for Constructing an ITS Driver-Adaptive Warning System*, Annual Progress Report July 98 - June 99, Transportation Research Board, National Research Council, pp. 10.
[21] Prokop O, Prokop L. Ermu *dung und Einschlafen am Steuer*. Zhl Verkehrsmed 1955, No. 1, pp. 19 – 30.
[22] Harris W. *Fatigue, circadian rhythm and truck accidents*. In: Mackie RR, editor. Vigilance. New York: Plenum, 1977, pp. 133 – 47.
[23] Langlois PH, Smolensky MH, Usi BP, Weir FW. *Temporal patterns of reported single-vehicle car and truck accidents in Texas, USA during 1980– 1983.* Chronobiol Int 1985, No. 2, pp. 131–46.
[24] Thyge Corfitsen *M. Fatigue in single car fatal accidents*. Forensic Sci 1986, No. 30, pp. 3– 9.
[25] Hamelin P. Lorry *Driver's time habits in work and their involvement in traffic accidents*. Ergonomics 1987, No. 30, pp. 1323– 33.
[26] Lavie P, Wollman M, Pollack I. *Frequency of sleep related traffic accidents and hour of the day*. Sleep Res 1987, 16:275.
[27] Lauber JK, Kayten PJ. *Sleepiness, circadian dysrhythmia, and fatigue in transportation system accidents*. Sleep 1988, No. 11, pp. 503– 12.
[28] NTSB. *Fatigue, alcohol, other drugs and medical factors in fatal-to-the driver heavy truck crashes*. National Transportation Safety Board. Safety Study 1990. Washington, DC, 1990; NTSB/SS 90/01.
[29] NTSB. *A review of flight crew-involved major accidents of USA Air Carriers, 1978 through 1990*. National Transportation Safety Board. Washington, DC, 1994; NTSB/SS 94/01.
[30] NTSB. *Factors that affect fatigue in heavy truck accidents.* National Transportation Safety Board.Washington, DC, 1995; NTSB/SS 95/01.
[31] Summala H. *Fatal accidents among car and truck drivers: effect of fatigue, age, alcohol consumption*. Hum Factors 1994; No. 36, pp. 315– 26.
[32] Horne JA, Reyner LA. *Sleep related vehicle accidents*. BMJ 1995, No. 4, pp. 565– 7.
[33] Philip P, Vervialle F, Le Breton P, Taillard J, Horne JA. *Fatigue, alcohol and traffic accidents in France*. BMJ 2001, No. 322, pp. 829– 30.
[34] Santamaria, J., and Chiappa, K. H. *The EEG of Drowsiness*. New York, Demos, 1987.
[35] Caton R. *The electric currents of the brain*. Brit Med J., 1875.
[36] Smith, M. (1998), *Why Can't In-Service Safety Checks Mirror New Vehicle Design Rules? Braking Performance – A Good Example!*, In VTI Conference Publication 9A part 9, pp. 3-17.
[37] Strandberg, L. (1998), *Winter Braking Tests with 66 Drivers, Different Tires and Disconnectable ABS*, Paper presented at International Workshop on Traffic Accident Reconstruction, Tokyo.
[38] http://www.sensation-eu.org (Advenced Sensor Development for Attention, Stress, Vigilance & Sleep/Wakefulness Monitoring)
[39] www.Elemaya.com
[40] www.sensormedics.com
[41] Hancock, P. A. & Parasuraman, R. (1996), *Driver-Centered Issues in Advanced Automation for Motor Vehicles*, pp. 337-364.
[42] Lloyd, M. M., Wilson, G. D., Nowak, C. J. & Bittner, A. C. Jr. (1999), *Brake Pulsing as Haptic Warning for an Intersection Collision Avoidance Countermeasure*, Transportation Research Record No. 1694, pp. 34-41.
[43] Labiale, G. (1990), *In-Car Road Information: Comparison of Auditory and Visual Presentation*, In: Wilson, T. (1994), "IVHS Countermeasures for Rear-End Collisions Task 1 Interim Report: Human Factors Studies", Report No DOT HS 808 566, U.S. Department of Transportation
[44] Schumann, J., Godthelp, H., Farber, B. & Wontorra, H. (1993), *Breaking up Open-Loop Steering Control Actions the Steering Wheel as an Active Control Device*, In: Hancock, P. A., Parasuraman, R. (1996), "Driver-Centred Issues in Advanced Automation for Motor Vehicles", pp. 337-364.
[45] A. Rovetta, A. Cucè , M. Bisogni, R. Pegoraro, "Innovative biorobotic system DDX for the analysis of neuro-motor conditions: methodology and results", ICAR 2001, International Conference on Advanced Robotics, Budapest, 22-26 August.
[46] A. Rovetta, *Protocols for clinical tests on Parkinson disease affected persons and comparison with healthy people with a quantitative method of a new system Daphne*, MMVR 2002, January 22-26, Newport, Usa.

ISSN 1590-8844
International Journal of Mechanics and Control, Vol. 07, No. 01, 2006

HIGH RESOLUTION SERVOMOTOR FOR SPACE APPLICATION

Mirco Zaccariotto * Mariolino De Cecco ** Stefano Debei *
Roberto Ricciu *** Giampaolo Calabrese ****

* CISAS "G. Colombo",

** Dept. of Mech. and Struct. Eng., University of Trento,

*** Dept. of Mech. Eng., University of Cagliari,

**** LIKA Electronics

ABSTRACT

In this paper a custom-built Servo-Motor for space application is presented and discussed. This device was designed for the OSIRIS instrument of the ESA Rosetta spacecraft, scheduled to fly on 2004. The necessity to limit both mass and dimension of the Servo-Motor suggested to design a custom-built system, made up of a "Limited Angle Torque" motor and a high resolution optical encoder. The high ratio between the resolution and the outer diameter of the motor and the particular compactness of the system make the developed Servo-Motor of great interest for its use in space missions and for future industrial production.

Keywords: servomotor encoder space mechanism

1 INTRODUCTION

This work is the consequence of the Osiris experiment. The principal investigator of the Osiris project is Dr. U. Keller of the Max-Planck Institute. For the Rosetta spacecraft of the ESA mission (ESA Mission cornerstone, launched on March 2004 from Kourou), CISAS G. Colombo was one of the partner of an international team among several research institutes; Lika Electronic, which is an Italian company that develop high reliability systems for automation ranging from encoders, lasers, controllers, collaborated with CISAS to the development of the servomotor They turn back the principal results gotten from the CISAS and Lika [6] of the activity of design and characterization of the Servo-Motor for the electro-mechanical shutters.

Contact authors: M. Zaccariotto[1], M. De Cecco[2], S. Debei[1], R. Ricciu[3], G. Calabrese[4]

[1] Via Venezia 15, 35131 Padova - Italy

[2] Via Mesiano 77, 38050 Trento - Italy

[3] Piazza d'Armi 1, 09123 Cagliari - Italy

[4] Via S. Lorenzo 25, 36010 Carrè (VI) - Italy

The imaging system OSIRIS, on board of the Rosetta spacecraft, is focused on the mapping of the Churyumov-Gerasimenko comet nucleus and of the coma structure evolution in order to monitor the related dynamics.

The OSIRIS imaging system consists of two CCD (2048 x 2048 pixels, with a pixel size of 13.5 μm) cameras: a Narrow Angle Camera (NAC) and a Wide Angle Camera (WAC) with identical CCD and electro-mechanical shutters. The shutter, placed in front of the detector, consists of two independent four-bar linkages, each driving a thin blade [17].

As a comet is composed of extremely bright and dark parts, high contrast near the limb is obtained by means of a 16 bit ADC converter and, thanks to the short exposure time (minimum value is 10 ms), with electromechanical shutter instead of electronic shutter, higher signal-to-noise ratio are obtained. Forasmuch as the imaging system can observe the comet surface as close as 2 km and the comet nucleus is rapidly rotating (period = 0.2 day), the requirement of exposure repeatability and uniformity of the two cameras' shutter becomes 0.2%. That implies an extremely constant velocity of the blades in front of the CCD: 1.3±0.0026 m/s.

Fulfilling the above requirements means "to monitor" what happens during the motion of the blades and therefore to have the possibility to control the feedback: this is done via

ISSN 1590-8844
International Journal of Mechanics and Control, Vol. 07, No. 01, 2006

a fit measurement systems of the wave current form of the motors that is the handle to guarantee a motion above the CCD with a constant speed (uniformity of exposure) [21,22,23,24]. That is why, adding an instrument able to measure with high resolution and accuracy the blades angular motion was mandatory: with this goal the encoders described in the present paper has been designed, developed and qualified.
This mechanical system is a measurement system whose performance has to be defined in order to go through the highly hostile spatial environment (e.g., in the carry- the launch phase- and in the space over the terrestrial orbit).
The sub-system, encoder + motor, mounted in the shutter mechanism, must be qualified for the Rosetta space mission.
The approach in the design of the measurement system has been oriented to find a solution to its safe carry, in order to preserve its metrology performances [16,26].
The measurement system was an encoder for angular position [1,2]. A servomotor is joined to this measurement system: the latter could not be a conventional system as, for the ESA, it has to accomplish to another factor related to the allocate resources: small mass and little volume and the extended temperature ranges due to the permanence in the space extra-terrestrial.
The analysis of the state of the art about these measurement systems is below reported.
Encoders for angular and linear position measurement have been widespread in several fields since long time. Despite its consolidated technology, the research in this field is very active [3,4,5].
The maximum resolution to diameter ratio achievable is 3600 x 4 ppr for the optical solution..
For this space applications, a consolidated technology and the resolution limit and efficiency (leading to accurate velocity estimation typical of optical solution) are necessary. It has been also necessary to minimise the required resources, i.e. mass, volume and power, without jeopardize the reliability of servomotor.
For space applications only few companies produce qualified encoders (about five in the world [7,8,9,10,11,12]) and to our knowledge none of them integrate the instrument on the same shaft of the motor, both for mechanical and integration problems.
Despite the technology on consider consolidate, for space application it has to be considered critical because of the adopted methodology, which foresees an abundant use of joined portions for gluing through types of junctions which have not given good results in the hostile spatial environment the shutter experiences during its life (such as vibration, thermal vacuum) and caused problems to the required positioning.
As a consequence the instrument, which must be qualified to vibration and thermal vacuum cycling, has to implement special solutions to be mechanically insensitive to vibrations, even if optical parts with the minimum use of glue are present, and to survive the extended temperature ranges. This choice has oriented the project towards the development of a highly integrated encoder + motor of optical nature starting from the heritage of commercial encoders designed by Lika Electronics for applications that require high-reliability.
The instrument described in this paper was the output of a high demanding application (deep space, long-term mission) constrained with severe mass, volume and power budget. The instrument is therefore a high resolution to diameter ratio encoder integrated on the same shaft of a high efficiency Limited Angle Torque (LAT) motor. This solution, very sensitive to the mechanical design and mountings, allows the minimisation of mass and volume. Fig. 1 shows the shutter developed.

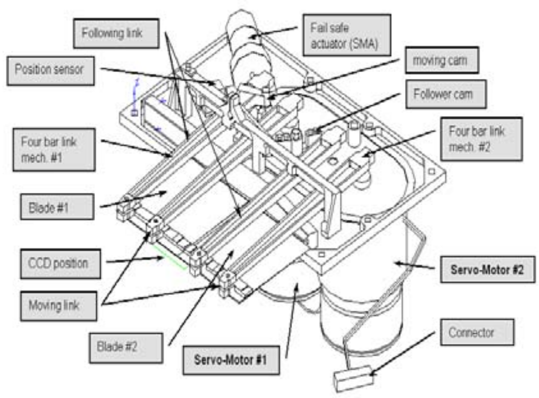

Figure 1 Shutter scheme.

2 TRANSDUCER DESCRIPTION AND PRINCIPLE OF OPERATION

The main mechanical, electrical and optical features of the mechanism are reported in table I.

Table I - Main features of the servomotor

Operative temperature range	-35 °C … +65 °C
Torque Sensitivity	21 N·cm/A
Peak Torque	14 N·cm
O.D. (outer diameter)	40.5 mm
Diameter	45 mm
Length	86 mm
Total mass	192 g
Resolution	3600 x 4 ppr
Encoder Power consumption	200 mW max.

The mounting of the motor and of the encoder on the same shaft the encoder principle of operation and the integration of a temperature sensor into the motor housing are of primary relevance.

ISSN 1590-8844
International Journal of Mechanics and Control, Vol. 07, No. 01, 2006

The motor and the encoder are mounted on the same shaft by means of a three ball bearings configuration (see figure 2) [13,21].
This solution allows the minimisation of the instrument volume and mass. A dedicate model has been developed in order to optimise the stiffness of the motor shaft and to verify the compatibility between blade trajectory, obtained from the encoder output elaborations, and the blade motion, in order to totally fulfil the performances requested for the shutter.

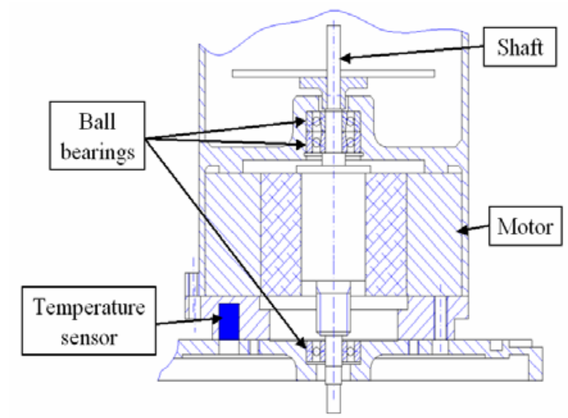

Figure 2 Motor configuration.

A first model is based on generalised impedance (2 degree of freedom DOF), that considers the four bar mechanism like a rigid body but take into account the torsional stiffness of the motor shaft, whilst in the second finite element model the elasticity of each component was taken into account.
In fig. 3 the module and phase plot for the transfer function between angular velocity output from encoder and angular velocity of the link (motor shaft attached to the moving link on the four bar mechanism) is reported [25].

The main torsional frequencies for the considered system are: 325 Hz, and 1365 Hz; these values are the results from the optimisation process that allowed to increase the band-pass of the encoder inside the allocate resources (mass, volume and power).
From Fig. 3 it is clear that the measurement chain under investigation undergoes an absorption in correspondence to the first cutting frequency (325 Hz) with consequent reduction of harmonic component in the measured signal. For harmonics between 325 Hz and 1365 Hz an amplification and a phase angle larger than 175° can be expected.
To reduce the uncertainty for the reconstruction of the blade velocities from encoders data it is important to select an appropriate current waveform, chosen by an algorithm developed on the inverse dynamics and kinematics of the mechanism.
These algorithms take into account the first cutting frequency and calculate a current waveform able to fulfil the requirement on blade motion (constant velocity path on the CCD) but with harmonic components lower than 300 Hz: to obtain these results a low pass filter with cutting frequency of 300 Hz and an iterative process has been used.
The principle of operation of the optical encoder is based upon four couples of led-phototransistor. This model of encoder configuration have an optical resolution as high as 3600 x 4 ppr. Two of them work in counter phase to give in output the channel A, the other two work in the same way to give the channel B (90° out of phase with respect to channel A). This way of reading the phototransistors output allows minimising the common mode uncertainties [14].
Opto-mechanically there are a moving coded disk and a fixed one (with the same angular resolution) in front of each couple led-phototransistor, whose distance is about 2 mm, with a mechanical accuracy of 0.01 mm adjusted by shimming during assembling phase. Due to the Moiré effect, the disk rotation causes different amount of light to

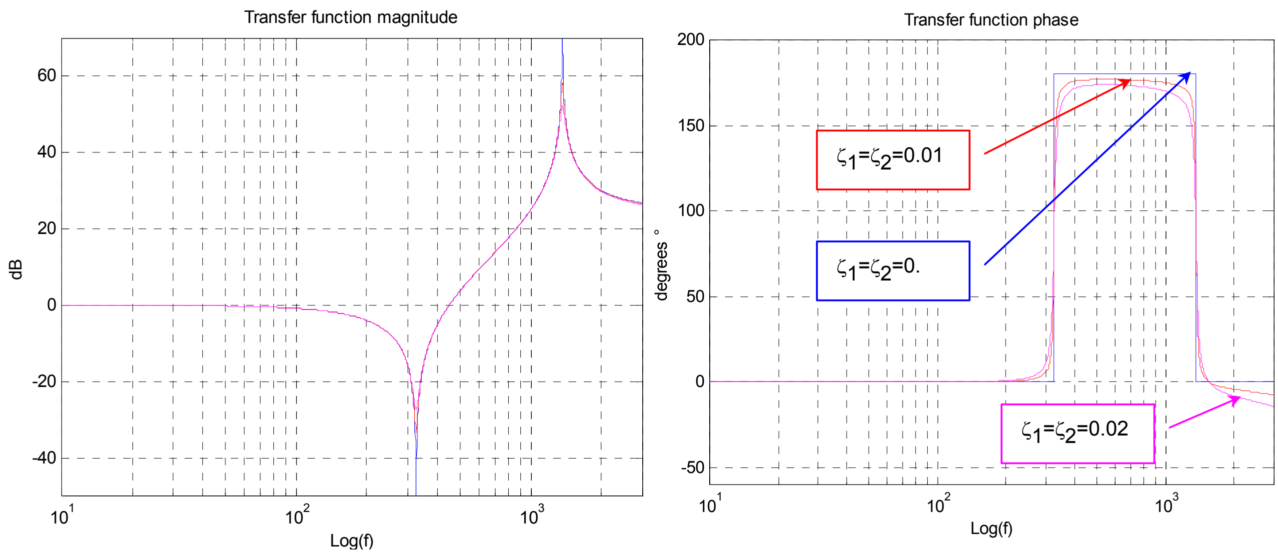

Figure 3 Module and phase plot for 2 D.O.F. system with small critical damping factors.

be directed toward the photo-sensors thus modulating their output. The needed differences in phase are achieved by the fixed disk.
As shown in figure 2 a temperature sensor (Analog Device temperature sensor AD590) is integrated in the instrument housing near the motor stator. In this way it is possible monitoring the instrument temperature for safety and/or for calibration purposes. For example the torque characteristics of the motor may be compensated for temperature variations.

3 INSTRUMENT QUALIFICATION

The reliability of a mechanism for space applications is of the great importance, especially when the mechanism is classified as a failing point to the mission. A strict test procedure was therefore necessary to qualify the custom-built servo-motor. Vibration and thermal-vacuum test method (with reference to the document: Rosetta Experiment Interface Document (EID-A), Issue 2 Date 01.06.1999) and results are presented in this section [19,20]. The following method can be roughly summarized as a sequences of vibrations and thermal vacuum. The tests are fit to simulate the environmental condition which the shutter will meet in his life and demonstrate the margin of the design. After each test the shutter was submitted to performances' checking, in order to verify its stability and reliability.

3.1 TEST METHOD

In order to check the design margin, the qualification test shall be more severe with respect to the acceptance test [15].

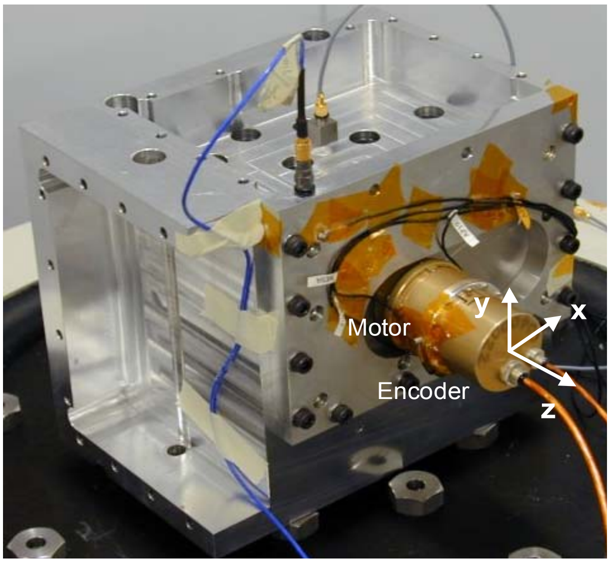

Figure 4 Vibration tests.

The main difference with the acceptance test is related to the levels of the vibration test and to the duration of the test itself. Fig. 4 shows both the servo-motor during the vibration tests and the vibration axes. In Table II, Table III, Table IV and Table V the sine and random qualification test levels are presented. Before and after qualifying the mechanism, a resonance test was performed in order to identify instrument natural frequencies and to detect possible frequency and amplitude changes after the qualifying tests. The test method used along every axis of the servo-motor is here summarized:

- the fixture calibration is performed,
- a resonance test is carried out,
- the qualification sine test is performed,
- a resonance test is carried out,
- the random qualification test is performed,
- a resonance test is carried out.

Thermal vacuum tests were also performed in order to verify the thermal reliability of the mechanism. Concerning these tests, a relevant difference of temperature was used for the acceptance and qualification tests. Table 6 shows these temperatures. Qualification was performed for 8 cycles of 2 hours of permanence, whilst acceptance require only 4 cycles. The servo-motor was able to have a safe mechanical behaviour during all the vibration and thermo-vacuum tests. Performance was almost unchanged during the tests as explained in the following section.

Table II - Shutter mechanism Sine acceptance level

	Frequency range [Hz]	Input level [g]	Sweep rate [Oct/min]
All axis	20-70	8.7	4
	70-85	Interpolation	
	85-100	1.3	

Table III - Resonance research levels

	Frequency range [Hz]	Input level [g]	Sweep rate [Oct/min]
All axis*	20-2000	0.2	2

Table IV - Shutter vibration test, main difference between qualification and acceptance vibration test

Test type	Qualification test Level module ratio respect the acceptance test level	Qualification test duration (min. or sweep rate)	Acceptance test duration (min. or sweep rate)
Sine	1.5	2 Oct/min	4 Oct/min
Random	2.25	2 min	1 min

Table V - Instrument random qualification levels

	Frequency range [Hz]	Input level [g^2/Hz]	Duration [min]
	20-100	+2 dB/Oct	
Z_u axis	100-200	0.38	
	200-2000	-8 dB/Oct	
	20-100	+10 dB/Oct	
Y_u axis	100-200	0.43	
	200-2000	-10 dB/Oct	2
	20-60	+15dB/Oct	
	60-100	0.24	
X_u axis	100-120	extrap.	
	120-180	0.85	
	180-200	extrap.	
	200	0.1	
	200-2000	-6 dB/Oct	

Table VI - Environmental testing temperatures

I38S Incremental Encoder	I/F T Range
Non Operational Qualification Range [°C]	-55 / +75
Operational Qualification Range [°C]	-35 / +65
Non Operational Acceptance Range [°C]	-45 / +65
Operational Acceptance Range [°C]	-25 / +55

3.2 MEASURED QUANTITIES AND ACCEPTANCE CRITERIA

In order to foreseen the behaviour of the servo-motor after the launch and the cruise phase of the space mission, the performance of the servo-motor before and after the qualifying tests were compared.
The following three quantities were chosen to show the correct functionality of the mechanism:

1. the duty cycle of each channel;
2. the phase between the two channel;
3. the zero pulse length.

These three measured quantities and the acceptance criteria are defined and explained here below.
Fig. 5 shows the digital output of channel A, B and Zero.

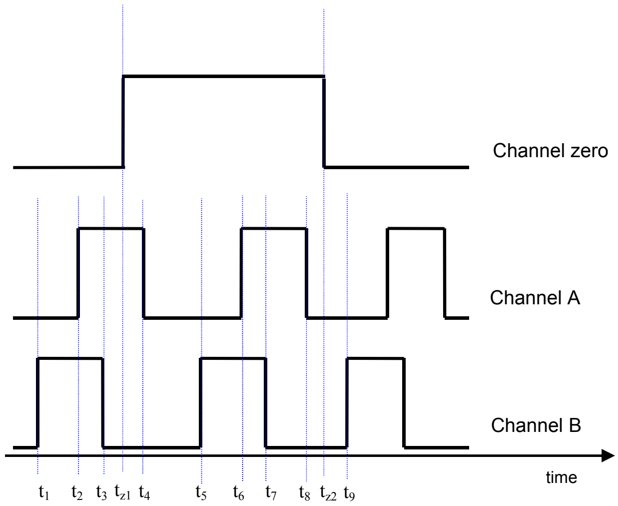

Figure 5 Scheme of the channel output as a function of time.

The duty cycle of channel A is defined as:

$$duty_A = 100 \cdot (t_4 - t_2)/(t_6 - t_2)\% \tag{1}$$

assigned to the time $(t_6-t_2)/2$.

Similarly, the duty cycle of channel B is defined as:

$$duty_B = 100 \cdot (t_3 - t_1)/(t_5 - t_1)\% \tag{2}$$

assigned to the time $(t_5-t_1)/2$.
The phase between channels is defined as:

$$Phase = 360 * (t_2 - t_1)/(t_5 - t_1) \tag{3}$$

The last quantity used for verify the integrity of the servo-motor after the qualifying tests is the zero length. The zero length (ZL) is defined as the ratio between the zero pulse length and the period of the channel B corresponding to the time instant of the zero. The procedure that was used is here summarized. First of all, the zero pulse length (ΔT_{ZERO}) and its time instant T_{ZERO} are computed as:

$$\Delta T_{ZERO} = t_{z2} - t_{z1} \geq \Delta T_{ZERO} = (t_{z1} - t_{z2})/2 \tag{4}$$

The channel B periods, just before and just after the time instant ΔT_{ZERO}, are then computed:

$$\Delta TCHB_{before} = t_5 - t_1 \text{ -> } TCHB_{before} = (t_5 - t_1)/2 \tag{5}$$

$$\Delta TCHB_{after} = t_9 - t_5 \text{ -> } TCHB_{after} = (t_9 - t_5)/2 \tag{6}$$

The period of the channel B corresponding to ΔT_{ZERO} is computed as:

$$\Delta TCHB = (\Delta T_{ZERO} - TCHB_{before}) \cdot (\Delta T\,CHB_{after} - \Delta TCHB_{before}) / (T\,CHB_{after} - TCHB_{before}) + \Delta TCHB_{before} \tag{7}$$

Lastly, the ratio between the zero pulse length and the period of the channel B is computed:

$$ZL = \Delta T_{ZERO} / \Delta TCHB \tag{8}$$

4 INSTRUMENT CALIBRATION

The encoder calibration had an important role in the servo-motor performance identification. The test-bed was made of a high resolution reference encoder with a resolution larger than one order of magnitude, a DC motor, a flexible shaft connector and the encoder to be calibrated. Fig. 6 shows the test-bed setup.

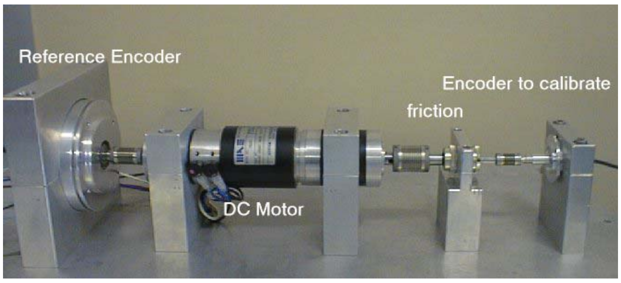

Figure 6 Calibration setup.

The quantity used to calibrate the encoder was the angular velocity. To compute this quantity, different techniques can be employed, which can be divided in time and frequency measurement to estimate velocity. Time measurement between the edges of the encoder pulses leads to a velocity data rate equal to the position data rate, the frequency one instead leads to a data rate much lower (or to a filtering which is equivalent). However frequency measurement is preferable when the encoder pulse frequency is high with respect to the clock available for time estimation. Due to the high motor dynamics, in this paper the instrument calibration making use of time measurement techniques is considered.
The signals of the led-phototransistor, represented by the channels A and B, follow these equations:

$$A(\theta)=A_0\cdot\sin\left(\frac{2\pi}{\theta_R}\cdot\theta+\varphi_A\right)+off_A \qquad (9)$$

$$B(\theta)=B_0\cdot\cos\left(\frac{2\pi}{\theta_R}\cdot\theta+\varphi_B\right)+off_B \qquad (10)$$

where $A(\theta)$ and $B(\theta)$ are the channel laws, A_0 and B_0 are two constants, θ_{Ris} a constant, θ is the angular variable, φ_A and φ_B are the phases, off_A and off_B are the offsets. The harmonic model was chosen for its simplicity and for the high tolerance of the mechanical device. Higher harmonic orders would have been necessary in case of low mounting precision.
The analogue signals are squared with a comparator referred theoretically to zero. The phases φ_A and φ_B , the offsets off_A and off_B, the amplitudes A_0 and B_0 should only in principle be equal for both channels but in reality this is not the real case. Figure 7 shows the ideal and real cases.
In order to achieve the highest accuracy in velocity estimation, the time was measured between the corresponding edges of the same channel (see Fig. 7). The angular velocity was therefore computed as:

$$v\left(\frac{t_i+t_{i+4}}{2}\right)=\frac{\Delta\theta}{t_{i+4}-t_i}\ . \qquad (11)$$

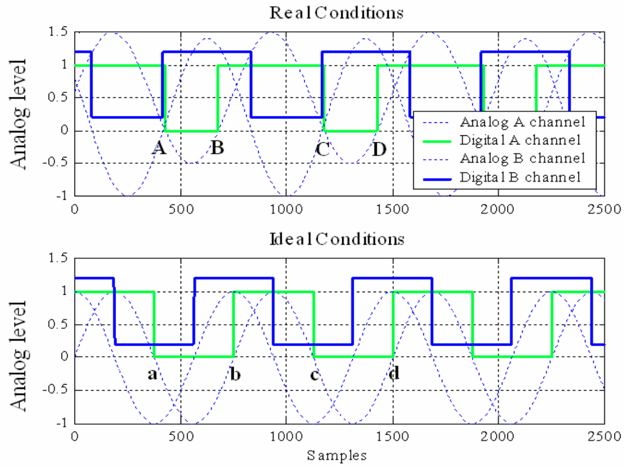

Figure 7 Real and ideal condition of channels output.

The same operation was accomplished for both channels and the resulting data were elaborated together. Since the data rate is non constant, an interpolation operation was carried out.
The figure 8 shows the results obtained during the calibration test.

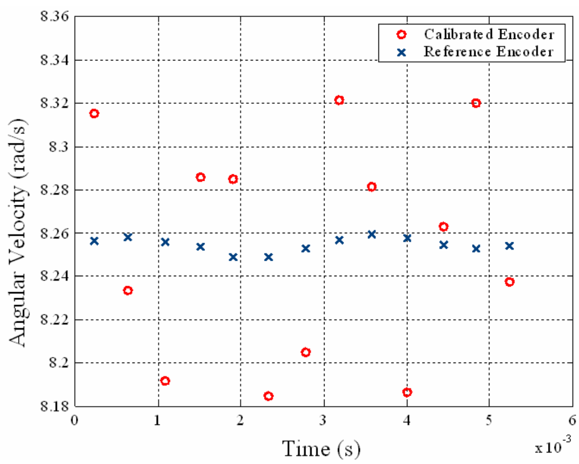

Figure 8 Angular velocity measured by the reference encoder and the encoder to be tested.

The velocity of the reference encoder was computed over a major number of periods in comparison to the encoder to calibrate. Therefore, the velocity accuracy of the reference encoder was better than the one of the encoder to be calibrated. The standard deviation between the velocities of the two encoders is 0.0512 rad/s.

4.1 PRINCIPAL RESULTS

In compliance with the § 3, the encoder performances have been checked.

The encoders have been submit to strictly withstand the vibration and thermal vacuum cycles (i.e. to the qualification tests).

In the following the sequence for the encoder performance characterization is listed:

- the measurement system calibration is performed;
- five cycles of the vibration tests on the measurement system;
- the measurement system is checked and the differences with the previous measurements are verified;
- the thermal-vacuum test is carried out;
- the measurement system is checked and the differences with the previous measurements are verified;
- the measurement system verification in calibrating table (test-bed) is performed.

The performed tests have been processed in compliance with the zone 3 in Fig. 9 through the four outputs, two for channel, named A and B (see description § 3 [18]).

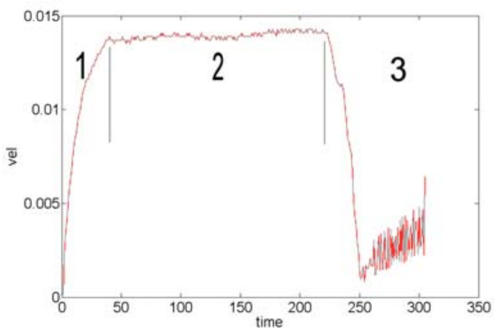

Figure 9 Progress speed.

The digital data from the couple of the encoder phototransistors have been sampled at 500 KHz; these data give us the possibility to deduce the evolution of the speed of the servo-motor shaft.

The raw data have been saved on a mass memory device in files text format containing three columns of values indicating the voltage values (high and low) in volts of the channel A and B. The third channel (zero) is the reference (low voltage).

Through specific custom software with an automatic system the following estimated data have been read and worked out:

- duty cycle for the two channel, A and B;
- the phase between the two channels;
- progress speed of the servo-motor in the test phase.

During the test the servomotor passes in sequence through three phases:

1. initial transient (settling time) or increase of speed;
2. steady-state or constant speed;
3. final transient or decrease of speed;

The Fig. 9 showing a example the evolution of the test in the three phases.

In the central part of the draw (phase 2 of the Fig. 9), the visual (geometrical) linearity is 10% lower than the mean value and the steady-state is obtained from the linear regression line as in Fig.10.

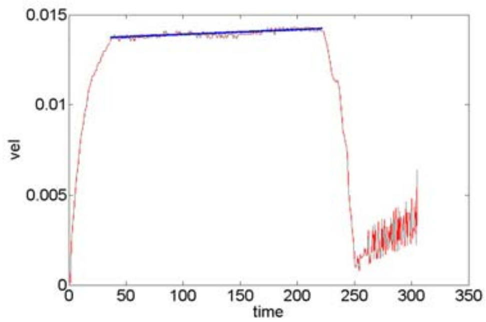

Figure 10 Steady-state of the velocity.

The initial transient is defined following these steps: three consecutive points are taken, the distance between the first and the last point is computed, the ratio between this distance and the mean value is calculated; when this ratio is lower than 0.05, that point is assumed to be the end of the initial transient and so the first point of the regime velocity (settling time). A similar method is used to find the begin of the final transient. The frame zone in steady-state is therefore identified as the one included between the above defined points. Within this zone the first order curve that best fits the data in a least square sense can be defined and it is shown in figure 11, together with two parallel lines (equal to the best fit line ± 5%) showing that the ratio is always included within that value.

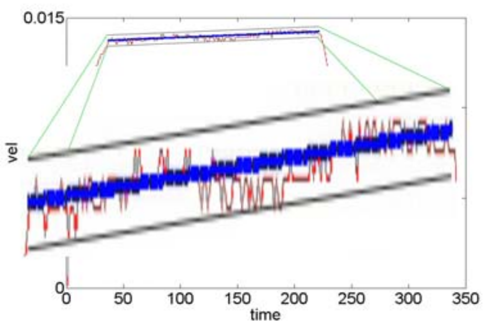

Figure 11 Least square fitted line (thick line blue) and variation of the 5% (thin lines).

The servomotors have been qualified in according with the parameters in the § 3.2:

a) variation of the duty cycle. This parameter, in the phase steady-state is nearly constant but it can change because of the effect the ambient stress due to the test that the device has been subject to, therefore the

variation on the mean value, max and min of the duty cycle of each channel have been verified;
b) variation of the phase between the two channels. The same method of the point "a".

The next elaborations of the data with some codes written on purpose. In Fig.12 an example of the trend of the mean, max and min value of the test.
The Fig.12 shows the variation of the temporal series of the value.

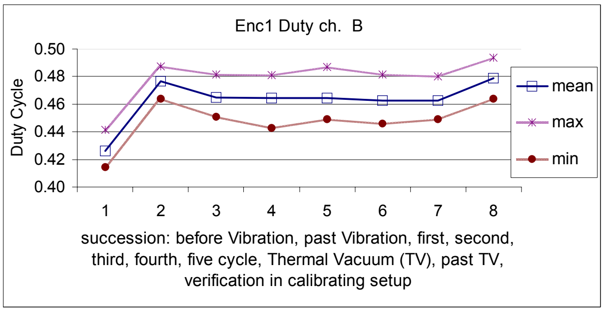

Figure 12 example of performed, trend of the value mean, max and min.

The cited codes have allowed the statistical analysis of the data via a comparison, point by point, between the least square fitted line (best fit line) and the measured data, so allowing to compute, along all the test, the per cent variation of the "point of the measure" from the least square fitted line.
The results of the tests is shown in Tab.7. In the same Tab. 7 the parameters of reference in § 3.2 have been inserted.

Table VII - Numerical results

Enc.	Type of the data	Max per cent variation respect least square fitted line [%]	Max per cent variation respect of the data of project [%]	Max per cent variation of the acceptance criteria of the project [%]
1	Channel A	2	9	40
	Channel B	2	9	40
	Phase displacement	11	19	33
2	Channel A	8	13	40
	Channel B	3	5	40
	Phase displacement	16	19	33

For the duty cycle: nominal value: 50%; max variation permitted: from 30 to 70%.
The max duty cycle observed is 37% with a mean value of 45% for this couple of phototransistors.
For the phase between the two channels: nominal value: 90° max variation permitted: from 60 to 120°.
In this case the data obtained from the analytical elaboration have given a max value of 71°. From the same test with the couple of phototransistors a mean value of 83° is obtained.
The max and min variation of the mean value for the couples of phototransistors are 44% and 51% for the duty cycle and 83, 85% for the phase between the two channels.
The authors comply with the required performances and they are above the nominal value.
The values of the max variation percent from the least square fitted line working on the mean data (T. amb) and the variation max percent with reference to the data project (T. amb.) as in the Tab.7, are taken.
The max variation from the least square fitted line is amply under the admitted variation percent.
The results are in good agreement with the data project.

5 CONCLUSIONS

An electro-mechanical shutter, consisting in two independent four-bar linkages, has been designed, realised and tested; this mechanical system is actuated by two custom designed servomotors.
A high ratio resolution over outer diameter of the motor (3600 x 4 ppr/40.5 mm =355.6 ppr/4) has been reached; the optical encoder principle of operation is based upon four couples of led-phototransistor.
Mass and volume have been minimized for aerospace higher efficiency mission: the mass reached is 192 g and the ∅45x86 mm are the overall dimensions.
A main goal of the research was keeping the high quality metrological characteristics in working conditions during the fly. The quality of metrological characteristics are saved despite of the hostile environment in the space and of the vibrations mainly in take off and thermal vacuum in the space.
The qualification tests here defined, more severe with respect to the acceptance tests, realised by a specific set-up and a specific measurement procedure, allowed to estimate the metrological characteristics as hereafter referred:
Duty-cycle: maximum deviation 13% and maximum allowable deviation 40% (already considered restrictive from the buyer because of the required technical characteristics regarding the physical characteristics, i.e. mass and volume)
Phase displacement: maximum deviation 19% and maximum allowable deviation 33%.
The obtained values of linearity in the third column of the table 7 are interesting too (Numerical results).

ACKNOWLEDGEMENTS

Work done in the frame of the OSIRIS/ROSETTA program partly supported by the Italian Space Agency (ASI) through a contract to CISAS/UPd. The OSIRIS imaging system (PI Dr. U. Keller) on board ROSETTA is managed by the Max-Planck Institute for Solar System Research (MPS) in Katlenburg-Lindau, thanks to an International collaboration among Germany, France, Italy, Spain and Sweden.

REFERENCES

[1] Orgen R., A high resolution optical shaft encoder, *Journal of the Institution of Electronics and Radio Engineers*, Vol.55, No.4, pp.133-138, April 1985.

[2] Engelhardt K., and Seitz P., High-resolution optical position encoder with large mounting tolerances, *Applied Optics,* Vol.36, No.13, 1 May, 1997.

[3] Kaye J.E., Balakrishnan S., Popplewell, N., and Menzies, R., High resolution adaptive tachometer for spindle motor drives, *Int. J. Electronics*, vol. 69, No.6, pp.835-848, 1990.

[4] Yeh W., High resolution optical shaft encoder for motor speed control based on an optical disk pick-up, *Review of scientific Instruments*, Vol. 69, No.8, August 1998.

[5] Engelhardt K., and Seitz P., Absolute, high-resolution optical position encoder, *Applied Optics*, Vol.35., No.1, Jan. 1996.

[6] http://www.lika.it/italiano/index.php)

[7] http://www.eltra.it.

[8] http://www.beiied.com/index.html.

[9] http://www.codechamp.fr/gb/index.ideal.

[10] http://www.heidenhain.com/.

[11] http://www.midoriamerica.com/.

[12] http://www.admotec.com/.

[13] Botta G.F., Balthazar J.M., Fisher B.R., Hermini, H.A., On Mechatronics systems management with fault tolerant architectures, *Proceeding of MYSME 2005 the International symposium on Multibody Systems and Mechatronics, Uberlandia* (Brazil), 6-9 March 2005.

[14] Auckland D.W., Sundram S., Shuttleworth R., and Posner D. I., The measurement of shaft torque using an optical encoder, *J. Phys. E: Sci. Instrum.*, Vol.17, 1984.

[15] Kang S., Cox D. and Tesar D., Design of actuator endurance and reliability testbed, *Proceeding of ASME IDETC/CIE: 26TH Biennal Mechanisms and Robotics Conference*, Baltimore, Maryland, 2000.

[16] Thomas N., The Influence of an Electronic Shutter on OSIRIS CCD Images, *Draft 1*, Nov. 1995.

[17] Sarafin T. P., Spacecraft Structures and Mechanism, *Kluwer Academic Publishers*, 1995.

[18] Doebelin E. O., Measurements System Application and Design, *McGRAW-HILL International Editions*, 1990.

[19] Polytec, Vibrometer Operator's Manual, *Series 3000, 2002.*

[20] Harris C. M., Shock and Vibration Handbook, *McGraw-Hill*, 1996.

[21] Da Peppo V., Naletto G., Analisi delle disuniformità introdotte dallo shutter, *TN 0015 UPD,1999.*

[22] Zaccariotto M., Realizzazione ed ottimizzazione di un otturatore veloce per misure fotometriche, *Tesi di dottorato Misure Meccaniche per l'ingegneria, XIII Ciclo*, Padova Anno accademico 1999-2000.

[23] Bulfone M.R., Modellazione numerica e verifiche sperimentali per il perfezionamento delle prestazioni di un otturatore fotografico per uso spaziale, *Tesi di Laurea in Ingegneria Meccanica of Padova*, A.A. 1999-2000.

[24] De Cecco M., Debei S., Fanti G., Pertile M., Zaccariotto M., Bianchini G., Angrilli F., Sistema di taratura per otturatori veloci da impiego spaziale, *atti del congresso 'Metrologia & Qualità'*, 20-22 Feb., Milano, 2001.

[25] Debei S., Angrilli F., Bianchini G., De Cecco M., Guizzo G., Parzianello G., Pertile M., Saggin B., Ramous P., Zaccariotto M., The Wide Angle Camera for OSIRIS Experiment of the ROSETTA Mission: design validation and qualification. *XVI congresso nazionale AIDAA*, 24-28 Sett 2001, Palermo, Italy.

[26] De Cecco M., Angrilli F., Da Forno R., Debei S., Uniformity error reduction by adaptive control of an electro-mechanical shutter for space imaging, *48th International Astronautical Congress,* 6-10 Ott., Torino, Italy, 1997.

ISSN 1590-8844
International Journal of Mechanics and Control, Vol. 07, No. 01, 2006

TEMPLATE FOR PREPARING PAPERS FOR PUBLISHING IN INTERNATIONAL JOURNAL OF MECHANICS AND CONTROL

Author1* Author2**

* affiliation Author1

** affiliation Author2

ABSTRACT

This is a brief guide to prepare papers in a better style for publishing in International Journal of Mechanics and Control (JoMaC). It gives details of the preferred style in a template format to ease paper presentation. The abstract must be able to indicate the principal authors' contribution to the argument containing the chosen method and the obtained results. (max 200 words)

Keywords: keywords list (max 5 words)

1 TITLE OF SECTION (E.G. INTRODUCTION)

This sample article is to show you how to prepare papers in a standard style for publishing in International Journal of Mechanics and Control.
It offers you a template for paper layout, and describes points you should notice before you submit your papers.

2 PREPARATION OF PAPERS

2.1 SUBMISSION OF PAPERS

The papers should be submitted in the form of an electronic document, either in Microsoft Word format (Word'97 version or earlier).
In addition to the electronic version a hardcopy of the complete paper including diagrams with annotations must be supplied. The final format of the papers will be A4 page size with a two column layout. The text will be Times New Roman font size 10.

Contact author: author1[1], author2[2]

[1]Address of author1.

[2]Address of author2 if different from author1's address.

2.2 DETAILS OF PAPER LAYOUT

2.2.1 Style of Writing

The language is English and with UK/European spelling. The papers should be written in the third person. Related work conducted elsewhere may be criticised but not the individuals conducting the work. The paper should be comprehensible both to specialists in the appropriate field and to those with a general understanding of the subject.
Company names or advertising, direct or indirect, is not permitted and product names will only be included at the discretion of the editor. Abbreviations should be spelt out in full the first time they appear and their abbreviated form included in brackets immediately after. Words used in a special context should appear in inverted single quotation mark the first time they appear. Papers are accepted also on the basis that they may be edited for style and language.

2.2.2 Paper length

Paper length is free, but should normally not exceed 10000 words and twenty illustrations.

2.2.3 Diagrams and figures

Figures and Tables will either be entered in one column or two columns and should be 80 mm or 160 mm wide respectively. A minimum line width of 1 point is required at actual size. Captions and annotations should be in 10 point with the first letter only capitalised *at actual size* (see Figure 1 and Table VII).

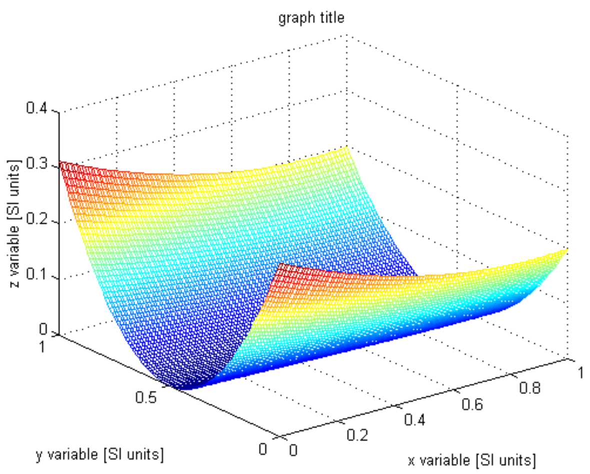

Figure 1 Simple chart.

Table VII - Experimental values

Robot Arm Velocity (rad/s)	Motor Torque (Nm)
0.123	10.123
1.456	20.234
2.789	30.345
3.012	40.456

2.2.4 Photographs and illustrations

Authors could wish to publish in full colour photographs and illustrations. Photographs and illustrations should be included in the electronic document and a copy of their original sent. Illustrations in full colour …

2.2.5 Equations

Each equation should occur on a new line with uniform spacing from adjacent text as indicated in this template. The equations, where they are referred to in the text, should be numbered sequentially and their identifier enclosed in parenthesis, right justified. The symbols, where referred to in the text, should be italicised.

- point 1
    - point 2
        - point 3

1. numbered point 1
    2. numbered point 2
        3. numbered point 3

$$W(d) = G(A_0, \sigma, d) = \frac{1}{T}\int_0^{+\infty} A_0 \cdot e^{-\frac{d^2}{2\sigma^2}} dt \qquad (1)$$

3 COPYRIGHT

Authors will be asked to sign a copyright transfer form prior to JoMaC publishing of their paper. Reproduction of any part of the publication is not allowed elsewhere without permission from JoMaC whose prior publication must be cited. The understanding is that they have been neither previously published nor submitted concurrently to any other publisher.

4 PEER REVIEW

Papers for publication in JoMaC will first undergo review by anonymous, impartial specialists in the appropriate field. Based on the comments of the referees the Editor will decide on acceptance, revision or rejection. The authors will be provided with copies of the reviewers' remarks to aid in revision and improvement where appropriate.

5 REFERENCES (DESCRIPTION)

The papers in the reference list must be cited in the text. In the text the citation should appear in square brackets [ ], as in, for example, "the red fox has been shown to jump the black cat [3] but not when...". In the Reference list the font should be Times New Roman with 10 point size. Author's first names should be terminated by a 'full stop'. The reference number should be enclosed in brackets.

The book titles should be in *italics*, followed by a 'full stop'. Proceedings or journal titles should be in *italics.* For instance:

REFERENCES (EXAMPLE)

[1] Smith J., Jones A.B. and Brown J., *The title of the book.* 1st edition, Publisher, 2001.

[2] Smith J., Jones A.B. and Brown J., The title of the paper. *Proc. of Conference Name*, where it took place, Vol. 1, paper number, pp. 1-11, 2001.

[3] Smith J., Jones A.B. and Brown J., The title of the paper. *Journal Name*, Vol. 1, No. 1, pp. 1-11, 2001.

[4] Smith J., Jones A.B. and Brown J., *Patent title*, U.S. Patent number, 2001.

International Journal of Mechanics and Control – JoMaC
Published by Levrotto&Bella

TRANSFER OF COPYRIGHT AGREEMENT

NOTE: Authors/copyright holders are asked to complete this form signing section A, B or C and mail it to the editor office with the manuscript or as soon afterwards as possible.	*Editor's office address:* Andrea Manuello Bertetto Elvio Bonisoli *Dept. of Mechanics* *Technical University-Politecnico di Torino* ***C.so Duca degli Abruzzi, 24. 10129 Torino – Italy*** e_mail: jomac@polito.it fax n.: +39.011.564.6999

The article title:

By:____

To be Published in ***International Journal of Mechanics and Control JoMaC***
Official legal Turin court registration Number 5320 (5 May 2000) - reg. Tribunale di Torino N. 5390 del 5 maggio 2000

A Copyright to the above article is hereby transferred to the JoMaC, effective upon acceptance for publication. However the following rights are reserved by the author(s)/copyright holder(s):
1. All proprietary rights other than copyright, such as patent rights;
2. The right to use, free or charge, all or part of this article in future works of their own, such as books and lectures;
3. The right to reproduce the article for their own purposes provided the copies are not offered for sale.

To be signed below by all authors or, if signed by only one author on behalf of all co-authors, the statement A2 below must be signed.

A1. All authors:

SIGNATURE____________________________DATE__________ SIGNATURE____________________________DATE__________

PRINTED NAME______________________________________ PRINTED NAME______________________________________

SIGNATURE____________________________DATE__________ SIGNATURE____________________________DATE__________

PRINTED NAME______________________________________ PRINTED NAME______________________________________

A2. One author on behalf of all co-authors:
"I represent and warrant that I am authorised to execute this transfer of copyright on behalf of all the authors of the article referred to above"

PRINTED NAME______________________________________

SIGNATURE____________________________ TITLE____________________________ DATE______________

B. The above article was written as part of duties as an employee or otherwise as a work made for hire. As an authorised representative of the employer or other proprietor. I hereby transfer copyright to the above article to Editel-Pozzo Gros Monti effective upon publication. However, the following rights are reserved:
1. All proprietary rights other than copyright, such as patent rights;
2. The right to use, free or charge, all or part of this article in future works of their own, such as books and lectures;
3. The right to reproduce the article for their own purposes provided the copies are not offered for sale.

PRINTED NAME______________________________________

SIGNATURE____________________________ TITLE____________________________ DATE______________

C. I certify that the above article has been written in the course of employment by the United States Government so that no copyright exists, or by the United Kingdom Government (Crown Copyright), thus there is no transfer of copyright.

PRINTED NAME______________________________________

SIGNATURE____________________________ TITLE____________________________ DATE______________

CONTENTS

next number scheduled titles:

Design Parameters Sensitivity Analysis of a New Diesel Locomotive
P. Belforte, F. Cheli, A. Collina, L. Prone, G. Tomasini

Nonlinear Elastic Characteristic of Magnetic Suspensions through Hilbert Transform
E. Bonisoli

Design of Advanced Robotic Systems for Assembly Automation
M. Callegari, A. Gabrielli, M. C. Palpacelli, M. Principi

Multi-body Dynamic Modeling of the Expected Performance of Accelerated Pavement Testing
E. Santagata, M. Velardocchia, E. Galvagno, D. Lioi, A. Sorniotti

Proposal of Innovative Fluido-dynamic Nonlinear Servovalve's Model
L. Borello, M. D. L. Dalla Vedova